# Optimising the Near-Infrared Survey Strategy in Unveiling Hidden Galaxies in the Great Attractor

James Tagg

Department of Astronomy
University of Cape Town
South Africa

Supervisors:
Prof. R.C. Kraan-Korteweg & Dr. P.A. Woudt



*A dissertation submitted in partial fulfillment of the requirements for the degree M.Sc. in the Department of Astronomy, as part of the National Astrophysics and Space Science Programme*
UNIVERSITY OF CAPE TOWN

November 5, 2008

# Abstract

An optimisation strategy for completing a near infrared survey of the Great Attractor, where it crosses the Zone of Avoidance, is presented in this thesis. The full survey is expected to cover an area of approximately 70 deg$^2$ centred on the Great Attractor, and is complete in the $K_s$-band to $K_s^{lim} = 14.^{\rm m}72$. Seven regions, covering in total $\sim 2.5$ deg$^2$ within the survey area, were chosen for analysis with respect to galaxy identification in different environments of diverse star crowding and dust extinction. A photometric catalogue of galaxies identified in these regions is presented. The catalogue consists of 115 objects, 106 of which are considered definite galaxies, and 9 which are considered candidate galaxies. Analysis of near infrared colours of the galaxies suggests an overestimate of the existing DIRBE/IRAS reddening maps (Schlegel et al., 1998) close to the Galactic Plane ($|b| \leq 5°$) of 25%. Three regions were found to have galaxy number densities consistent with the region surrounding PKS 1343-601, a suspected overdensity in the Great Attractor. Success of galaxy identification was quantified in terms of environment. This yielded star density and extinction contours of $3.2 \times 10^4$ stars/deg$^2$ and $A_{K_s} = 0.^{\rm m}5$ respectively, above which galaxy identification was far less efficient. These contours, along with the three regions of suspected overdensity suggest possible avenues for completion of the survey observations.

# Acknowledgements

First and foremost I would like to thank my supervisors, Professor Renée Kraan-Korteweg and Dr. Patrick Woudt. Their invaluable assistance with all aspects of this work including their patient reading and feedback with the many drafts of this paper, and the invaluable lessons learned are sincerely appreciated. I would also like to thank our Japanese collaborators, Professor Ken-ichi Wakamatsu and Dr. Taka Nagayama, for the use of their survey data, without which this work could not have been completed. Within the UCT Astronomy department, I would like to thank my colleague and friend Ewald Zietsman for the countless discussions on statistics and life, as well as Ed, Paul, and Michelle for their support and helpful suggestions. Then to my parents, thank you for listening and for supporting me continually throughout. Finally, I'd like to thank Carol for the never-ending patience and continual motivation that kept me going.

This work was funded and made possible by the National Astrophysics and Space Science Programme (NASSP).

*This thesis makes use of data products from the Two Micron All Sky Survey, which is a joint project of the University of Massachusetts and the Infrared Processing and Analysis Center/California Institute of Technology, funded by the National Aeronautics and Space Administration and the National Science Foundation.*

# Contents

# List of Tables

# List of Figures

# Chapter 1

# Introduction

In this thesis, the current state of observations and data reduction of a near infrared survey currently underway (henceforth 'the survey') are examined, and solutions for improving the basic survey strategy are explored. The survey was started in 2006, using the Infrared Survey Facility located at the South African Astronomical Observatory site in Sutherland, South Africa. The survey aims to uncover galaxies hidden by a thick obscuration layer of dust and stars in the plane of the Milky Way, as part of an ongoing attempt to discover the true nature and extent of the Great Attractor. The Great Attractor is an important mass overdensity in the nearby Universe, although it has yet to be fully uncovered and thoroughly studied.



## 1.1 The Great Attractor

To address the underlying question of why this survey was initiated, a review of the Great Attractor (GA) will be given. This discussion will cover a few relevant aspects of large scale structure. In particular the GA's identification, its scientific significance, and gaps in our full understanding of it are discussed.

Galaxies are generally distributed, in physical space, in large structures such as clusters, or along filamentary structures (e.g. Jarrett et al., 2006). The earliest indications for large scale structures were discovered through the life works of Sir William Herschel (1738-1822) and Sir John Herschel (1792-1871) who mapped the distribution of extragalactic 'nebulae'. The first recognition of structure on "very large" scales[1], however, was presented by Jôeveer & Einasto (1978), after redshift plots of data from the *Second Reference Catalogue* (De Vaucouleurs et al., 1976) revealed cellular structure in galaxy distribution. Where large scale structures

[1]Structure at a ~20 Mpc scale could be seen.

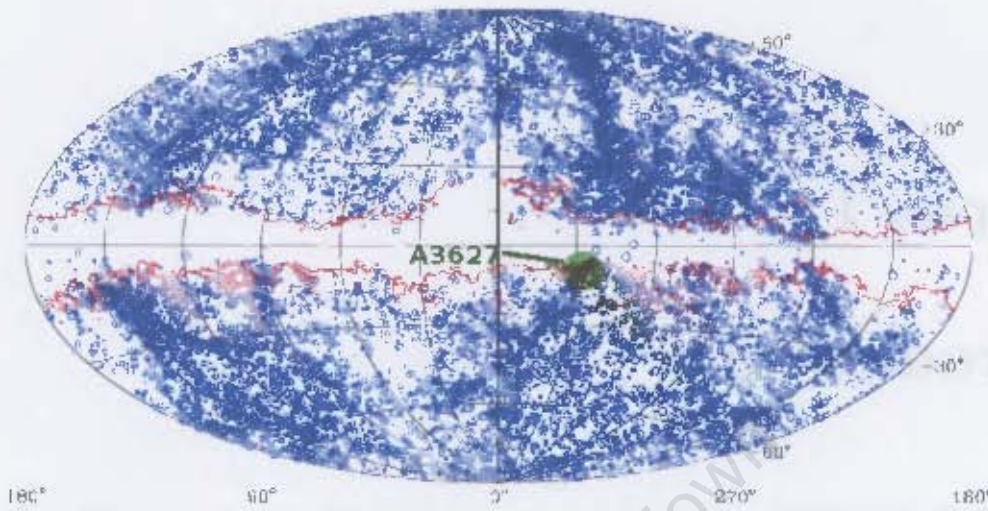


Figure 1.1: Equal-area Aitoff projection in Galactic coordinates of the distribution of extended sources in the optical. Generated by a compilation of galaxy catalogues, this plot is complete for sources with galaxy diameter $D > 1.3'$. Galaxies are diameter-coded, with larger circles depicting larger diameter. The central position is the Galactic centre; the Norma cluster (A3627) is highlighted. The solid contour marks the $A_B = 1.0$ mag absorption level in the $B$-band. It appears a good indicator of the extent of the Zone of Avoidance in the optical. (Image courtesy of Kraan-Korteweg, private communication).



intersect, we often see dense mass concentrations. One such concentration is the Coma cluster $(l, b, v) = (58.1^{\circ}, 88.0^{\circ}, 6925 \text{ km s}^{-1})$ (Abell, Corwin & Olowin, 1989).

A visual impression of the large scale structures is immediately obtained by looking at the projected distribution of galaxies in the sky. By combining homogenized data from various optical galaxy catalogues, a whole sky catalogue of galaxies was created (Kraan-Korteweg, 2000a). This catalogue is complete for galaxies with $D \geq 1.3'$ (Hudson & Lynden-Bell, 1991) where $D$ represents the galaxy diameter (see Fig. 1.1). It shows the projected whole sky distribution of local large scale structures with the exception of a horizontal band of width $\sim 20^{\circ}$ around the Galactic Plane (GP). This narrow band (also known as the Zone of Avoidance (ZOA) - see Sect. 1.2) is thought to conceal a large mass overdensity (the mass is not exactly known, but known contributing clusters infer a mass of the order $10^{16} M_{\odot}$) dubbed 'the Great Attractor'.

The presence of the GA was first inferred by Lynden-Bell et al. (1988) after noting that most nearby galaxies are streaming on a large scale toward a specific region of $(l, b, v) \approx (307^{\circ}, +9^{\circ}, 4350 \perp 350 \text{ km s}^{-1})$. It was postulated that a GA must be centred at that position,

since only a great mass overdensity (of order $10^{16}M_{\odot}$) could induce a gravitational flow on such large scales. However, since the GA is obscured by stars and interstellar dust in the Milky Way (MW), no density peak in the form of galaxies could be identified at the time (see Fig. 1.1).

One of the techniques used for calculating the GA overdensity is a reconstruction of the mass distribution based on an analysis of galaxy motions. Assuming galaxy motions are caused by the local gravity field, two methods for applying this technique, are the Wiener Filter method (Hoffman, 2000), and the POTENT method (Dekel, 1994). Both methods infer the presence of the GA in the southern MW. A later study narrowed down the location of the centre potential well of the GA to $(l, b, v) = (320°, 0°, 4500 \text{ km s}^{-1})$ (Kolatt et al., 1995).

More recently Tonry et al. (2000) found the GA centre to be even closer than previous estimates, at different Galactic longitude and latitude, and with a lower mass than previously found by Lynden-Bell et al. (1988). This result was based on the surface brightness fluctuation (SBF) method for measuring distances to early-type galaxies (see Tonry & Schneider, 1988).

Since its discovery, much work has been done to reveal the galaxies and clusters contributing to the GA. ACO3627 (Abell, Corwin & Olowin, 1989), now known as the Norma cluster, was identified by Kraan-Korteweg et al. (1996) as the very massive cluster in the GA region at $(l, b, v) = (324.3°, -7.2°, 4848 \text{ km s}^{-1})$. They suspected that it lies at the bottom of the potential well of the GA overdensity given its high mass ($0.9 \times 10^{15}M_{\odot}$ within its Abell radius (Woudt, Kraan-Korteweg & Fairall, 2000)), which is comparable to that of the Coma cluster, and its proximity to the initial Kolatt et al. (1995) GA location.

Besides the Norma cluster, a number of lower mass clusters have also been identified to form part of the GA. Cen-Crux $(l, b, v) \simeq (305°, +5°, 6214 \text{ km s}^{-1})$ is a relatively low-mass cluster constituting part of the GA (Woudt & Kraan-Korteweg, 2000, 2001), with a more massive neighbour, the X-ray cluster CIZA J1324.7-5736 ('Clusters in the Zone of Avoidance (CIZA)' Ebeling, Mullis & Tully, 2002) at $(l, b, v) \simeq (307°, +5°, 5700 \text{ km s}^{-1})$. In general, very strong radio continuum sources could lie at the centre of rich clusters, and Woudt & Kraan-Korteweg (2000) note that one such source, PKS 1343-601, lies in the GA region at $(l, b, v, A_B) = (309.7°, +1.9°, 3800 \text{ km s}^{-1}, 12^{\text{m}})$. Nagayama et al. (2004) report the presence of an intermediate mass cluster, or "density enhancement", centred on PKS 1343-601, based on deep near infrared (NIR) observations. No X-ray emission associated with this cluster has been found (Ebeling, Mullis & Tully, 2002). Tashiro et al. (1998) present X-ray evidence from the Advanced Satellite for Cosmology and Astrophysics (ASCA) to support the conclusion that PKS 1343-601 is not a rich cluster.

It was suggested by Kraan-Korteweg et al. (1994), that the GA is a "confluence of superclusters" and that the central density peak of the GA most likely is the Norma cluster. Figure 1.2 shows the major large-scale structures that have been identified thus far in the GA region. These

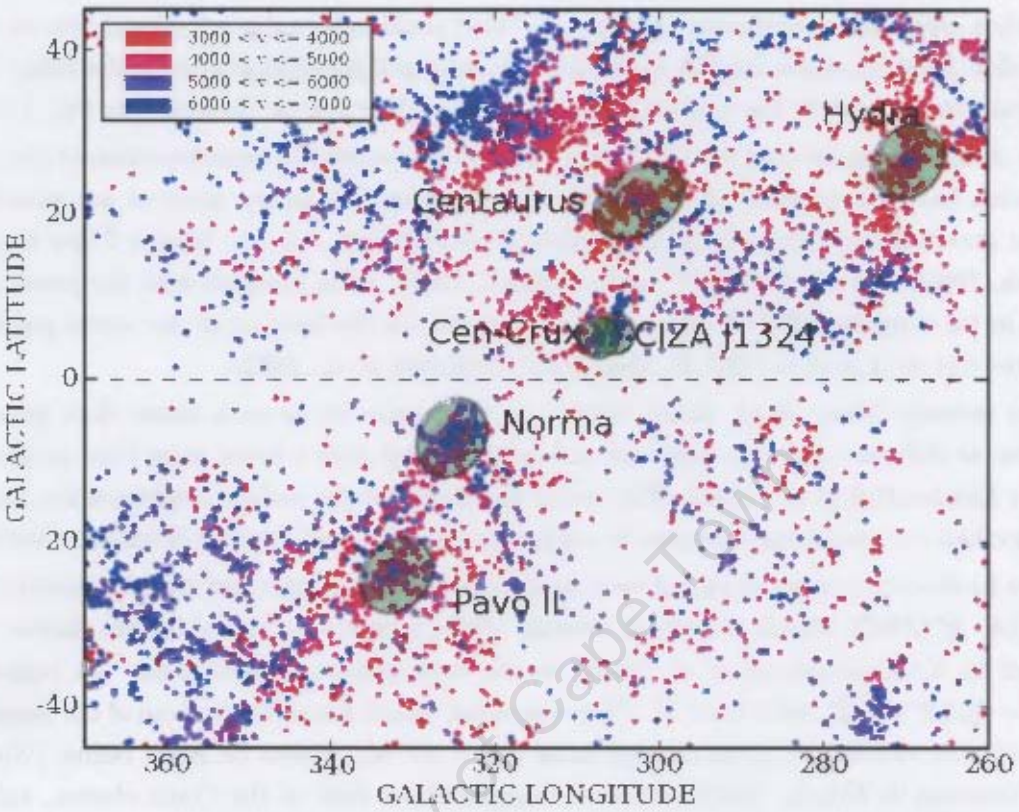


Figure 1.2: Large-scale structures in the Great Attractor region. Galaxies with distances between $3000 < v_{hel} < 7000$ km s$^{-1}$ are shown. Important clusters in the Norma Wall are highlighted.

include the Norma cluster, Centaurus cluster $(l, b, v) \simeq (302°, 22°, 3400$ km s$^{-1})$, Hydra cluster $(l, b, v) \simeq (270°, 27°, 3800$ km s$^{-1})$, Pavo II cluster $(l, b, v) \simeq (332°, -24°, 4200$ km s$^{-1})$, Cen-Crux cluster and CIZA J1324.7-5736. Woudt et al. (1997) proposed that a 'Great Wall' structure extends from the Pavo II cluster, through the Norma cluster, then bending across the GP to the Cen-Crux cluster and then further to $l \sim 290°$. This Great Wall (or Norma supercluster) "constitutes the major structure in the GA region" (Radburn-Smith et al., 2006). Further evidence for the presence of the Norma supercluster extension at $(l, v) = (300° - 340°, 5000$ km s$^{-1})$ was found through blind HI surveys in the southern sky (Henning et al., 2005).

The GA has significant bearing on the dynamics of the MW and the Local Group of galaxies (LG). Kocevski & Ebeling (2006) amongst others, propose that 44% of the LG's peculiar velocity is due to infall into the GA, while the remaining 56% is due to more distant structures between $130h^{-1} - 180h^{-1}$ Mpc. However, this is still controversial; it remains debated whether the GA is chiefly responsible for the LG's motion or more distant large-scale structures that govern the

peculiar motion of the LG. Knowing the peculiar velocities of galaxies in and around the GA may help to resolve the debate. Peculiar motions of galaxies in the GA can give an indication as to whether the GA itself is involved in an even larger scale flow or at rest with respect to the Cosmic Microwave Background (CMB) (Woudt & Kraan-Korteweg, 2000). The peculiar motions of galaxies in the GA are hardly known because of its central location behind the MW. Lucey et al. (2004) amongst others propose that the GA is itself involved in a larger flow toward the Shapley Concentration at $(l, b, v) = (306.4°, 29.7°, 12891 \text{ km s}^{-1})$ .

More recently, reconstruction of real-space density distributions from redshifts in the Two Micron All Sky Survey (2MASS) Redshift Survey (2MRS) have helped reconcile observed and reconstructed distributions (Erdoğdu et al., 2006), although these do exclude the ZOA around the GA. Further observational work must still be done to get a more precise view of the galaxy distribution in the GA. This is a central point to the survey which this project addresses.

There remains large scope for future work on the GA. Of the work to be done, a critical part is obtaining more multi-wavelength observational data on galaxies in the GA, in particular at low latitudes and obscured regions of the ZOA. This will help to reconcile the different opinions on the GA's mass, position and motion, and to improve current estimates of the GA's contribution to the LG's peculiar velocity. In particular, the possibility of further clusters lying near the bottom of the GA potential well, where $A_B \gtrsim 3^{\text{m}}$, is not implausible (Kraan-Korteweg, 2005).

The controversy surrounding the GA, the lack of data for galaxies in the GA, and the inherent difficulty in working with ZOA data motivated this NIR survey to be initiated. The very great dust extinction in the ZOA is less of a problem for NIR observations. Existing NIR archive data is at a resolution significantly lower than that capable by the Infrared Survey Facility (IRSF) (see Sect. 1.3). This survey is important because it addresses these problems by providing unique NIR data on galaxies as yet undiscovered, and NIR data for correlation with existing data of known galaxies in the GA. Of course, the greatest constraint to the survey, and on future GA observations, remains the most opaque and star-crowded regions of the ZOA.



## 1.2 The Source of Confusion - the ZOA

As previously mentioned, the reason for the lack of observational evidence to support the reconstructed galaxy distribution inferring the GA, is the Zone of Avoidance - a region of high dust extinction and interstellar confusion. At optical wavelengths, approximately one fifth of the sky is obscured by dust in the MW. This obscuration explains the historical origin of the ZOA. Early astronomers noted a lack of extragalactic sources in this region of the sky and named it accordingly, first describing it as the "Zone of few Nebulae" (Proctor, 1878). Astronomers tended to avoid making observations in the ZOA because of the difficulty of observing extragalactic

objects through the dust and stars (Woudt, 1998; Kraan-Korteweg & Lahav, 2000). It was in 1961 that a more scientific definition of the ZOA was made by Shapley (1961) as the region defined by "the isopleth of five galaxies per square degree from the Lick and Harvard surveys". This defined contour of low number density contrasts strongly with the typical density of galaxies in the unobscured sky of 54 gal./sq.deg. by Shane & Wirtanen (1967).

The optical ZOA refers to a band of width $\sim 20°$ centred on the GP. It is a result of the interstellar dust in the disk of the MW which scatters and absorbs extragalactic light trying to pass through it. These grains absorb and scatter light from extragalactic sources along the line of sight to us (an effect known as extinction). Light at the blue end of the spectrum is more scattered than red. Extinction diminishes short wavelength light more than long wavelength light. Optical light trying to pass through the ZOA is reduced as a function of wavelength, resulting in optical detectors detecting less emission from extragalactic sources obscured by the ZOA, than NIR detectors. It is in fact wavelength-dependent extinction which determines the actual size and shape of the ZOA (Kraan-Korteweg, 2005).

As the foreground extinction increases (close to the GP), detections of spiral galaxies in optical searches drop dramatically. This is because the isophotal diameter and brightness of a galaxy decreases as a function of extinction. The isophotal dimming effect was modelled in simulations done by Cameron (1990) for optical wavelengths. In this case, the low surface brightness disk component of spiral galaxies which is blue as well, will be lost first, leaving just the nucleus, which often results in the galaxy not being detected. Elliptical galaxies are also affected, but less so. This is because they are redder and have a different surface brightness profile to spirals.

Much survey work has been done to penetrate the ZOA. In the scope of this project, it is important to see what work has been done in terms of reducing the ZOA through discovery of galaxies at low latitudes, and at what wavelengths the best results have been obtained. Despite the limitations due to dust extinction close to the GP, a large number of ZOA surveys have been performed in the optical. Deep optical searches have reduced the optical ZOA by a factor of $\sim 3$ to a region within the extinction contour of three magnitudes in the blue band ($A_B = 3^{\mathrm{m}}$) (Kraan-Korteweg & Lahav, 2000), compared to $A_B = 1^{\mathrm{m}}$ (see Fig. 1.1).

Far infrared (FIR) observations, by the Infrared Astronomical Satellite (IRAS), are not affected by the midplane extinction. These have helped in mapping the distribution of galaxies throughout 96% of the sky at 12, 25, 60 and 100$\mu$m (Joint *IRAS* Science Working Group, 1988). FIR observations are sensitive only to the emission from spiral and star-burst galaxies, and not elliptical galaxies, which are typically the dominant mass component of clusters. Furthermore, extragalactic FIR sources in the MW are not easily distinguished from Galactic sources. Follow up work by Saunders et al. (2000) helped confirm the extragalactic nature of the sources in the

IRAS Point Source Catalogue in the ZOA.

In the radio wavelength regime, the Parkes 64m telescope was used to conduct a Multibeam (MB) survey to uncover galaxies at the lowest Galactic latitudes ($|b| \lesssim 5°$) in the southern ZOA (Henning et al., 2000). About $\sim 1000$ new extragalactic sources were found in this way, with radial distance measurements determined from the redshift in the neutral hydrogen (HI) emission line.

The future of ZOA work will be most likely to advance through observations in certain wavelengths only. While optical searches have certainly narrowed the ZOA significantly, the remaining work should be done in wavelength regimes less affected by extinction, such as NIR, radio, and X-ray. Radio waves are impervious to the effect of extinction in the ZOA, and can provide useful distance data to highly obscured galaxies. X-rays observations are useful for identifying clusters, because the intercluster medium gets hot enough to produce X-rays. Although this is good for mapping large scale structures, individual galaxies are not detected and cannot be studied. X-ray surveys such as CIZA are useful for determining where we are likely to find galaxies, but are limited to space telescopes. X-ray searches are also sensitive only to clusters which are dominated by ellipticals. In particular, NIR observations can be invaluable for work on galaxies that are highly obscured by dust extinction.



## 1.3 Near-Infrared Motivation and Limitations

Different wavelengths have partly complimentary characteristics for uncovering galaxies at low latitude. Young stars burning at a higher temperature radiate blue wavelength light where they are well detected by optical detectors. This effect is due to Wien's displacement law which states that the temperature of a blackbody is inversely proportional to the wavelength at which peak emission occurs.

$$\lambda_{max} \propto \frac{1}{T} \tag{1.1}$$

where $\lambda_{max}$ is the wavelength of peak emission and $T$ the temperature. Older stars have redder peak emission, and are hence detected by infrared detectors. Galaxies with large quantities of neutral hydrogen gas can be detected at radio wavelengths because the hyperfine splitting of neutral hydrogen HI in its ground state emits at 21cm. This is very useful for detecting galaxies at low Galactic latitudes, because radio waves are not scattered or absorbed by dust. However, for gas deficient galaxies (ellipticals, early type spirals), the NIR can provide a useful insight. These early type galaxies are typical of clusters and superclusters (Einasto et al., 2007), and these galaxian types are not detected in the ZOA in FIR or HI surveys (Schröder et al., 2000). In such galaxies, the dominant old stellar population accounts for the bulk of the galaxy's light. The result is that gas-deficient galaxies obscured by foreground extinction are best detected by

NIR telescopes. In addition, extinction in the ZOA will result in more NIR light reaching us than optical. *We thus expect near-infrared observations to be crucial for revealing galaxies in the ZOA.*

It is not only the dust that causes obscuration in the ZOA, but also the very high number density of stars (star crowding) which lead to obscuration of galaxies behind the GP. Star crowding creates some limitation for doing NIR work in the ZOA, and in particular close to the Galactic Bulge (GB). For a spiral galaxy, the blue light component in the disk is almost entirely absorbed, leaving mostly only the bulge of the galaxy detectable. This is still distinct though because the bulge of a spiral galaxy has a different profile to the point spread function of a star. However when trying to detect such objects in environments of extreme star crowding, it becomes virtually impossible. Kraan-Korteweg & Jarrett (2005) show that, for galaxies in the 2MASS Extended Source Catalogue (XSC), star crowding affects galaxy detection in the NIR ZOA more than extinction in high star density regions around the GB.

The NIR is still somewhat susceptible to the effect of extinction. Cardelli et al. (1989) provides an "extinction law" for calculating extinction at a given wavelength with respect to the extinction at a reference wavelength (shown in Equation 1.2).

$$\frac{A_\lambda}{A_V} = a(x) + \frac{b(x)}{R_V} \tag{1.2}$$

where $A_\lambda$ is the extinction at the wavelength $\lambda$ we are interested in, $A_V$ is the extinction in the visual, $x$ is the inverse of wavelength, i.e. $x = \frac{1}{\lambda}$, and $R_V \equiv \frac{A_V}{E(B-V)} = 3.1$ is a standard value for the interstellar medium. For NIR bands $J$, $H$, and $K_s$, the extinction law predicts that the respective extinctions are 21%, 14%, and 9% of the extinction in the $B$-band (Cardelli et al., 1989). The number of galaxies detected at low Galactic latitudes (more specifically, in the GA) decreases due to increasing foreground extinction, and the decrease is far slower in the NIR than in the optical (see Fig. 1 in Schröder et al. (2007), for example). Hence we detect more galaxies in NIR searches at low latitudes than in optical searches.

Nagayama (2004) simulated the effect of dust extinction in the NIR to show that smaller and fainter galaxies become undetectable when obscured by dust, and larger or brighter galaxies appear dimmed and smaller. As a result, many intrinsically large galaxies appear small and faint when obscured by interstellar dust in the ZOA and many galaxies are completely obscured, and may be omitted from magnitude- or diameter-limited catalogues (Kraan-Korteweg & Lahav, 2000). Although the effect of isophotal dimming and diameter reduction has not yet been modelled in NIR, Nagayama's simulation points toward an effect similar to the optical case of Cameron (1990).

Another important advantage of the NIR is being able to measure most of the stellar mass content of galaxies. Stellar mass content can be estimated because the bulk of the mass caused

by older stars contributes a significant flux in NIR. Recent star-formation regions in galaxies contribute only a small flux in the NIR.

Although we have looked at the physical advantages and disadvantages of NIR work, we must also consider the availability of NIR archive data. Large NIR surveys such as the Two Micron All Sky Survey (2MASS) (Jarrett et al., 2000; Skrutskie et al., 2006) and the DEep Near Infrared Survey (DENIS) of the southern sky (Epchtein, 1997) have been completed in the last decade, and provide a wealth of data on extragalactic sources across the whole sky. The 2MASS all sky release was made public in 2003 and provides catalogues of point sources and extended sources with photometry in the $J(\lambda_{central} = 1.25\mu\text{m})$, $H(\lambda_{central} = 1.65\mu\text{m})$ and $K_s(\lambda_{central} = 2.17\mu\text{m})$ bands. The extended source completeness limits ($10\sigma$) for the 2MASS survey are $J = 14.^{\text{m}}7$, $H = 13.^{\text{m}}9$, and $K_s = 13.^{\text{m}}1$. The resolution is $2''$ per pixel (Jarrett et al., 2000). This is particularly useful for comparison with our survey data (which uses the same wavelength bands) in terms of detection limits and photometry. DENIS also has a large volume of data for the $I$, $J$ and $K_s$ bands, with a detection limit for extended sources of $12^{th}$ magnitude for $K_s$ (Mamon, 1998).

Both DENIS and 2MASS have impressive sky coverage, but this has come at an expense in resolution and short integration time. Our survey data is capable of resolving smaller sources because of improved resolution. The IRSF imaging instrument has a resolution of $0.45''$ per pixel and the integration time for our ZOA survey was optimised at 600 seconds (refer to Sect. 2.1.2 for a discussion of depth versus star-crowding with respect to integration time). This results in magnitude limits several magnitudes fainter than the 2MASS XSC. This improved resolution and ability to detect fainter objects means we can probe further with this survey into the GA than was previously possible with existing survey data.



## 1.4 Project Aim and Outline

This project has the aim to design an optimal survey for completing a near infrared (NIR) survey of the Great Attractor (GA) across the Zone of Avoidance (ZOA). The relevance of such a survey has been highlighted through the description of the Great Attractor and its relevance to local large-scale structures, as well as the severe deficiency of GA data despite dedicated efforts in various other wavebands to unveil the GA across the ZOA. The strategy optimisation will be achieved through a thorough analysis of a subset of the survey data at various extinction and star-crowding levels.

Chapter 2 gives details of the survey area and the survey observations, as well as a comparison of the IRSF and 2MASS data properties. General survey strategy arguments are discussed. The details of the data reduction process, from the initial choice of data to reduce and analyse, to

the actual reduction process are then presented. The data reduction consists of frame processing (stacking, cleaning), astrometric calibration, star removal, and photometry.

Chapter 3 presents the results of the photometry in the form of a catalogue of all galaxy candidates, and an analysis of the data. Photometric properties of galaxies in different environments of extinction and star crowding are examined, and the results are compared with 2MASS Extended Source Catalogue (XSC) data.

Chapter 4 discusses the resulting galaxy identification efficiency, and how to use this knowledge to propose an optimised observation strategy.

# Chapter 2

# A NIR Survey of the GA Region

In March 2006, a near infrared (NIR) survey ($J(\lambda_{central} = 1.25\mu\text{m})$, $H(\lambda_{central} = 1.65\mu\text{m})$ and $K_s(\lambda_{central} = 2.17\mu\text{m}$ bands)) of the central Great Attractor (GA) region was initiated using the InfraRed Survey Facility (IRSF) in Sutherland. This survey aims to recover the distribution of galaxies in the Norma wall (Woudt, 1998; Radburn-Smith et al., 2006) at very low Galactic latitude; the Norma wall crosses the Galactic plane diagonally from the Vela cluster $(l, b, v) = (280°, +6°, 6000$ km s$^{-1})$, via the Centaurus-Crux cluster $(l, b, v) = (305.5°, +5.5°, 6214$ km s$^{-1})$ (Fairall et al., 1998) to the Norma cluster $(l, b, v) = (325.3°, -7.2°, 4844$ km s$^{-1})$ (Kraan-Korteweg et al., 1996; Woudt et al., 2008).

Fig. 2.1 shows the proposed survey area in Galactic coordinates, overlaid on the galaxy distribution in the GA region.



## 2.1 Observations

### 2.1.1 2006 and 2007 Observations

The footprint on the sky of the proposed survey (see Fig. 2.1) covers approximately 71.4 deg$^2$. With the field of view of the IRSF of $7.8' \times 7.8'$, this survey will take a substantial amount of observing time. In 2006, 12 weeks were allocated to the GA survey as part of a joint Japanese-South African collaboration, and 10 weeks were allocated for 2007. A further 8 weeks have been allocated in 2008 to complete the survey.

During the first year of observations (2006), 891 fields were observed. The first observed fields of 2006 were located in two branches - using my own nomenclature, the 'Upper Northern Branch' (UNB) which runs from approximately $304° < l < 311°$ and roughly $b \simeq 5°$, and the 'Southern Branch' (SB) approximately running from $306° < l < 325°$ and $-5° < b < 0°$.

Subsequently a new branch was defined later in 2006 - the 'Lower Northern Branch' (LNB) running from $305° < l < 309°$ and $3° < b < 4°$. These were observed in strips of equal Right Ascension (RA) spanning usually 11 fields per strip (or $7.8' \times 77.8'$) in the SB, and 10 fields per strip ($7.8' \times 70.8'$) in the UNB and LNB, with an overlap of $\sim 0.8'$ in declination between adjacent fields in a strip. The fields are labelled by their RA plus an integer that runs between $+9$ and $-9$, where this number refers to steps in declination of 7 arcminutes. In the northern branches, the declination number runs from $+0$ down to $-9$ and in the SB from $+5$ down to $-5$.

In 2007, new blocks of strips to be observed were added to the survey footprint, one on the SB ($322° < l < 325°$, $-5° < b < -3°$) and one on the LNB ($308° < l < 311°$, $2° < b < 4°$). The new blocks for 2007 (LNB block and SB block) consist of strips of 19 fields running from $+9$ down to $-9$. These can be seen in Fig. 2.1.

### 2.1.2 Details of the Observations

The survey is being carried out using the IRSF telescope at the South African Astronomical Observatory (SAAO) observing site in Sutherland, South Africa. The IRSF is a 1.4m alt-azimuth Cassegrain telescope and the imaging instrument is the Simultaneous 3-colour InfraRed Imager for Unbiased Surveys (SIRIUS). The three colours are the NIR passbands $J$, $H$ and $K_s$. SIRIUS has an array of three $1024 \times 1024$ pixel HgCdTe detectors (HAWAII array) (Kandori et al., 2006). This makes it an efficient instrument, being able to simultaneously gather high resolution data in three wavelength bands.

Each field was produced by combining twenty five dithered 24-second exposures, resulting in an effective exposure time of 600 seconds for each field (in each wavelength band) with a dither step of 15 arcseconds between each exposure. The exposure time is limited by two factors. The sky background at NIR wavelengths becomes too bright if individual frames are exposed too long. This results in an effective maximum exposure time of $\sim 24$ seconds in winter, and $\sim 15$ seconds in summer. At low Galactic latitudes, if the overall integrated exposure time is much longer than 600 seconds, the images become too heavily crowded with stars, effectively limiting our ability to identify extragalactic sources. The imaging instrument has a field of view of $7.8' \times 7.8'$ with a pixel scale of 0.45 arcseconds per pixel.

The main advantage of the IRSF/SIRIUS over existing all-sky surveys such as the 2MASS and DENIS surveys is the increased angular resolution. The 2MASS scans have a pixel scale of 2 arcsec/pixel (Skrutskie et al., 2006), the DENIS survey has 3 arcsec/pixel for the $J$ and $K_s$ bands, as opposed to the 0.45 arcsec/pixel of SIRIUS. This means that the resolution of our data is a factor $\sim 4.5$ higher than that of 2MASS data. In addition, being able to choose the exposure time is important in determining the quality and depth of the data. The IRSF survey

offers a substantial increase in depth. This is because longer exposures give a deeper view, at the expense of greater star crowding. Conversely, short exposures yield less star crowding but fail to detect fainter galaxies. The extended source completeness limits for the IRSF are $J = 16.^{\rm m}3$, $H = 14.^{\rm m}9$ and $K_s = 14.^{\rm m}7$ (see Sect. 3.1.2). In contrast, the 2MASS extended source completeness limits are $J = 14.^{\rm m}7$, $H = 13.^{\rm m}9$ and $K_s = 13.^{\rm m}1$ (Jarrett et al., 2000) and the DENIS extended source completeness limits at high Galactic latitudes are $J = 16.^{\rm m}5$, $H = 14.^{\rm m}8$ and $K_s = 12.^{\rm m}0$ (Mamon, 1998).

Table 2.1 compares the basic properties of the 2MASS, DENIS and IRSF telescope and image features for this survey.

Table 2.1: Comparison of IRSF, 2MASS and DENIS survey properties

| Telescope | Field of View [arcmin] | Wavelength [$\mu$m] | Spatial Resolution [$''$/pixel] | Integration time [sec] |
|---|---|---|---|---|
| (1) | (2) | (3) | (4) | (5) |
| IRSF | $7.8 \times 7.8$ | $J, H, K_s$ (1.25, 1.65, 2.17) | 0.45 | 600 |
| 2MASS | $8.5 \times 8.5$ | $J, H, K_s$ (1.25, 1.65, 2.17) | 2.0 | 7.8 |
| DENIS | $12 \times 12$ | $I, J, K_s$ (0.82, 1.65, 2.17) | $1.0 - 3.0$ | $\sim 9$ |



### 2.1.3 Initial Plan for Survey Optimisation

The survey is expected to map the distribution of extragalactic extended sources across an area of approximately 71.4 deg$^2$ ($\sim$ 4000 fields of $7.8' \times 7.8'$ - see Fig. 2.1). The exposure time, readout time, and vast number of fields give rise to a long timescale to complete the survey (longer than the time allocated from 2006 - 2008). Since the exposure time and readout time are fixed (assuming we have chosen a practical exposure time - see Sect. 2.1.2), a strategy for reducing the number of fields to be observed is required. The goal of this study is to find ways to optimise this survey, and so it is important to carefully select regions for analysis within the survey area that trace different environments of star density and dust extinction. By analysing chosen representative fields with respect to the likelihood of galaxy identification in different environments, a skeleton trace of the Norma Wall will be revealed. After this analysis, it will be clear which environments yield the highest level of extragalactic source extraction.

Accordingly, follow-up observations may be done in the regions which are expected to show the most galaxies. Follow-up observations can be done in different wavelength bands besides the NIR observations such as in the Mid-Infrared (MIR) regime or at radio wavelengths (HI). The practical advantage of doing this is that HI observations for example are impervious to foreground Galactic dust extinction, making galaxy detections close to the GP easier. HI

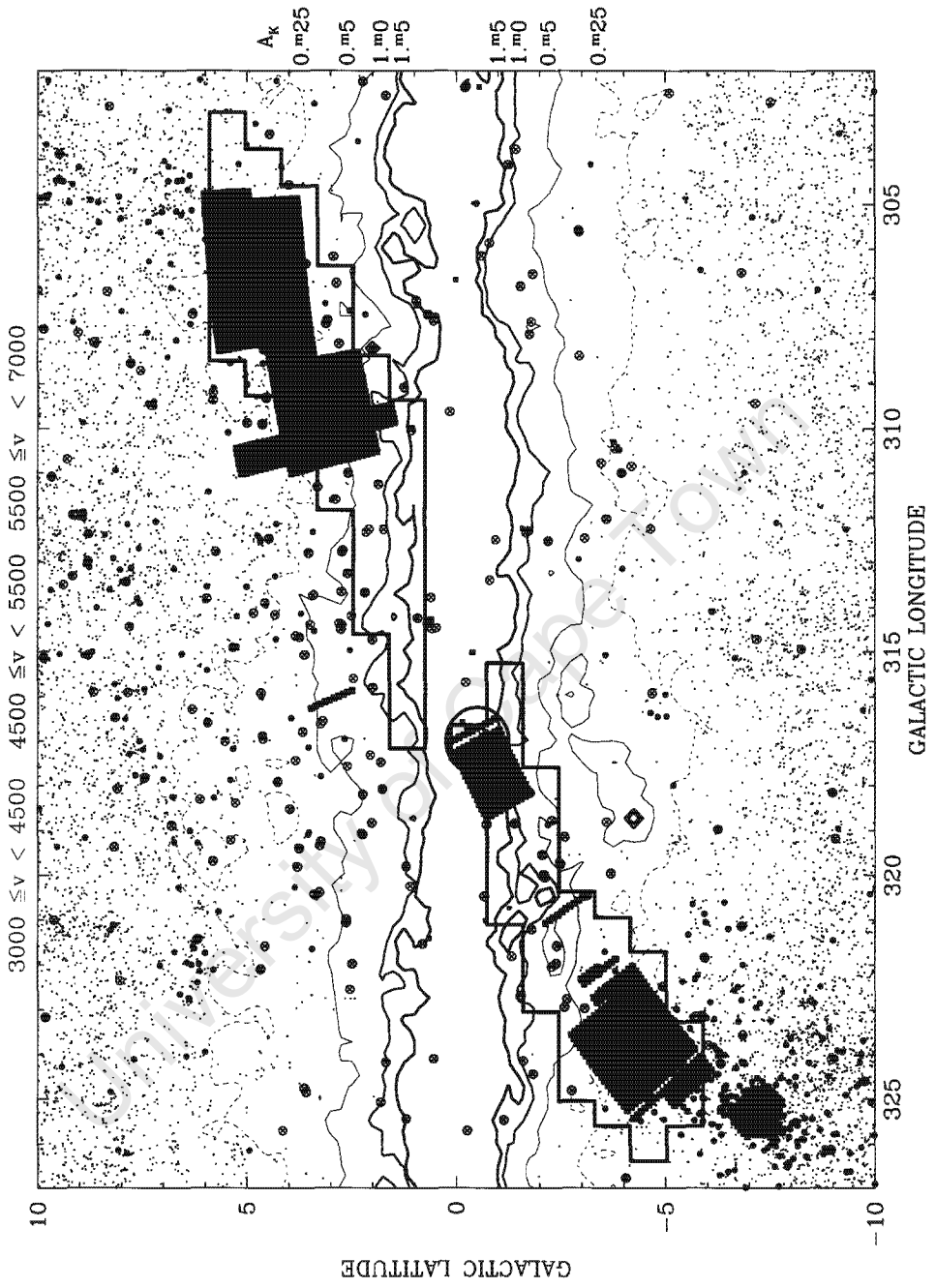




Figure 2.1: Survey Area - The solid black borders indicate the originally proposed survey area. The yellow blocks indicated survey area still to be observed, the black blocks indicate survey area already observed, and the green lines are contours of extinction in the $K_s$ band. The different coloured circles indicate galaxies out to different redshifts. Green dots indicate galaxies already known from optical searches; red dots indicate 2MASS galaxies. (Image courtesy of Kraan-Korteweg (private communication)).

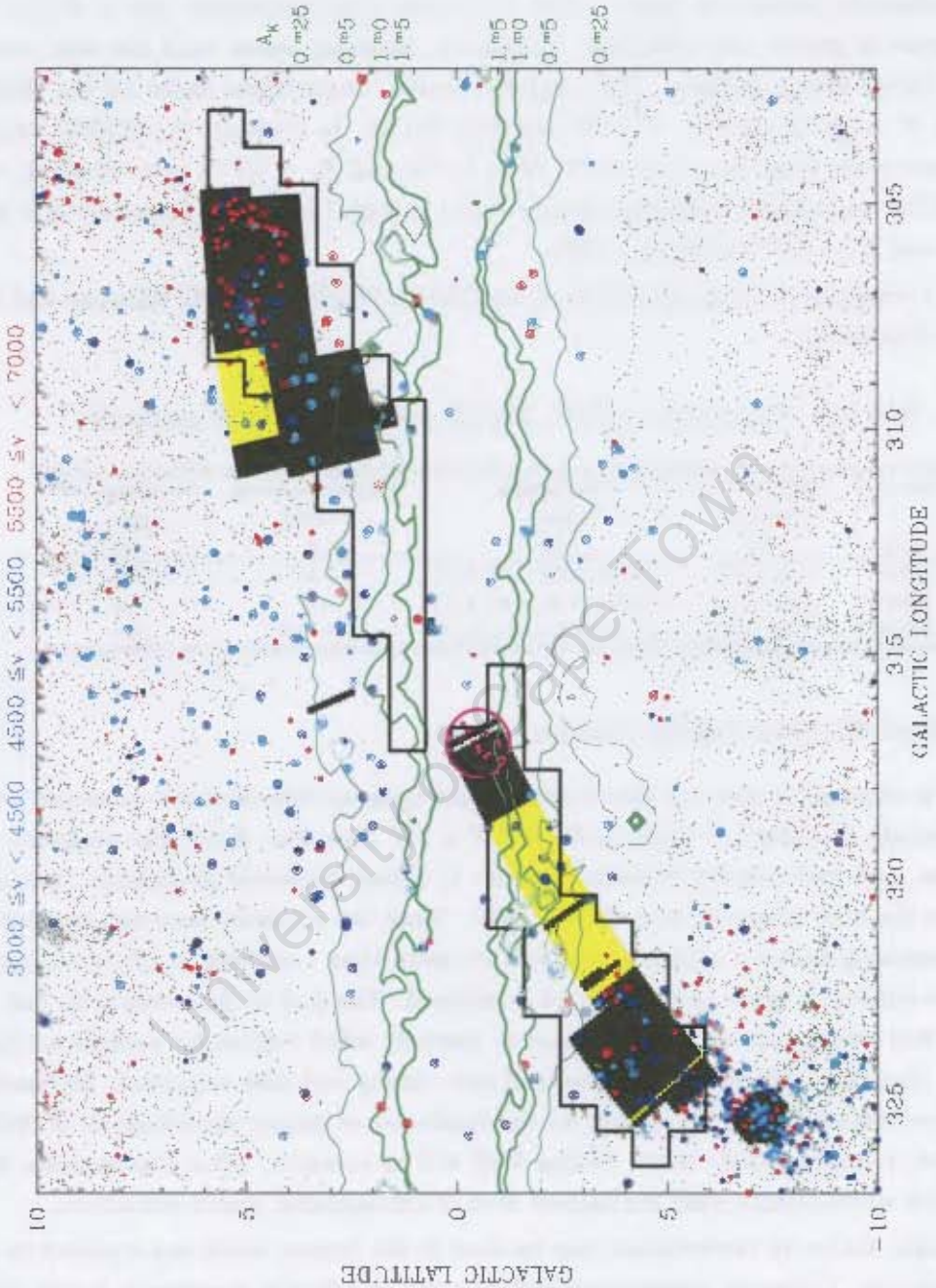




Figure 2.1: Survey Area - The solid black borders indicate the originally proposed survey area. The yellow blocks indicated survey area still to be observed, the black blocks indicate survey area already observed, and the green lines are contours of extinction in the $K_s$ band. The different coloured circles indicate galaxies out to different redshifts. Green dots indicate galaxies already known from optical searches; red dots indicate 2MASS galaxies. (Image courtesy of Kraan-Korteweg (private communication)).

observations may also be useful for measuring redshifts for galaxies in the GA. Further improvement of the strategy may be possible by doing follow-up observations that are more spread out. Instead of doing observations in consecutive strips (see Sect. 2.1.2 for details of the data strips), it may be possible to instead observe every second strip, thereby reducing observation time by a further half. Although only half the amount of possible galaxies would be detected (assuming a statistically homogeneous galaxy distribution), the trace would still clearly emerge. This is a more elegant approach to mapping the wall structure than a 'brute-force' approach since it will reduce the number of unnecessary observations.

## 2.2 Field Selection

The survey area covers approximately $325° \gtrsim l \gtrsim 305°$ and $-5° \gtrsim b \gtrsim 5°$ (Fig. 2.1). This work plans to optimise the survey observation strategy, and since observations cover such a broad range of fields in both position and environment, it is important to select fields from regions of diverse dust extinction and star-crowding (wide range of environments) for analysis. In order to find out how the environment changes across the survey area, a detailed knowledge of the dust distribution and star density distribution in the survey region is required.

Extinction due to interstellar dust was calculated from the $100\mu$m full sky dust temperature maps measured by the Diffuse InfraRed Background Explorer (DIRBE), combined with the earlier Infrared Astronomical Satellite (IRAS) measurements. The data from DIRBE, combined with numerical factors provided by Cardelli et al. (1989), provides values for the absorption and reddening factors at different wavelengths across the whole sky (see Sect. 1.3 for details). Although the DIRBE/IRAS maps are not calibrated at low latitudes ($|b| < 5°$) (Schlegel et al., 1998), we can still see a pattern emerge in Fig. 2.2 that shows that extinction due to interstellar dust increases greatly near the GP.

Star density was calculated by retrieving the 2MASS Point Source Catalogue (PSC) for sources with $K_s < 14^{\mathrm{m}}$ since this is the completeness limit of the PSC. The retrieved catalogue was then searched for sources lying within the fields of interest and these sources were counted. The result was the amount of stars in each field, which when divided by the area of the field and normalised to square degrees gives a star density in number per square degree for each field. The results are presented in Sect. 3.1.6.

It is necessary now to select fields for analysis based on different environments. Clearly, fields close to the GP are essential due to the extreme effects of dust extinction and star crowding. Conversely regions further away from the GP are equally important for their opposite effect of less dust extinction and less star crowding. A portion of the Norma Cluster lies within the survey area far south of the GP in latitude, and closer in longitude to the Galactic Bulge (GB) than

the rest of the survey area. An area closer in longitude to the GB is more crowded with stars than an area of equal dimension further from the GB (this is shown by Fig. 2.3 and Table 3.2), and so this is an important region to analyse due to higher star density but low dust extinction. It is also important to analyse survey fields north of the GP and at lower Galactic longitude, because they lie further from the bulge, but close enough to the GP to have an important mix of extinction and star crowding.

The strips that were analysed are accordingly spread fairly evenly across the survey area. They are divided into regions ordered according to RA. The breakdown of regions is explained in Sect. 3.1.7. The extinction, star number density and galaxy number density per strip are also explained further in Sect. 3.1.7.

## 2.3 Image Processing

The images that are captured as raw data from the telescope, are not suitable for immediate analysis because of imperfections in the telescope/detector optics, and because the counts are not calibrated and the frames not stacked. As such, images require processing (flat-field subtraction, dark current subtraction, sky subtraction). The first step is to create a good flat-field that can be used for pre-processing the images. It was decided that it would only be necessary to create one flat-field per month, i.e. have one flat-field (in each band) for data taken in April 2006 and so on, since variations in the physical integrity of the detector are not normally apparent on time scales much less than a month.

A flat-field is a frame showing the response of the optics to a uniform source. It is usually marked by blemishes on the detector array, which must be removed from science images so that they are not confused with astronomical sources. The flat-fields were created using the Image Reduction and Analysis Facility[1] (IRAF) task *autotwflat* from the SIRIUS package. This task chooses pairs of frames (with high enough background levels and adequate level difference) within a set of flat-fields taken on a particular evening (or morning). The two frames are then differentially combined, with the differential image then being normalised by the median value. The process is repeated for all the pairs of frames within all the specified sets of flat-fields, and the resulting normalised differential images are then median-combined (combining each image pixel-by-pixel with pixel values calculated from the median value) to create one final flat-field.



[1]IRAF is distributed by the National Optical Astronomy Observatory, which is operated by the Association of Universities for Research in Astronomy, Inc., under cooperative agreement with the National Science Foundation.

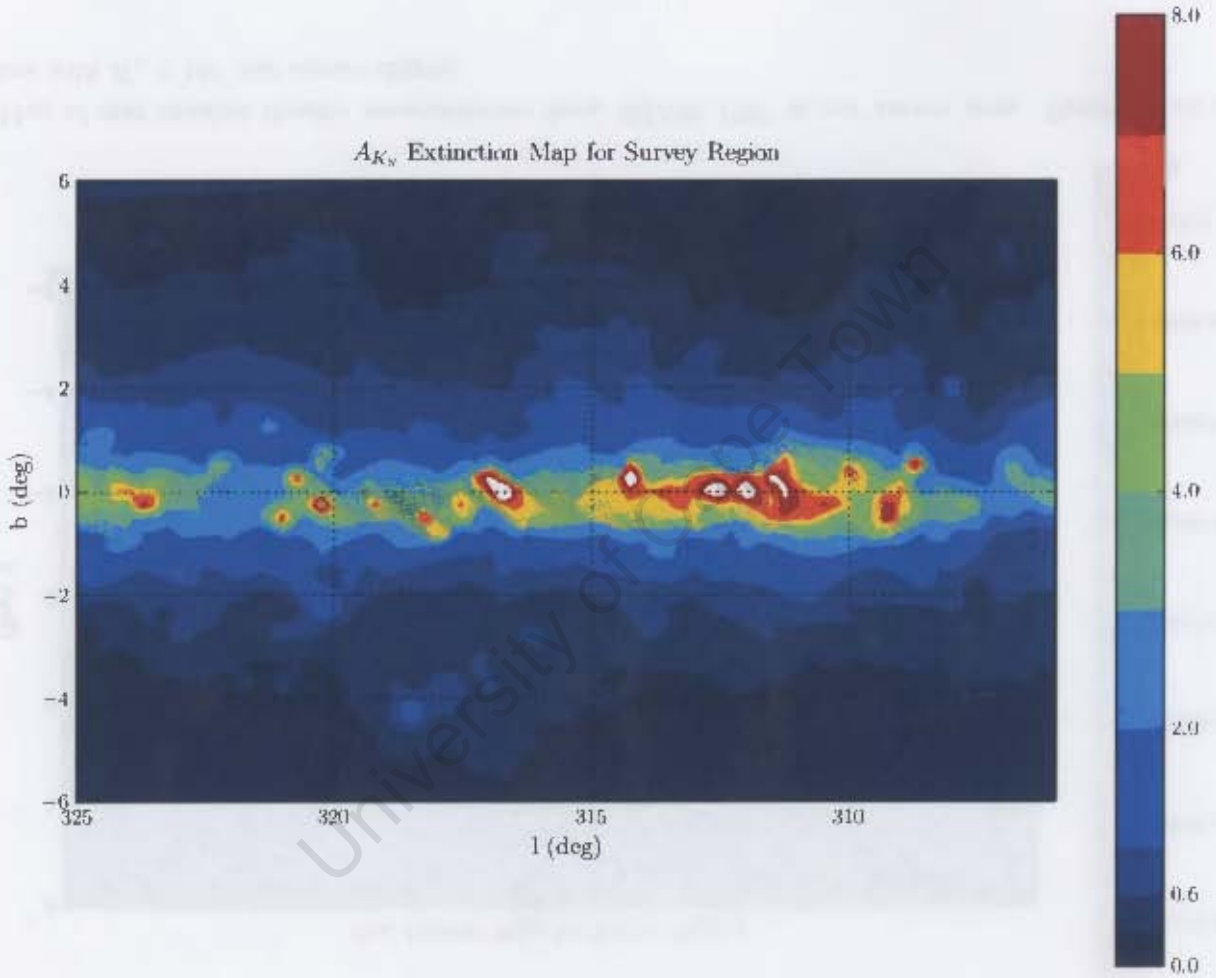




Figure 2.2: Map of selective $K_s$-band extinction $A_{K_s}$ values. Calculated by applying Cardelli et al. (1989) factors to colour excess $E(B-V)$ measurements from DIRBE/IRAS experiments (Schlegel et al., 1998) in our survey area.

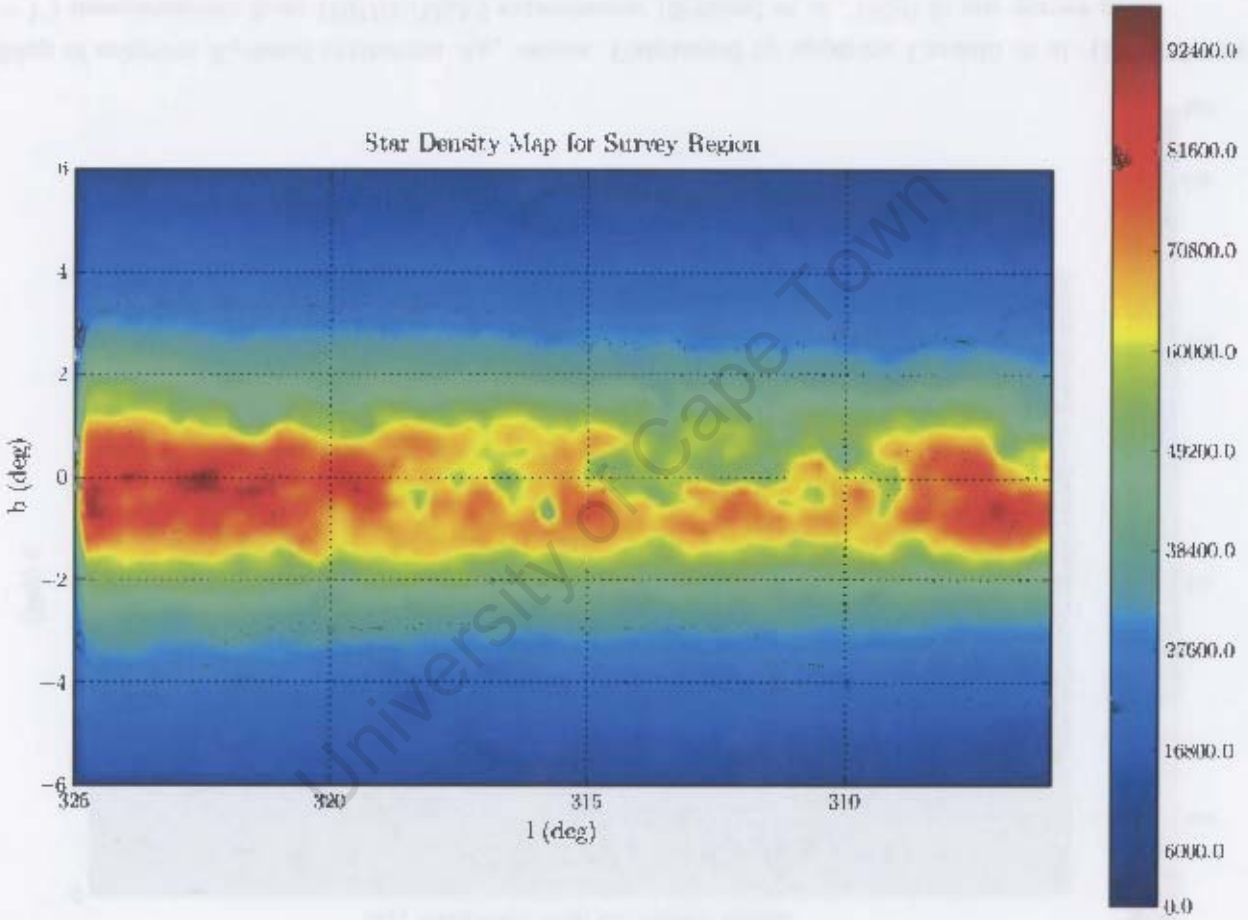


Figure 2.3: Map of star number density measurements from 2MASS PSC in our survey area. Densities are measured in number of stars with $K_s < 14^m$ per square degree.

After creating the flat-field, each frame is divided by the flat-field, which is normalised to unity, to remove any visual defects arising due to physical imperfections or blemishes on the detector. The flat-fielded dithered twenty-five frames (for each band) must then be sky subtracted and dark current subtracted. Lastly they are combined (in each band) to produce a single image (for each band), ready for analysis

The image processing involving frame combining, flat-fielding, sky subtraction, and dark current subtraction was done using the SIRIUS package, an automated data reduction pipeline[2] written for IRAF (Nakashima et al., private communication).

## 2.4 Astrometric and Photometric Calibration

### 2.4.1 Astrometric Calibration

Astrometric calibration of fields is done to assign positional information to an image, usually in the form of a World Coordinate System (WCS) update to the image header. The astrometry was made into a semi-automatic process through various PYTHON programs written by myself to improve the manual procedure. The overview of the method for a field needing calibration is shown in point form and then explained:

- $8' \times 8'$ WCS-aligned NIR calibration image downloaded,
- Corresponding catalogue containing all stars in that image downloaded,
- Plate solutions for co-ordinate aligning our field with calibration image calculated (*ccmap*),
- Transformation to WCS co-ordinates applied.

The first step involved downloading a calibration image of the field (at the RA and Dec of the field needing calibration) from the 2nd generation of Digitized Sky Survey (DSS II) images hosted at the European Southern Observatory (ESO) as well as the corresponding object catalog (the 2MASS Point Source Catalogue (Cutri et al., 2003)) from the 2MASS server at the Centre de Données astronomique de Strasbourg (CDS) using JSKYCAT. The IRAF task *ccmap* is used to compute plate solutions using matching pixel and celestial co-ordinate lists. To create this list a PYTHON script was written. This script simply allows the user to click on a star in the calibration image, and select the corresponding star in the un-calibrated IRSF image using the IRAF task *imexamine* (see example in Fig 2.4). The stars chosen were always stars of photometric

[2]The SIRIUS data reduction pipeline is publicly available online from http://optik2.mtk.nao.ac.jp/~yas/pipeline/siriuspipeline.html

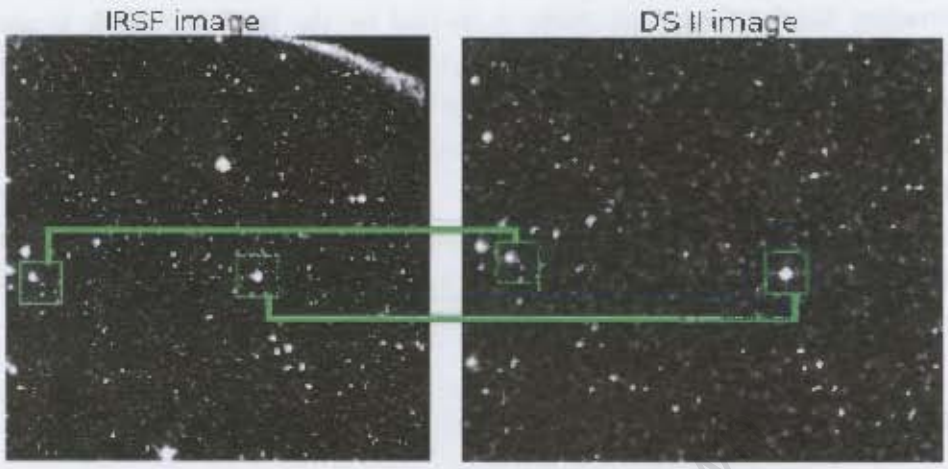


Figure 2.4: An example of an IRSF uncalibrated image (left) alongside a calibrated DS II image (right). Two pairs of matching stars are boxed in each image as examples of matching stars that can be used in astrometric calibration

quality (denoted by 'AAA' in the 2MASS PSC). After a list of matching stars has been created (usually 6 - 8 stars across the image), the list is written automatically to file, ready as input for *ccmap*. The output of *ccmap* is to assign the matched WCS to the IRSF image.

### 2.4.2 Photometric Calibration

In order to extract sources or do any meaningful photometry on the now astrometrically-calibrated image, it is necessary to calculate the magnitude zeropoint. The magnitude zeropoint is simply the offset between the instrumental magnitude and the correct magnitude. Typically, standard stars are observed (for which magnitudes are well known) on the night of observations, and then comparison of the instrumental magnitude of the standard stars with the correct magnitude gives an offset which is the magnitude zeropoint.

However, observing standard stars requires extra observing time, which we plan to minimise. An alternative method for photometric calibration is done by comparing the 2MASS PSC magnitudes for stars in our image with the instrumental magnitude for the corresponding stars that we measure. The procedure for doing photometric calibration is summarised and then explained:

- All photometric stars in the 2MASS catalogue and corresponding image found using *ccfind*
- Aperture photometry done on stars using *phot*
- Aperture correction used to calculate magnitude zeropoint

On the aligned image, the IRAF task *ccfind* was run to locate all the photometric stars in the 2MASS catalogue based on their celestial co-ordinates and the WCS updated image. The output is a list of the objects found which can then be filtered and passed as input to the *phot* task in the *daophot* package. *phot* does aperture photometry, calculating accurate centres, sky values and (instrumental) aperture magnitudes for the filtered list of objects. The output file of photometry for each object in the list is again filtered and then combined with the output from the *ccfind* task.

The aperture photometry was done using twenty apertures, ranging in size from 2.5 pixels to 20 pixels. A curve of growth was plotted to determine the asymptotic value at which the aperture magnitudes approach a total magnitude for each object. The magnitude for a specific aperture (used for all stars in the field) was then corrected according to the curve of growth to obtain a total instrumental magnitude for each star. This total instrumental magnitude could then be compared with the 2MASS catalogue magnitude for each star, taking into account a small correction factor due to the imperfect IRSF/2MASS filter match (Nakajima et al., 2008). Plotting the offsets between instrumental magnitudes and 2MASS magnitudes, and taking the mean then gave the magnitude zeropoint for each field.

Aperture-corrected photometry was used instead of a more conventional approach of fitting a point spread function (PSF) to each star, and calculating the magnitude within that PSF. This is because in crowded fields, the wings of the PSF profile can be affected by flux from nearby stars, thereby giving an inaccurate measure of the true brightness of the star. When doing aperture photometry, a fixed aperture that is small enough to encompass the majority of only the star of interest can be used, and simply corrected by the curve of growth difference between the fixed aperture magnitude and the asymptotic total magnitude.



## 2.5 Galaxy Identification

### 2.5.1 Field Analysis and Identification of Galaxies

I identified galaxies by inspection from composite false colour images rather than by looking at single wavelength images. Using single-band images to search for galaxies is complicated due to the different depth attained in each filter, the colour completeness of the survey and how this varies as a function of extinction. Some of the effects will be quantified in Chapter 3. Accordingly, for each field a composite $JHK_s$ false colour image was created. The colour image was created by resizing the $J$ and $H$ to the size of the $K_s$-band image and then aligning the resized $J$- and $H$-band images with the $K$-band image using IRAF packages *geomap* and *geotran*.

The three images were then sky-subtracted, and the IRAF package *rgbsun* was used to assign

the $K_s$-band image a red colour palette, the $H$-band image a green palette, and the $J$-band image a blue palette, and overlay these three colour images to produce a single false RGB colour image.

The sky subtraction was done by loading the image for viewing, setting the contrast and brightness to a high level (showing up any patches of pure sky), then using IRAF task *imexam* to measure the sky level in a few patches of sky, calculating the average sky value from these measurements, and then using IRAF task *imarith* to subtract the average sky value from the image. Since the process is slow, a PYTHON program was written to automate the whole procedure from resizing through to colour compositing. The colour images were then scanned by eye. At lower Galactic latitude, the galaxies appear reddened due to the vast increase in dust and gas close to the GP, which scatter shorter wavelengths more than longer wavelengths, resulting in more long wavelength flux being detected. This made them harder to find by eye since we detect very little flux in the $J$-band. Furthermore, star crowding close to the GP makes finding galaxies there difficult (*cf* Fig. 2 from Kraan-Korteweg 2005). Further from the GP, as the dust contamination decreases, the reddening decreases, although the star crowding increases closer to the GB (see Fig. 2.3).

The total number of galaxies identified (including 9 candidates) in the 162 scanned fields, is 115. See Appendix B for details.



## 2.6 Galaxy Photometry

Initially, "postage stamps" of dimension $1' \times 1'$ of all galaxy candidates are made. The smaller dimension of stamps when compared with whole fields, makes stamps quicker to analyse photometrically. Star removal is then performed on all stamps, and any remaining blemishes are cleaned. Finally, photometric analysis of all cleaned stamps using Source Extractor (SE) (Bertin & Arnouts, 1996) is performed, resulting in an output catalogue of photometric data for all galaxy candidates.

### 2.6.1 Postage Stamp Creation

The term "postage stamp" or simply stamp, refers to a $1' \times 1'$ portion of an image and contains a galaxy candidate usually in the centre of the stamp. All galaxies found fitted within a stamp. It serves as a quick look image for a galaxy without having to look for the galaxy in a typical $\sim 8' \times 8'$ field. However since it is created initially from a subset of a larger IRSF Flexible Image Transport System (FITS) image, it can be used for extracting photometry in the same way that photometry can be extracted from a large image. In addition, since it is only $\sim 1.5\%$ the area

of a typical field, there are far fewer stars in the stamp, which makes star removal a far quicker process (described in Sect. 2.6.2).

Creating the postage stamps for all the galaxy candidates had to be done manually. This is because at the time when the galaxy identification was done, WCS information was not present for the relevant fields, meaning no coordinates could be recorded for the galaxy candidates. If real physical coordinates had been known for the galaxy candidates, it would have been possible to automate the extraction of a $1' \times 1'$ stamp around the galaxy position in a field.

I wrote a PYTHON script to make the stamp creation a faster process. The script allows the user to enter a field name and the number of galaxies in that field, after which it opens the chosen field for viewing. The user then simply has to hover the cursor over the approximate centre of a galaxy candidate and press the '**,**' key followed by the '**q**' key. The script then creates a postage stamp centred on the galaxy candidate in each of the $J$, $H$, and $K_s$ bands since the fields have already been aligned and scaled for all three bands (see Sect. 2.5.1). Some galaxies are near to the edge of an image. In such cases, the program creates a postage stamp with the galaxy candidate offset from the centre so that the edge of the postage stamp coincides with the edge of the larger image.

All the postage stamps of the galaxy and galaxy candidates in $J, H, K_s$ and RGB false colour are shown in Appendix C.

### 2.6.2 Star Removal - Why and How?

Once the image is reduced and calibrated it is possible to begin extracting sources and their photometry using a software tool (the most recent and reliable of which is Source Extractor). While the photometry yielded by SE is very accurate, it breaks down when trying to do photometry in crowded fields. The output from SE is also very sensitive to user-defined initial parameters such as detection threshold, background estimation and Kron aperture parameters. Careful fine tuning of such parameters is necessary to ensure correct output.

SE defines a crowded field in the following way: within a certain square area of the image, the mean and standard deviation of the distribution of the pixel values is calculated. The extreme outlying values are discarded and the median and standard deviation recomputed. The process is repeated until all pixel values lie within $\pm 3\sigma$. If $\sigma$ dropped by more than 20% per iteration, the field is considered crowded (Da Costa 1992). Closely adhering to this procedure for determining crowding was not necessary, since a simple glance at the star density in our fields shows obvious star crowding.

The star crowding generally causes the extracted galaxy magnitudes to be incorrect, since in most cases the galaxy is partially obscured by a number of stars, often bright. It is thus

essential for stars to be removed or masked from the images in order for accurate photometry to be done. An adapted procedure for crowded field photometry was used, in conjunction with the IRAF routine called KILLALL (Buta & McCall, 1999) to remove the stars. An overview of the process is shown in Fig. 2.5.

The process begins by using the IRAF task *daofind* to find all objects in the field above a certain threshold (in $\sigma$) above the local background noise level. The background noise level can be estimated by taking a few readings of background counts in different parts of the image and estimating the standard deviation. Alternatively a precise calculation can be done, but I found that an estimated value was amply good enough for detecting objects. Standard deviation values were found to typically be:

$$\begin{aligned} \sigma_j &\simeq 1.2 - 1.5 \text{ counts} \\ \sigma_h &\simeq 2.3 - 2.7 \text{ counts} \\ \sigma_k &\simeq 4 - 4.5 \text{ counts} \end{aligned}$$

I used a feature detection threshold of between $3\sigma - 5\sigma$ depending on the wavelength. In particular the $H$-band required a very low detection threshold otherwise many faint stars were not detected. *daofind* then produces a catalogue of the objects found.

The next step is to run the IRAF task *phot* which generates a file with accurate centres, sky values and aperture photometry for single or multiple apertures for all the objects in the *daofind* catalogue. *phot* requires input parameters such as the background noise level determined earlier as well as the full-width half-maximum (FWHM) of the PSF. Determining the PSF FWHM from the image requires measuring the FWHM of several stars (I used between 4 and 10) in the field using the IRAF task *imexamine*. The stars used for measuring the FWHM PSF were chosen according to the following criteria:

- Not too large/bright - no saturation or refraction spikes
- Not too small/faint - need a good signal to noise ratio (S/N) to ensure a correct FWHM
- Not close to bright stars and not blended with other stars

In order to measure the FWHM of all the fields in each band, I wrote a PYTHON script to open each image automatically, allow the user to select a few stars fitting the above criteria, calculate the average FWHM of the selected stars, and save the results of all the fields in a file. The output list shows that the FWHM values for all the fields in all bands range between approximately $2.25 - 4.25$ pixels which, for the IRSF pixel scale of 0.45 arcseconds per pixel, translates into approximately $1 - 2$ arcseconds.

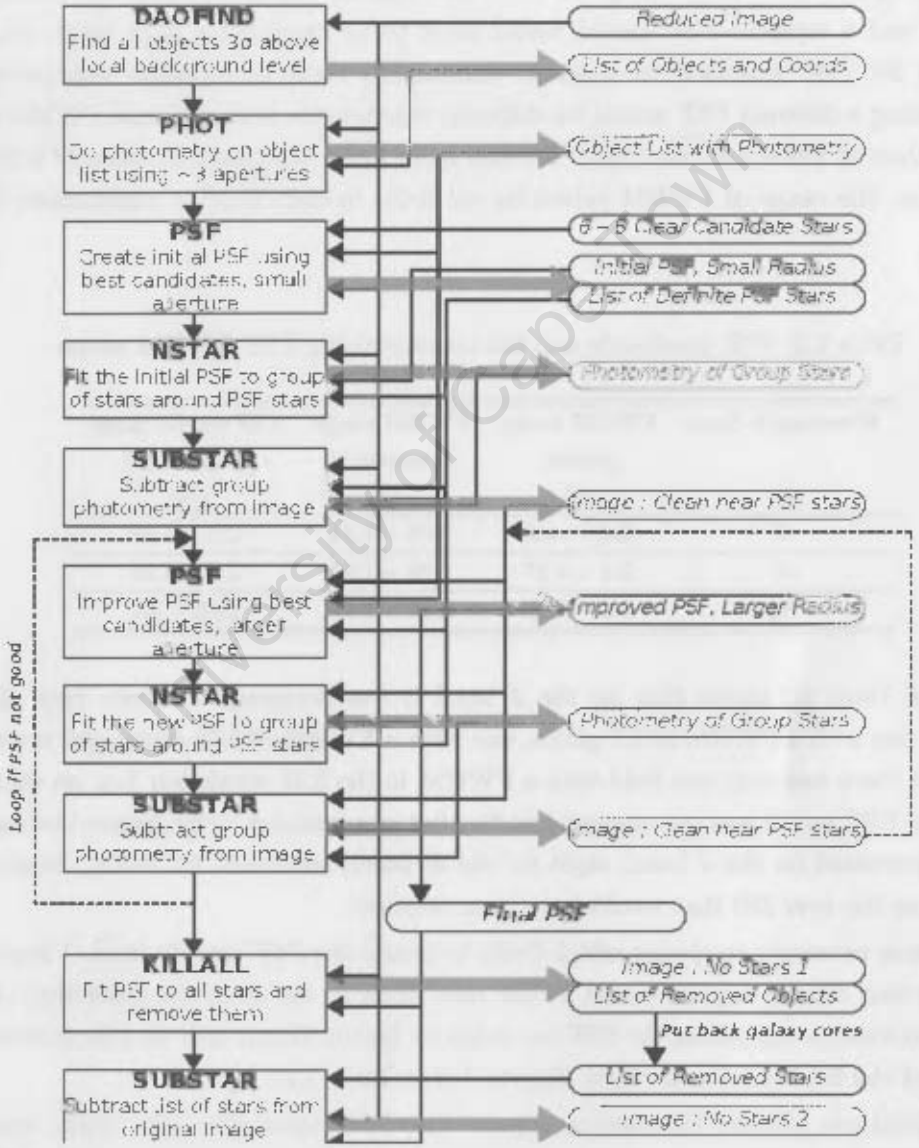
DAOFIND
Find all objects 3σ above local background level
Reduced Image
List of Objects and Coords
PHOT
Do photometry on object list using ~3 apertures
Object List with Photometry
PSF
Create initial PSF using best candidates, small aperture
6 – 8 Clear Candidate Stars
Initial PSF, Small Radius
List of Definite PSF Stars
NSTAR
Fit the Initial PSF to group of stars around PSF stars
Photometry of Group Stars
SUBSTAR
Subtract group photometry from image
Image : Clean near PSF stars
PSF
Improve PSF using best candidates, larger aperture
Improved PSF, Larger Radius
NSTAR
Fit the new PSF to group of stars around PSF stars
Photometry of Group Stars
SUBSTAR
Subtract group photometry from image
Image : Clean near PSF stars
Loop if PSF not good
Final PSF
KILLALL
Fit PSF to all stars and remove them
Image : No Stars 1
List of Removed Objects
Put back galaxy cores
SUBSTAR
Subtract list of stars from original image
List of Removed Stars
Image : No Stars 2

### Point Spread Function Model

To proceed with removing the objects detected earlier, it is necessary to create a model PSF for the field of interest. However, since there are approximately 70 fields containing galaxy candidates, and a separate PSF model would need to be created for each band, that would require over 200 PSF models to be created. Fortunately there is a quicker alternative, which requires making a different PSF model for different wavelengths with different FWHM values. I created a subset of PSFs, per band, with FWHM from $2.25 - 4.5$ pixels (in steps of 0.25 pixels). To be precise, the range of FWHM values for all fields in each band is summarised below in Table 2.2:

Table 2.2: NIR passbands and the corresponding PSF FWHM values

| Wavelength band | FWHM range [pixels] | FWHM range [arcseconds] | PSF model range [0.25 pixels] |
|---|---|---|---|
| (1) | (2) | (3) | (4) |
| $J$ | $2.41 - 4.3$ | $1.08 - 1.94$ | $2.5 - 4.25$ |
| $H$ | $2.4 - 4.27$ | $1.08 - 1.92$ | $2.5 - 4.25$ |
| $K_s$ | $2.1 - 3.75$ | $0.95 - 1.69$ | $2.25 - 3.5$ |

Column 4 of Table 2.2 shows that for the $J$ band it was necessary to create only eight PSF models, i.e. one with a FWHM of 2.5 pixels, one with a FWHM of 2.75 pixels and so forth. For the $K_s$ band there was only one field with a FWHM in the 3.75 pixels bin (i.e. an outlier) and so a separate PSF model was not created just for that one instance. This means that eight PSF models were created for the $J$ band, eight for the $H$ band, and seven for the $K_s$ band which is far fewer than the over 200 that would have been required.

Next it was necessary to choose which fields to create the PSF models from. I decided that fields in low star density regions would be the best fields to use since the possibility of finding good isolated stars for modelling the PSF on would be higher than in heavily star crowded fields. Thus most of the fields used came from Region 7 (see Table 3.2).

Once a field was selected for creating a particular PSF model from, the image was opened and several candidate stars were chosen according to the criteria mentioned earlier. The IRAF task *psf* was used to create the model. Examining the various profile functions for fitting a PSF (e.g. Gaussian, Lorentzian, Penny) it was clear that the IRSF PSF is best fitted by a Gaussian profile. A complex incremental approach to building a PSF can be used to construct a PSF in a typical field that allows for a wide range of star sizes being removed. However, since postage stamps have been created of all galaxy candidates, it is no longer necessary to create PSF models

to fit all the stars in a field, but simply to create a PSF that fits the stars in a postage stamp. This is simpler because in a postage stamp image, most stars are easily modelled by a smaller PSF, since it is unlikely that a very large star (greater than 24 pixels radius) will appear in a postage stamp. For the smaller, simpler PSF, I used a 15-pixel fitting radius (6.75″). For this smaller PSF, it is not necessary to use the incremental method mentioned above. This is because it is far easier to find in a field a good star isolated by 15 pixels than by 24. Thus for removing stars from postage stamps a single iteration of *psf* was used with a fitting radius of 15 pixels. In addition, since it is easier to find isolated stars in a less crowded field with the same FWHM as a more crowded field, stars in low star density fields were used for creating the different FWHM PSF models.

### Removing stars with *killall*

Now that PSFs for all wavelengths and FWHM values have been created along with postage stamps, it is simply a matter of removing the stars using IRAF routine *killall*. This routine uses the PSF, as well as all the parameters used in creating the PSF such as PSF radius, PSF model type, standard deviation of the background, FWHM and detection threshold. It starts by using *daofind* to find stars, then running *phot* and then attempting to fit the PSF we have created to the actual stars it has found. The results of all the stars or objects removed and their properties such as $x$ and $y$ coordinates, magnitude and local sky value are saved in a file. Fig. 2.6 shows a typical stamp before and after *killall* has been run.

In most cases, *killall* recognises the core of the galaxy in the current stamp as an object which requires removing, since the core very often fits an elliptical Gaussian PSF closely. For this reason, after a stamp has had the stars removed, it is necessary to replace the core of a galaxy that has been removed. This is done by going to the *killall* results file and finding the entry that matches the coordinates of the galaxy core, and removing this entry. We are then left with a results file of all objects except for the galaxy core. We can now use the edited results file, the PSF and the original image as input for the IRAF task *substar*. This task uses the results file to find objects for removing, and uses the PSF to fit them. Since the galaxy core is no longer in the results file, *substar* skips over it and removes only the stars, and saves the output image. The whole procedure is shown in the bottom section of Fig. 2.5, and Fig. 2.6 shows the star removed image with galaxy core replaced.

### Blemish editing

In most cases, the PSF fitting is not perfect, because the PSF model we created does not exactly match the true PSF of the stars. This often results in small 'holes' with very negative flux being

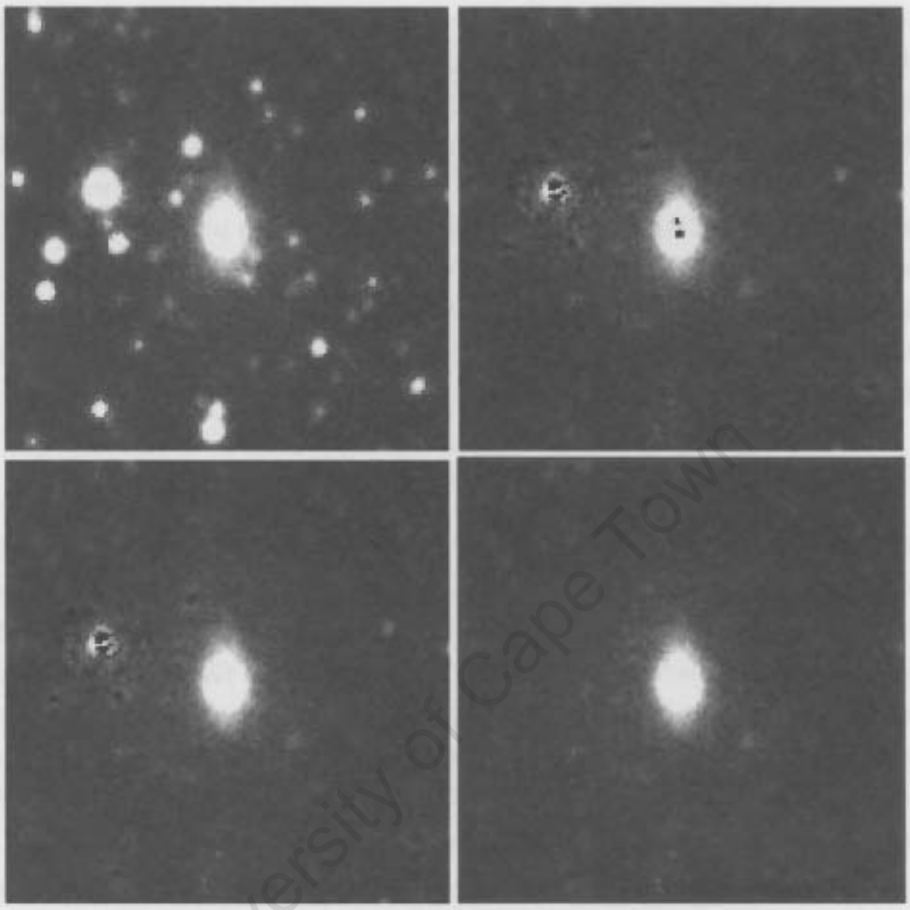

Figure 2.6: The star removal process for a typical postage stamp (ID number 111 in Table A.1). *Top left*: Original image, *Top right*: After running *killall* - galaxy core removed, *Bottom left*: Galaxy core replaced, *Bottom right*: Blemishes and holes edited - final image.



left where a star used to appear. In the case of very large or saturated stars, the PSF does not match very well, and large unsightly 'blemishes' will result. These holes and blemishes can affect the photometry of a galaxy, and so must be removed if we are to get accurate photometry for the galaxies.

For the blemish editing, IRAF task *imedit* was used. I used this task in interactive mode (as opposed to passing a list of blemishes for automatic editing) since a lot of care was required to remove blemishes near galaxy cores. A circular (or square) aperture is used to select the region that requires editing. A small annulus around the aperture is used to calculate the background level. This background level is then used to replace the pixel values within the aperture. In this way, using for example a 5-pixel aperture with 2-pixel sky annulus will comfortably replace a

3-pixel hole with sky values surrounding the hole.

Where holes obscure parts of a galaxy, special care must be taken to minimise the aperture size, so that if a 2-pixel hole is removed, 2-or maybe 3-pixel aperture is used. This is important as we need to get the most local background (i.e. galaxy) values as possible when replacing the hole. Using a large aperture would less accurately interpolate the replacement region because there is a larger background variation.

Where large residuals (blemishes) remain from saturated stars the editing is more difficult. In these cases a large aperture is required (typically a pixel or 2 pixels larger in radius than the PSF radius). If the blemish is obscuring the galaxy, it is very difficult to remove it, but again by using small aperture blemish corrections to the edges of the blemish, its size can be reduced.

### 2.6.3 Galaxy Photometry with Source Extractor

Having completed the star removal and blemish editing, one can now analyse the images photometrically. This is done by running each image through Source Extractor (SE). SE is a software tool for extracting sources from images and performing photometric analysis on all sources. SE is one of several source extraction and photometry tools available, and was chosen for its ability to process images very quickly with good accuracy, since this is what is needed when handling large numbers of files. The following explanation is based on the software authors' original documentation.

The operating procedure of SE is shown in Fig. 2.7, and summarised in five steps. The procedure begins by estimating the background level and variability, and removing it from the image. Object detection follows by setting a detection threshold, and finding consolidated groups of pixels above that threshold. Objects that are blended are then separated by the process of deblending. The image is then scanned for spurious detections, which are then removed. Finally, photometry is done on all astronomical objects in the image to return the position, magnitude, surface brightness, and other photometric parameters in a catalogue. Each object is also then classified as either a star or galaxy based on a neural network algorithm.

#### Background Estimation

SE begins by dividing the image into a grid with the mesh size specified by the user parameter `BACK_SIZE`. It then makes an initial pass through the image, estimating a local background in each grid mesh using a combination of $\sigma$ clipping and mode estimation. This method is described in Da Costa (1992). The basic procedure is to iteratively clip the histogram of pixel data values in the local background until convergence at $\pm 3\sigma$ around the median is reached. If $\sigma$ changed by more than 20% during the clipping, the field is considered crowded, otherwise it is

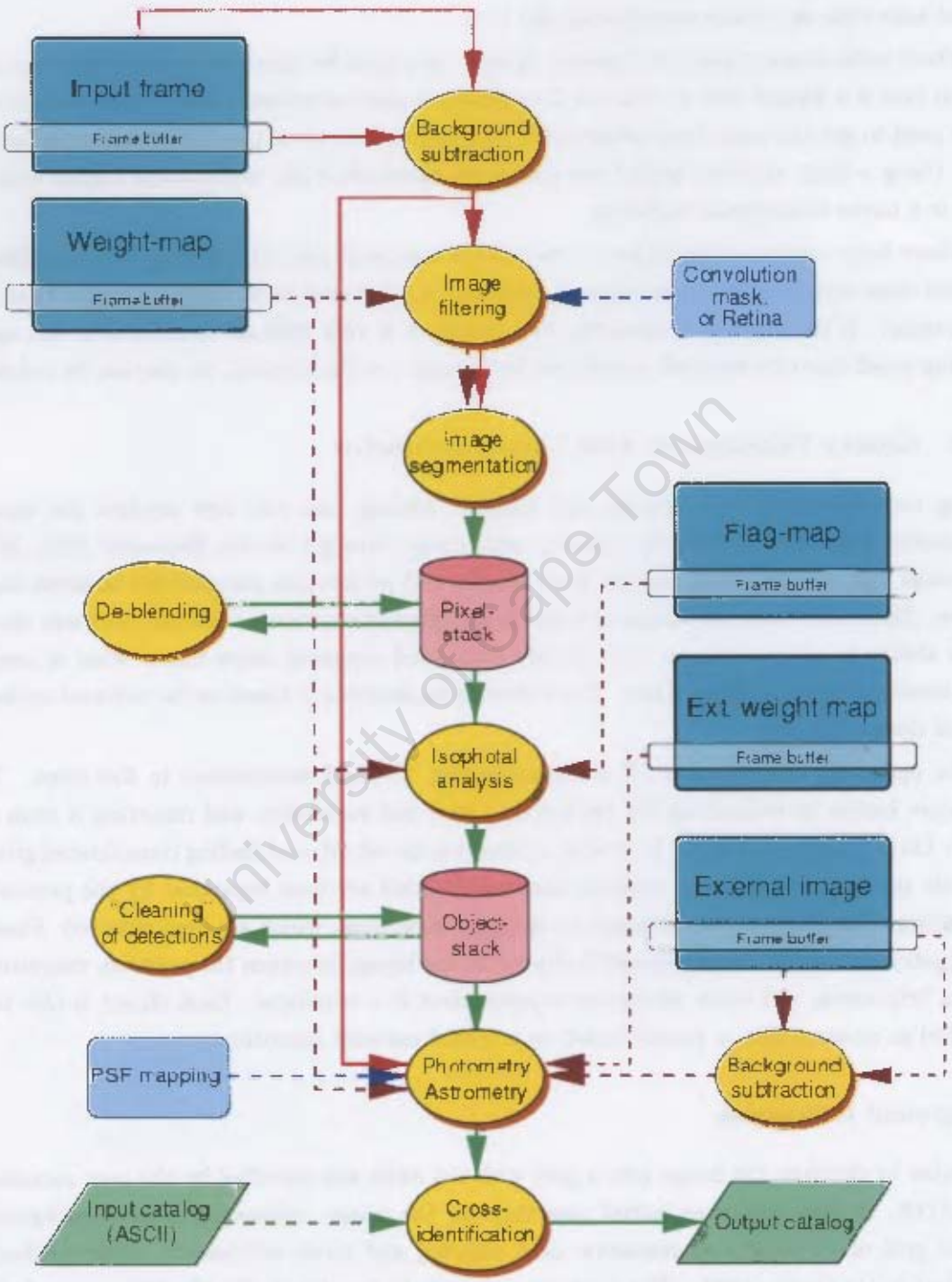




Figure 2.7: Flow diagram of operating procedure for Source Extractor (reproduced with permission from Bertin's Source Extractor Manual - available online at http://terapix.iap.fr/soft/sextractor)

not considered crowded. In the latter case, the background value is simply taken as the median of the clipped histogram of pixel values. In the case of the former, the mode is estimated by the following expression[3]:

$$\text{Mode} = 2.5 \times \text{Median} - 1.5 \times \text{Mean} \tag{2.1}$$

After the local background has been estimated over the whole grid, a median filter is applied to reduce the effect of local over-estimates of the background due to bright stars. The result is an overall background map with bicubic-spline interpolations between the local backgrounds of each grid mesh. The user's choice of grid mesh size is important. If the mesh size is too small, the background map is too heavily influenced by noise and actual objects in the image. In particular, portions of extended objects may be attributed to the background if the mesh size is too small. Conversely, a large mesh size suppresses the small scale variations in the background. Care must therefore be taken when deciding the `BACK_SIZE` parameter.

It was found for this work that a mesh size of 128 pixels with a filter size of 5 meshes was optimal when working with full field images (i.e. $7.8' \times 7.8'$). However, photometry was not performed on field images, but rather on postage stamps, the dimensions of which are only $133 \times 133$ pixels. Thus a background mesh size of 128 pixels does not make sense. To effectively model the background correctly on such small images, a mesh size of $\leq 32$ pixels would be needed. However, such a small mesh size makes the background very sensitive to flux objects in the image. It was decided that the background does not vary significantly enough on such small scales. A mesh size of 128 pixels was decided upon because this results in a constant background value. After a background map is calculated, it is subtracted from the image in order to extract accurate photometry for sources.



### Thresholding - Object Detection

Any astronomical object must be detectable as a connected group of pixels which are later processed as an object for photometry. A grouping of pixels is defined as any pixels which, above the local detection threshold, are connected either at their sides or vertices. SE needs the user to input a detection threshold via the `DETECT_THRESH` parameter. This is usually done in units of the standard deviation $\sigma$ of the background. For our photometry, a detection threshold of $2.5\sigma$ above the background level was used. In addition, a $3 \times 3$ pixel filter mask was used to improve detection of faint sources.

[3]See Bertin's SE User's Manual

### Deblending - Separating Objects

Initially, detected objects may overlap and be confused as a single object. SE employs a deblending algorithm to separate groups of pixels into separate objects. The algorithm works by calculating the light profile of the blended object above the detection threshold (see Fig. 2.8). The algorithm then works down from the top of the profile until it reaches a saddle point. At this point a new branch may be made if there is sufficient flux (a fraction $\delta_c$ of the total flux) under that peak, and sufficient flux under the peak on the other side of the saddle point. If a branch is created by satisfying the above criteria, the original object is split into two separate objects, and the pixels are divided statistically. A faint pixel is fitted with a Gaussian and the flux contribution to each sub-object from that pixel is measured. The sub-object due the greater share of the pixel's flux then claims that pixel.

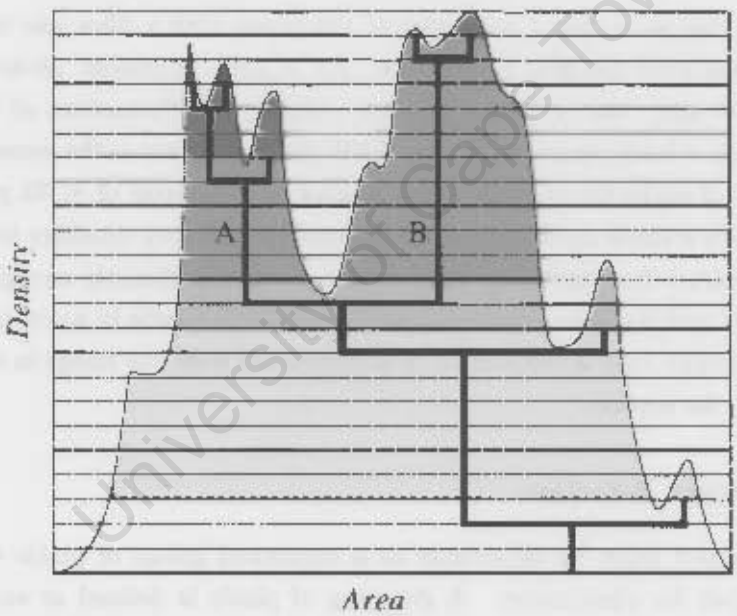




Figure 2.8: Schematic diagram showing a blended object's light profile and illustrating the deblending algorithm. See text for details. (Image reproduced with permission from Bertin's SE User's Manual)

Bertin & Arnouts (1996) found that a good value for the deblending contrast parameter was $\delta_c \sim 0.005$ after analysing galaxy images. They further suggest that a good value for the number of deblending thresholds is 32. Both these values were used in our analysis.

The boolean CLEAN parameter gives the user the option to have SE check the list of detected objects to remove any objects that are artifacts of bright nearby sources. That is, to check

whether each object would have been detected had its neighbours not been present. This is achieved by fitting a scaled Moffat profile to all neighbours, and subtracting the contribution from the wings of the Moffat profile to the object being checked. The Moffat profile is defined as

$$\frac{I(r)}{I(0)} = \frac{1}{(1 + k \times r^2)^{\beta}} \tag{2.2}$$

where $I(R)$ is the intensity at some radius $r$, and $I(0)$ is the central intensity. The parameter $\beta$ is a cleaning efficiency factor that controls the brightness of the Moffat profile wings and hence the degree to which neighbours contributions are cleaned. The wings are subtracted from the object being cleaned, and if the subtraction causes the object to drop below the detection threshold, it is removed from the list of detected objects. A factor of $\beta = 1$ was used for our analysis.

### Photometry

The photometry for the extracted objects can be calculated in four ways by SE. The first and simplest way is to use the isophotal approach, which simply measures the contribution from all the object's pixels in the isophotal area (defined by all object pixels above the threshold) and adds it up. This gives an ADU count which must be converted to a flux (electron count) via the gain. The gain depends on what type of instrument is used and the frame stacking method. There is therefore a relation between the instrument gain and the effective gain that is used to convert counts to flux. In our case of median frame combining, the effective gain relates to the instrument gain as follows:

$$\text{gain}_{\text{eff}} = 2 \times \text{N} \times \frac{1}{3}\text{gain} \tag{2.3}$$

where N is the number of stacked frames. In our data, each image was produced by stacking 25 frames, i.e. N = 25, and the instrument gain of the detector is gain = 5.0. Using Eqn. 2.3, the effective gain for our data is calculated to be $\text{gain}_{\text{eff}} = 83.33$.

The gain is used to convert the isophotal ADU counts to isophotal flux. The isophotal flux is then converted to a magnitude via the following relation:

$$\text{m} = 2.5 \times \log_{10}[(\text{flux} - \text{magzp}) \times \text{exp.time}] \tag{2.4}$$

where 'm' is the apparent magnitude, 'magzp' is the magnitude zeropoint and 'exp. time' is the exposure time in seconds of an individual frame.

The second option is to use the isophotal-corrected approach. This approach assumes all the objects in the image are roughly Gaussian due to atmospheric seeing. The object's flux is then not only the isophotal flux but also the contribution from the Gaussian wings. This approach is best suited to photometry of stars, and is less reliable for galaxies.

```
# Default configuration file for SExtractor 2.5.0
# EB 2006-07-14
#

#-------------------------------- Catalog ------------------------------------

CATALOG_NAME     test.cat       # name of the output catalog
CATALOG_TYPE     ASCII_HEAD     # NONE,ASCII,ASCII_HEAD, ASCII_SKYCAT,
                                # ASCII_VOTABLE, FITS_1.0 or FITS_LDAC
PARAMETERS_NAME  default.param  # name of the file containing catalog contents

#-------------------------------- Extraction ----------------------------------

DETECT_TYPE      CCD            # CCD (linear) or PHOTO (with gamma correction)
DETECT_MINAREA   5              # minimum number of pixels above threshold
DETECT_THRESH    2.5            # <sigmas> or <threshold>,<ZP> in mag.arcsec-2
ANALYSIS_THRESH  2.5            # <sigmas> or <threshold>,<ZP> in mag.arcsec-2

FILTER           Y              # apply filter for detection (Y or N)?
FILTER_NAME      /usr/share/sextractor/default.conv   # name of the file containing the filter

DEBLEND_NTHRESH  32             # Number of deblending sub-thresholds
DEBLEND_MINCONT  0.005          # Minimum contrast parameter for deblending

CLEAN            Y              # Clean spurious detections? (Y or N)?
CLEAN_PARAM      1.0            # Cleaning efficiency

MASK_TYPE        CORRECT        # type of detection MASKing: can be one of
                                # NONE, BLANK or CORRECT

#-------------------------------- Photometry ----------------------------------

PHOT_APERTURES   13.33, 22.22              # MAG_APER aperture diameter(s) in pixels
PHOT_AUTOPARAMS  2.5, 3.5       # MAG_AUTO parameters: <Kron_fact>,<min_radius>

SATUR_LEVEL      25000.0        # level (in ADUs) at which arises saturation

MAG_ZEROPOINT    20.398           # magnitude zero-point
MAG_GAMMA        4.0            # gamma of emulsion (for photographic scans)
GAIN             83.33            # detector gain in e-/ADU
PIXEL_SCALE      0.45            # size of pixel in arcsec (0=use FITS WCS info)

#------------------------- Star/Galaxy Separation ----------------------------

SEEING_FWHM      1.5            # stellar FWHM in arcsec
STARNNW_NAME     /usr/share/sextractor/default.nnw    # Neural-Network_Weight table filename

#------------------------------- Background -----------------------------------

BACK_SIZE        128             # Background mesh: <size> or <width>,<height>
BACK_FILTERSIZE  3              # Background filter: <size> or <width>,<height>

BACKPHOTO_TYPE   GLOBAL         # can be GLOBAL or LOCAL

#------------------------------- Check Image ----------------------------------

CHECKIMAGE_TYPE  APERTURES,BACKGROUND      # can be NONE, BACKGROUND, BACKGROUND_RMS,
                                # MINIBACKGROUND, MINIBACK_RMS, -BACKGROUND,
                                # FILTERED, OBJECTS, -OBJECTS, SEGMENTATION,
                                # or APERTURES
CHECKIMAGE_NAME  aper.fits,back.fits      # Filename for the check-image

#--------------------- Memory (change with caution!) -------------------------

MEMORY_OBJSTACK  3000           # number of objects in stack
MEMORY_PIXSTACK  300000         # number of pixels in stack
MEMORY_BUFSIZE   1024           # number of lines in buffer

#----------------------------- Miscellaneous ----------------------------------

VERBOSE_TYPE     NORMAL         # can be QUIET, NORMAL or FULL
```

Table 2.3: Example SE configuration script

object, and the photometry within that aperture should not be trusted.

### Automation of Photometry

To manually edit the configuration scripts for every image is very time consuming. An alternative, automated method is necessary for optimising survey strategy on the analysis side. A PYTHON wrapper for SE[4] was used to write a PYTHON script to automate the creation of configuration files and actual running of SE on all postage stamps. The PYTHON script I wrote works very efficiently and is shown in Appendix D. It allows the user to input the configuration details (gain, apertures, exposure time etc.) and a list of images, and runs with a time of less than thirty seconds for my 115 images. The result is a file with photometric and geometric parameters for each galaxy. This file contains the main results of this project and is discussed in Chapters 3 and 4.



[4]Courtesy of Laurent Le Guillou, 2005

# Chapter 3

# Results & Data Analysis

## 3.1 Galaxy Astrometry & Photometry

### 3.1.1 The Catalogue

Appendix A presents the catalogue of the galaxies and candidate galaxies (henceforth 'candidates') identified in this project. The galaxies were found by visual inspection of false colour NIR images (as discussed in Sect. 2.1.1). Objects that were identified as likely galaxies, and upon further examination were decided to be uncertain were classified as candidates. Visual inspection of colour NIR images, star/galaxy classification from Source Extractor (SE), and strongly blue $J - K_s$ colours helped separate candidates from definite galaxies. Galaxies labelled with a * symbol have uncertain magnitudes. Galaxies labelled with a † symbol are listed in the 2MASS Extended Source Catalogue. The catalogue contains 115 objects divided into 106 galaxies and 9 candidates. The determined parameters of these objects are:

**Column 1:** Identification number. This matches the numbering scheme on the stamp image catalogue presented in Appendix C

**Column 2:** Right Ascension (RA) and Declination (Dec) (J2000)

**Column 3:** Galactic longitude ($l$) and latitude ($b$)

**Column 4:** Interstellar extinction in the $K_s$-band ($A_{K_s}$) as determined from the Schlegel et al. (1998) Galactic reddening maps (see Sect. 3.1.4)

**Column 5:** Stellar number density measured in number of stars with $K_s < 14^{\mathrm{m}}$ per square degree as found in the 2MASS PSC (see Sect. 3.1.6)

**Column 6:** Galaxy (O) or Candidate (X) classification based on visual inspection of FITS images, SE star/galaxy classification and $J - K_s$ colour.

**Column 7:** Kron $J$-band magnitude and error. Not corrected for extinction.

**Column 8:** Kron $H$-band magnitude and error. Not corrected for extinction.

**Column 9:** Kron $K_s$-band magnitude and error. Not corrected for extinction.
**Column 10:** Central 3″-radius aperture $J$-band magnitude and error. Not corrected for extinction.
**Column 11:** Central 3″-radius aperture $H$-band magnitude and error. Not corrected for extinction.
**Column 12:** Central 3″-radius aperture $K_s$-band magnitude and error. Not corrected for extinction.
**Column 13:** Diameter ($D$) of the object in arcseconds in the $K_s$-band. This is determined from the relation $D = 2\times$ `KRON_RADIUS`$\times$`A`, where `A` represents the maximum spatial rms of the object profile in any direction, and `KRON_RADIUS` represents a numerical factor describing the extent of the semi-major axis of the Kron aperture.

### 3.1.2 Sample Completeness

The magnitude completeness limit was determined following the method described by Garilli, Maccagni & Andreon (1999). Magnitude completeness limits are often determined by investigating at what magnitude model galaxies with a similar surface brightness to real galaxies are still detected. The approach used here is different in that it is based on the detectability of the actual galaxies in our sample. In Fig. 3.1, the central 3-arcsecond aperture $K_s$-band magnitudes of the galaxies in our sample have been plotted as a function of central surface brightness. Certain galaxies are shown as circles, and candidate galaxies are marked as crosses. The dashed vertical line indicates the central surface brightness detection limit, and the solid fitted line is the best linear fit to the data (real galaxies only), with $+1\sigma$ and $-1\sigma$ plotted either side as dashed lines. The completeness limit is the intercept of the $-1\sigma$ line with the detection limit. The intercept of the fitted line with the detection limit is not used as the completeness limit, since any galaxy falling in the area to the right of the detection limit, under the completeness limit and above the continuation of the $-1\sigma$ line would still not be detected.



Objects far to the right of the fitted line have low surface brightness cores indicating that they are most likely late type spiral galaxies or irregular galaxies. Objects far left of the fitted line have high surface brightness at the core which either implies early type galaxies or unresolved merged stars (i.e. unlikely galaxies).

The completeness limit of the central $K_s$-band magnitudes measured from Fig. 3.1 is $K_s = 15.^{\mathrm{m}}55$ using the 3-arcsecond central aperture. Similarly, the completeness limits in the other bands are $J = 17.^{\mathrm{m}}34$ and $H = 16.^{\mathrm{m}}06$. The associated uncertainties listed in Table 3.1 were calculated as the sample standard deviation:

$$\sigma = \sqrt{\frac{\sum(x_i - \overline{x})^2}{N-1}}$$

Plotting Kron aperture magnitudes results in different completeness limits. This is because the Kron aperture encompasses the whole object, usually capturing more light than a 3-arcsecond central aperture. The spread in the Kron magnitudes is greater because of a higher possibility of contaminant light from nearby objects affecting the magnitude. The completeness limits are shown in Table 3.1 with the standard deviation. All values listed in Table 3.1 are based on fits to the data which exclude candidates. Skelton (2007) determined $K_s$ completeness limits in the Norma cluster, using the same method and with the same exposure time, to be $K_s = 15.^{\mathrm{m}}37$ for $5''$ aperture magnitudes and $K_s = 15.^{\mathrm{m}}10$ for Kron magnitudes. This is likely a result of lower levels of extinction and star crowding in that region than in our studied region.

Table 3.1: Completeness limits

| Passband | Aperture | Completeness Limit [mag] |
|---|---|---|
| (1) | (2) | (3) |
| $J$ | $3''$ Ap | $17.34 \pm 0.33$ |
| $H$ | $3''$ Ap | $16.06 \pm 0.32$ |
| $K_s$ | $3''$Ap | $15.55 \pm 0.34$ |
| $J$ | Kron | $16.31 \pm 0.77$ |
| $H$ | Kron | $14.90 \pm 0.80$ |
| $K_s$ | Kron | $14.72 \pm 0.75$ |



### 3.1.3 Comparison with 2MASS Photometry

In Sect. 2.1.2 the photometric properties of the SIRIUS camera on the IRSF were discussed and compared with the properties of the 2MASS and DENIS surveys. 2MASS makes use of the same passbands as the IRSF (although the actual wavelength of the filters is slightly different), making it ideal for a comparison of photometry. We will obtain better resolved images from the IRSF images, because of the superior resolution. The pixel scale for the IRSF is $0.45''$ pixel$^{-1}$, and $2.0''$ pixel$^{-1}$ for 2MASS. To illustrate this, postage stamps of three different galaxies (from different star density and extinction environments) are shown in Fig. 3.2 with the IRSF images in the top panel, and the corresponding 2MASS images in the bottom panel.

The IRSF images show a far higher signal to noise ratio (SNR), with clearer views of the galaxies. The increased apparent size and brightness is due to the longer integration time of the IRSF observations, allowing a deeper view than that offered by 2MASS. This is reflected in the completeness limits. The 2MASS Extended Source Catalogue (XSC) is complete to $K_s \simeq 13.^{\mathrm{m}}5$ at high latitudes (Jarrett et al., 2000), while the IRSF is complete to $K_s \simeq 14.^{\mathrm{m}}72$ (see above).

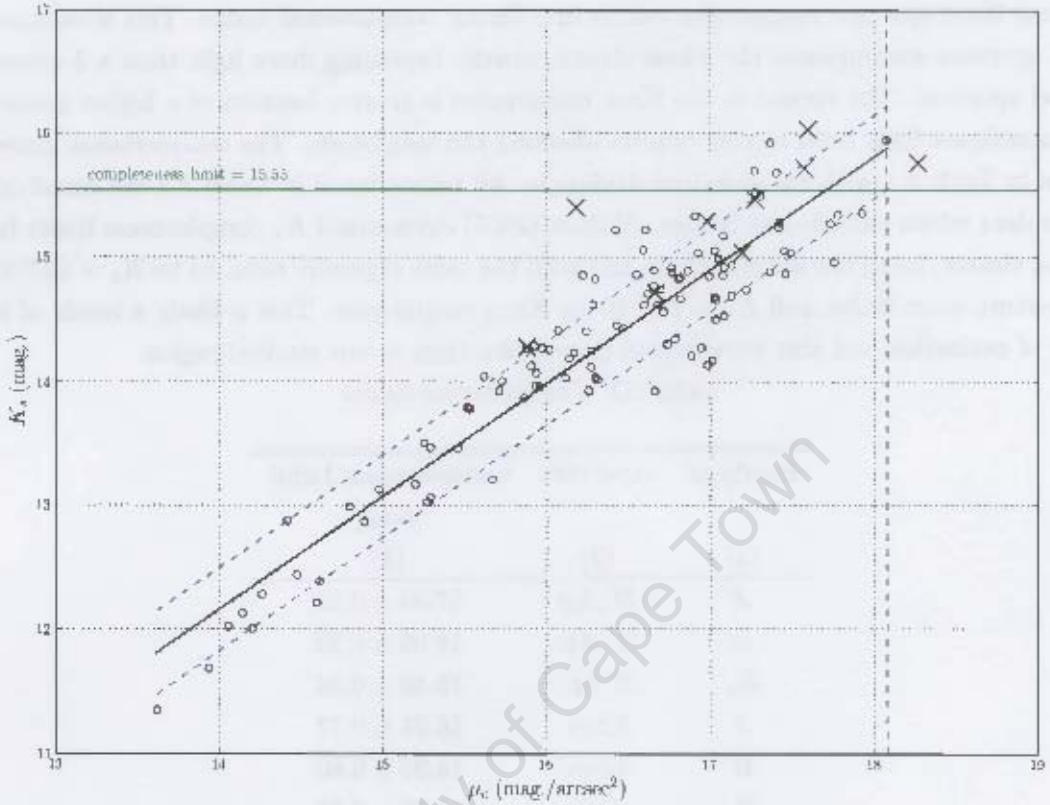


Figure 3.1: Central 3″ aperture $K_s$-band magnitudes vs. central $K_s$-band surface brightness. Candidates are shown as crosses. The solid line is a least squares fit to the certain galaxies. The intercept of the $-1\sigma$ linear fit line with the surface brightness detection limit gives the completeness limit for this type of aperture.



Twelve galaxies in our catalogue were found in the 2MASS XSC. Fig. 3.3 compares the NIR photometry for the twelve galaxies using central 5″-aperture magnitudes. These apertures are less susceptible to the addition of flux from foreground stars than Kron apertures. The error in $y$ was calculated as $\sigma_y = \sqrt{\sigma^2_{\rm 2MASS} + \sigma^2_{\rm IRSF}}$ and the error in $x$ is $\sigma_{\rm IRSF}$. The error in the IRSF magnitudes was calculated as a combination of the error in the magnitude zero point and the uncertainty in the noise distribution $\sigma_{\rm IRSF} = \sqrt{\sigma^2_{\rm noise} - \sigma^2_{\rm magzp}}$. The mean offset and standard deviation between the IRSF and 2MASS magnitudes are:

$$\Delta m^{J}_{IRSF-2MASS} = 0.^{\rm m}046 + 0.066 \qquad \sigma = 0.^{\rm m}228$$
$$\Delta m^{H}_{IRSF\ 2MASS} = 0.^{\rm m}028 + 0.074 \qquad \sigma\ \ 0.^{\rm m}258$$
$$\Delta m^{K}_{IRSF-2MASS} = 0.^{\rm m}073 \perp 0.088 \qquad \sigma - 0.^{\rm m}306$$

Figure 3.2: Three false colour postage stamp images of galaxies in our catalogue. The catalogue identification numbers are 45, 74 and 111 respectively. The top panel shows IRSF images and the bottom panel shows the corresponding 2MASS images. The scale of each stamp is $1' \times 1'$. See Appendix C for a complete list of all IRSF detected galaxies.



After carefully examining the central $5''$ of each galaxy, it was found that eight of the twelve galaxies had superimposed foreground stars which affected the central aperture magnitude. Calculating the average central magnitude difference of the other four unobscured galaxies gave:

$$\begin{aligned}
\Delta m^{J}_{IRSF-2MASS} &= -0.^{\mathrm{m}}052 + 0.054 \qquad \sigma = 0.^{\mathrm{m}}107 \\
\Delta m^{H}_{IRSF-2MASS} &= 0.^{\mathrm{m}}049 \perp 0.079 \qquad \sigma - 0.^{\mathrm{m}}148 \\
\Delta m^{K}_{IRSF-2MASS} &- +0.^{\mathrm{m}}019 \pm 0.090 \qquad \sigma = 0.^{\mathrm{m}}189
\end{aligned}$$

These results indicate that the IRSF magnitudes are fainter than the 2MASS magnitudes for twelve galaxies, although the differences lie well within $1\sigma$ of zero, implying the differences are not greatly significant. Skelton (2007) found a similar result for isophotal $K_s$-band magnitudes and suggested it was due to fewer stars superimposed on galaxies being resolved and removed in 2MASS images. Fig. 3.2 shows stars in the outer disk of the galaxies that are clearly resolved in the IRSF images, but not at all in the 2MASS images. These stars contribute flux to the 2MASS magnitude of the galaxies. This hypothesis is supported, albeit tenuously, by our data. The mean offsets drop when comparing the four galaxies which are not obscured by foreground stars, although the number statistics are poor.

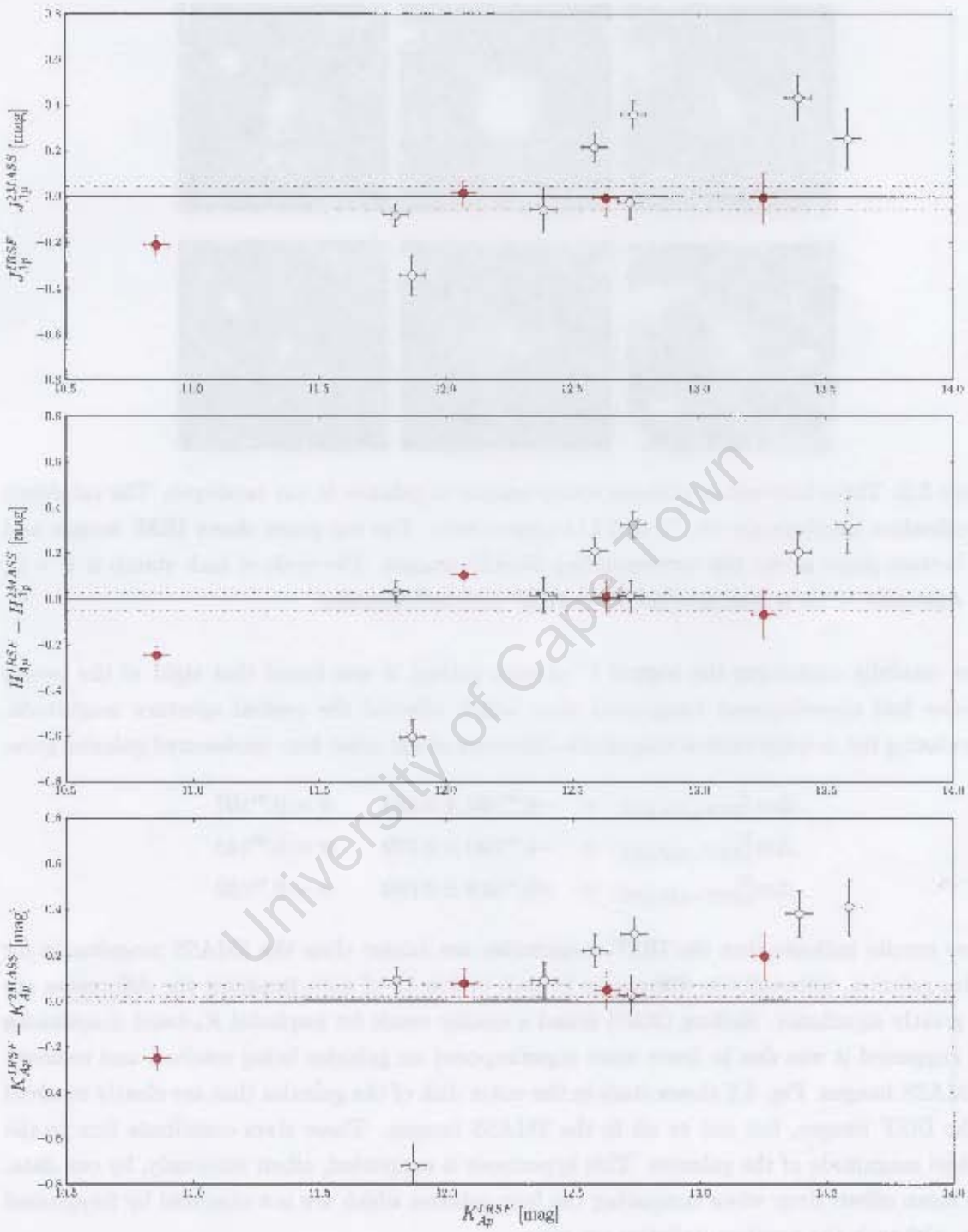




Figure 3.3: Comparison of 2MASS and IRSF central 5″-aperture $K_s$-band photometry for twelve galaxies. Galaxies with foreground stars superimposed on the central 5″ are shown as unfilled circles. The dashed line (black) shows the mean difference for all twelve galaxies, and the dashed line (red) shows the mean difference of the four galaxies which are not obscured by foreground stars.

### 3.1.4 NIR Extinction and Galaxy Colours

The observed 3″ aperture NIR galaxy colours $J-H$, $H-K_s$, and $J-K_s$ are plotted against the selective $K_s$-band extinction in Fig. 3.4. Galaxies which are certain and have accurate photometry are plotted as filled circles. Galaxies for which any of the $J$, $H$ or $K_s$ magnitudes are not accurate, because of imperfect star removal close to the core, are plotted as open circles. Error bars are shown, although in some instances are covered by the plot marker. The galaxy with $(A_{K_s}, J-K_s) \sim (0.^{\mathrm{m}}7, 1.^{\mathrm{m}}0)$ is bluer than expected for the associated extinction. Careful examination of the galaxy revealed nothing wrong with the photometry. It is most likely situated in a 'hole' in the extinction distribution, which explains why its colour is close to the typical colours for $A_{K_s} = 0$. The dashed line indicates the expected reddening according to Eqns. 3.11 and 3.12 (Cardelli et al., 1989). The $y$-intercept of the dashed line is taken from Jarrett et al. (2003) in their determination of typical NIR colours for galaxies of $J-H \sim 0.^{\mathrm{m}}73$, $H-K_s \sim 0.^{\mathrm{m}}27$ and $J-K_s \sim 1^{\mathrm{m}}$ in the 2MASS Large Galaxy Atlas (LGA) (Jarrett et al., 2003). We expect the galaxy colours to appear redder at greater extinction levels. A linear least squares trend line (solid line) is fitted (in each frame) to galaxies with exact magnitudes (plotted as filled circles) and confirms that galaxy colours appear redder at greater extinction levels. The solid line is extended as a dash-dotted line for comparison purposes. The linear trend lines were fitted following a Levenberg-Marquardt type algorithm:

$$y + v = mx + c$$

$$v = Ax - l$$

$$\text{where } \mathrm{A} = \begin{pmatrix} x_1 & 1 \\ x_2 & 1 \\ x_3 & 1 \\ \dots & \dots \end{pmatrix}$$

Minimising the sum of the squares of the residuals, i.e. $\frac{\partial v^T v}{\partial x} = 0$ gives

$$x = (A^T A)^{-1} \cdot A^T l$$

where $l$ is a column vector of the y-values. Since $A$ is known, $A^T$ can be calculated. $l$ is known and so we can solve for $x$ to determine the linear parameters of the gradient $m$ and the intercept $c$. To calculate the standard deviation of these parameters, a variance covariance matrix is calculated:

$$\begin{aligned} \Sigma_x &= \sigma_0^2 (A^T A)^{-1} \\ &= \begin{pmatrix} \sigma_m^2 & \sigma_{mc} \\ \sigma_{cm} & \sigma_c^2 \end{pmatrix} \end{aligned}$$

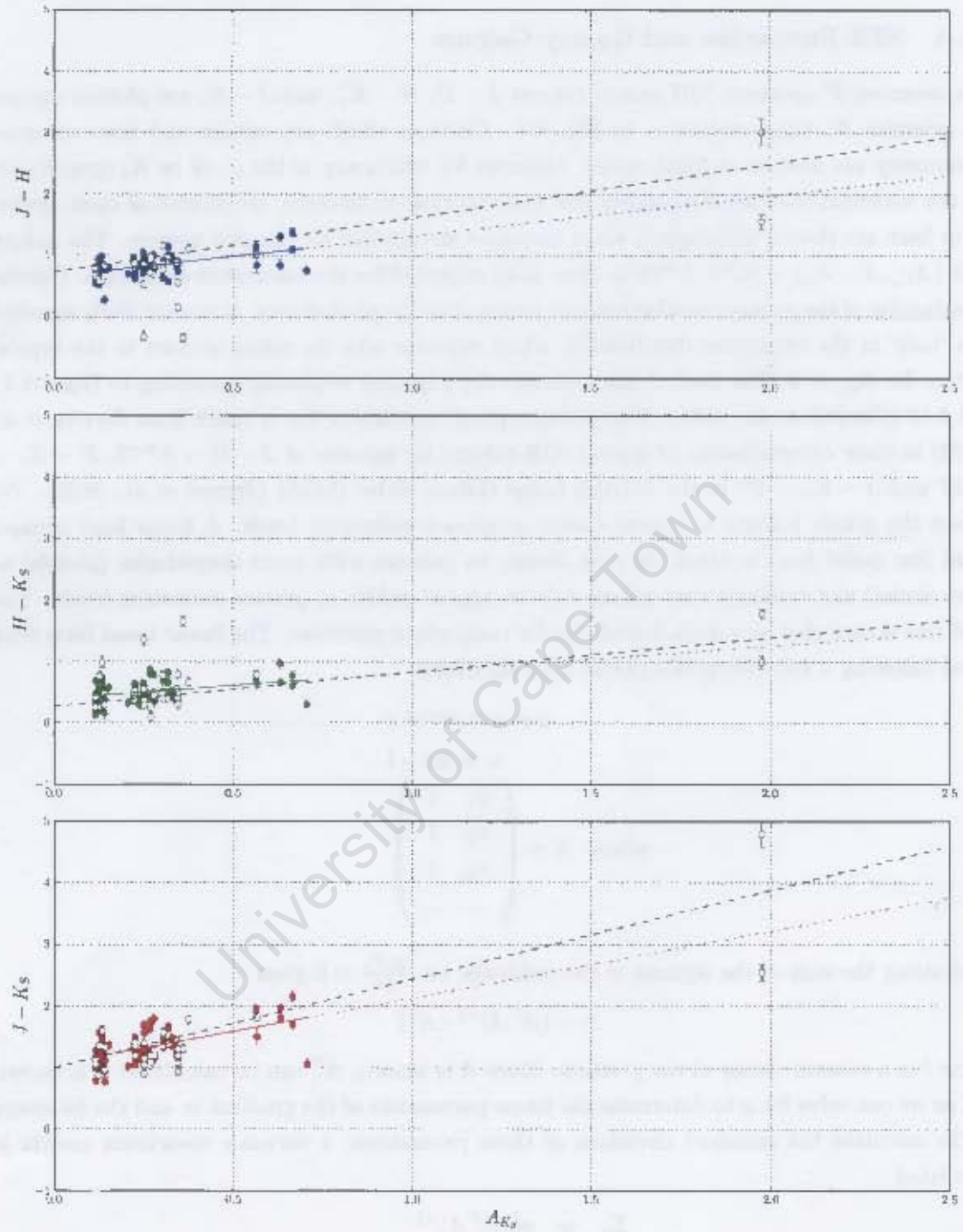




Figure 3.4: Observed NIR colours of our sample plotted against selective $K_s$-band extinction derived from the DIRBE/IRAS maps. Galaxies with accurate magnitudes are plotted as filled circles, and inaccurate magnitudes are plotted as open circles. The solid line in each frame is a least squares fit to the galaxies with accurate magnitudes. The dashed line indicates the expected reddening, with the zero point set at the mean intrinsic NIR galaxy colours as determined by Jarrett et al. (2003).

where

$$\sigma_0^2 = \frac{v^T v}{n-2}$$

is the standard deviation of observation of unit weight. Taking the square root of the variances $\sigma_m^2$ and $\sigma_c^2$ gives us, respectively, the standard deviation of the gradient and the intercept, $\sigma_m$ and $\sigma_c$. The least squares fit yields:

$$\begin{aligned} J-H &= (0.66 \pm 0.12) A_{K_s} - (0.66 \pm 0.03) \\ H \quad K_s &= (0.43 \pm 0.14) A_{K_s} - (0.40 \pm 0.04) \\ J-K_s &= (1.08 \pm 0.18) A_{K_s} - (1.05 \pm 0.05) \end{aligned}$$

The $y$-intercept in Fig. 3.4 indicates the NIR galaxy colours without extinction. From Jarrett et al. (2003): $J-H \sim 0.^{\rm m}73$, $H-K_s \sim 0.^{\rm m}27$ and $J \quad K_s \sim 1.^{\rm m}0$. The $J-K_s$ value for our data lies within $1\sigma$ of the Jarrett et al. (2003) value. The $J-H$ and $H \quad K_s$ values for our data are in reasonable agreement with the Jarrett et al. (2003) values, falling within $\sim 3\sigma$ difference. The expected reddening shown as a dashed line in Fig. 3.4 is derived from Cardelli et al. (1989) and is $J-H-0.88A_{K_s}$, $H \quad K_s = 0.56A_{K_s}$, and $J-K_s = 1.44A_{K_s}$. Comparison with the calculated slope fitted to the data in Fig. 3.4 shows that for $H \quad K_s$ our slope lies within $1\sigma$ of the expected reddening slope. For $J-H$ and $H-K_s$, the calculated slope lies outside of $1\sigma$ below the expected slope. This suggests an overestimate of the extinction for our data.

### Extinction correction

The NIR colour of galaxies in our sample can be used to derive an independent estimate of extinction at low Galactic latitudes. This is useful because the DIRBE/IRAS reddening maps are not calibrated at low latitudes (Schlegel et al., 1998), although they are the best existing approximation of the extinction at low latitudes ($|b| < 5^\circ$). Examining the extinction-corrected NIR colours as a function of the selective $K_s$-band extinction derived from the colour excess $E(B-V)$ (from the DIRBE/IRAS maps[1]), we expect systematic deviation (a linear slope) if the $E(B-V)$ calibration is under or overestimated. If the sample is biased toward a certain Galaxian type at a specific extinction (for example, if the sample at high extinction levels consists of more early type galaxies), a linear trend will appear in the data.

Fig. 3.5 shows a plot of extinction-corrected $3''$ aperture NIR colours against selective $K_s$-band extinction. The linear least squares trend in the bottom frame indicates that galaxies appear bluer at high extinction levels. This suggests that the higher the extinction levels - usually at low Galactic latitude - the DIRBE/IRAS maps provide an overestimate of the extinction. This

[1] See Sect. 1.3 on how selective extinction is derived from colour excess.

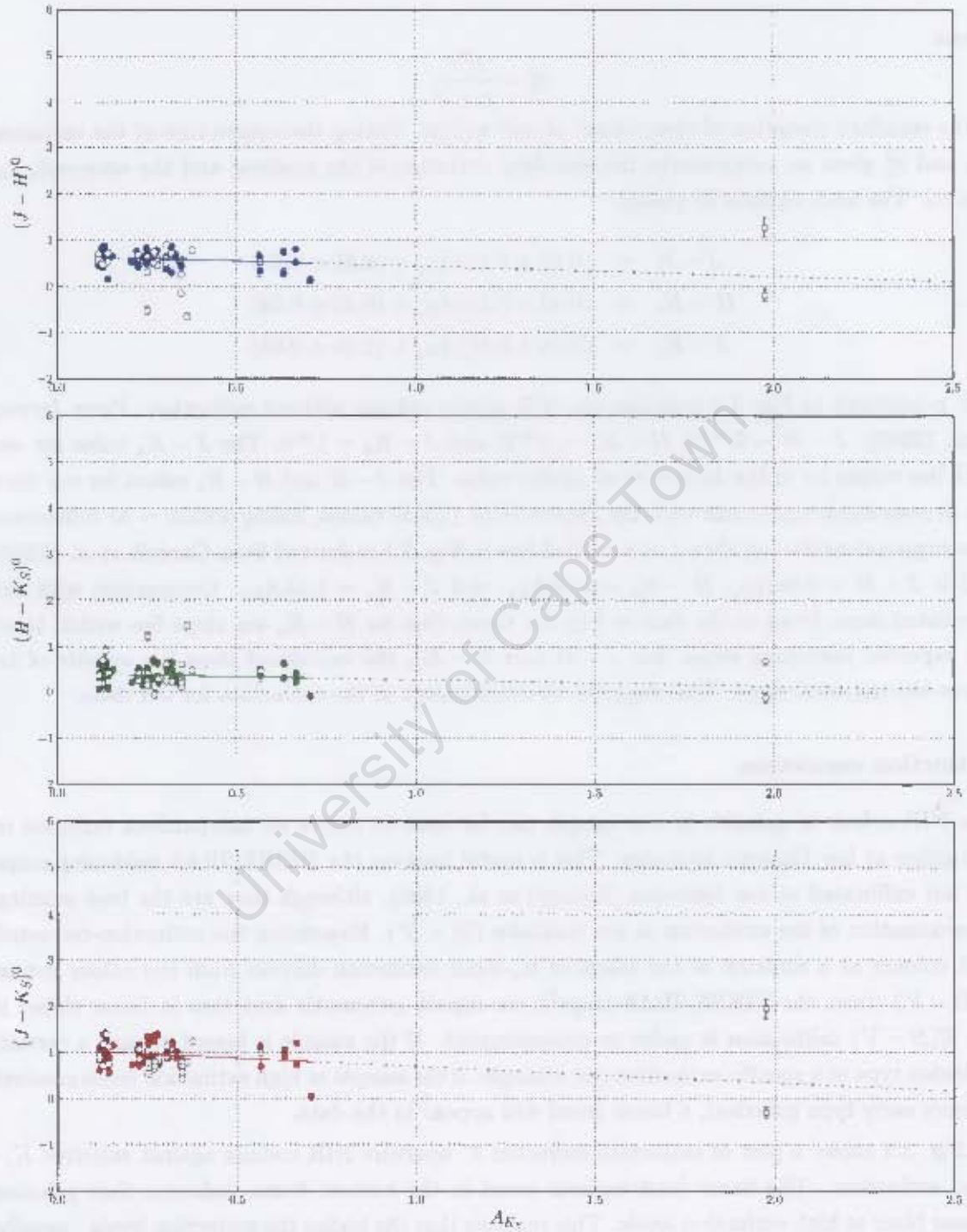




Figure 3.5: Extinction-corrected NIR colours of our sample plotted against selective $K_s$-band extinction derived from the DIRBE/IRAS maps. Galaxies with accurate magnitudes are plotted as filled circles, and inaccurate magnitudes are plotted as open circles. The solid line in each frame is a least squares fit to the galaxies with accurate magnitudes.

result is confirmed by Schröder et al. (2007) who performed a similar analysis in the ZOA, based on NIR ($I$, $J$, and $K_s$) colours (from the DENIS survey) of 83 galaxies lying within a $\sim 30$ square-degree area centred on the radio-bright galaxy PKS 1343-601 located at $(l, b) = (309.°7, +1.°8)$. They found a slope in the extinction-corrected colour of $(J-K_s)^0 = -0.01A_B$, which corresponds to a slope of $(J - K_s)^0 = -0.11A_{K_s}$. This lies within $2\sigma$ of our measured slope (see Eqn. 3.3), implying a more pronounced overestimate of the extinction in our case.

The least squares fitted lines in Fig. 3.5 yield the following values:

$$(J-H)^0 = (-0.22 \pm 0.12)A_{K_s} + (0.66 \pm 0.03) \tag{3.1}$$

$$(H-K)^0 = (-0.13 \pm 0.14)A_{K_s} + (0.40 \pm 0.04) \tag{3.2}$$

$$(J-K)^0 = (-0.35 \pm 0.18)A_{K_s} + (1.05 \pm 0.05) \tag{3.3}$$

The negative gradient in Eqns. 3.1, 3.2 and 3.3 confirm an overestimate of the extinction. To find out the true extinction, a derivation taken directly from Schröder et al. (2007) is performed. We start by saying that for any colour $C^0$, the Eqns. 3.1, 3.2 and 3.3 can be written as

$$C^0 = aA_{K_s} + b \tag{3.4}$$

where the reddening equation is

$$C = C^0 + \left(\frac{E}{A_{K_s}}\right) A_{K_s} \tag{3.5}$$

The true extinction-corrected colour is then

$$\tilde{C}^0 = C - \left(\frac{E}{A_{K_s}}\right) \tilde{A}_{K_s} \tag{3.6}$$

where the tilde ($\sim$) is used to denote any true quantity. Combining these gives

$$\tilde{C}^0 = aA_{K_s} + b + \left(A_{K_s} - \tilde{A}_{K_s}\right)\left(\frac{E}{A_{K_s}}\right) \tag{3.7}$$

We assume that the true extinction $\tilde{A}_{K_s}$ is a constant factor of the DIRBE/IRAS extinction value $A_{K_s}$. This is assumed since we see a linear trend in Fig. 3.5. Thus

$$\tilde{A}_{K_s} = fA_{K_s} \tag{3.8}$$

Eqn. 3.7 then becomes

$$\tilde{C}^0 = \left[a + (1-f)\left(\frac{E}{A_{K_s}}\right)\right] A_{K_s} + b \tag{3.9}$$

Since the extinction-corrected colour should be independent of $\tilde{A}_{K_s}$, the gradient term in square brackets in the last equation must be zero. Thus

$$f = 1 + \frac{a}{(E/A_{K_s})} \tag{3.10}$$

The colour excess $E$ for any colour is $E(\lambda_1 - \lambda_2) = A(\lambda_2)/R$ (see Sect. 1.3). The denominator in Eqn. 3.10 for a colour such as $J - H$ is calculated below:

$$A_J = 2.44 A_{K_s} \quad (3.11)$$

$$A_H = 1.56 A_{K_s} \quad (3.12)$$

$$E(J-H) = (2.44 - 1.56) A_{K_s}$$

$$\therefore \frac{E(J-H)}{A_{K_s}} = 0.88$$

Using the gradient coefficients $a$ from Eqns. 3.1, 3.2 and 3.3, and the method described for calculating the denominator, Eqn. 3.10 gives:

$$f_{J-H} = 0.75 \pm 0.13 \quad (3.13)$$

$$f_{H-K} = 0.76 \pm 0.25 \quad (3.14)$$

$$f_{J-K} = 0.75 \pm 0.13 \quad (3.15)$$

The error in $f$ was propagated from the error in $a$ by a multiplicative factor. To obtain the median $x_{50}$ of the first two estimates of $f$, Sanchis et al. (2004) state that

$$x_{50} = \frac{\Sigma_i x_i/\sigma_i^2}{\Sigma_i \sigma_i^{-2}} \quad (3.16)$$

and the standard deviation is

$$\sigma = \frac{1}{\sqrt{\Sigma_i \sigma_i^{-2}}} \quad (3.17)$$

Using Eqns. 3.16 and 3.17 with the first two independent calculations of $f \pm \sigma_f$, we get a final solution of $f = 0.75 \pm 0.12$. Thus

$$\tilde{A}_{K_s} = (0.75 \pm 0.12) A_{K_s} \quad (3.18)$$

The result is that for our data, the true extinction is 25% lower than is predicted by DIRBE/IRAS values. Using the same method, Schröder et al. (2007) find that $\tilde{A}_B = (0.87 \pm 0.04) A_B$, hence far less of an overestimate of the DIRBE/IRAS values. However, Nagayama et al. (2004) did their own calibration of the DIRBE/IRAS maps in the same area as that of Schröder et al. (2007) using the $J - K_s$ colours of foreground giant stars. They found that $A_{K_s}$ is systematically lower than the DIRBE/IRAS values in this area by $0.^{\mathrm{m}}4$, which corresponds to an $f$-factor of $f \simeq 0.67$ for the average extinction in the area (Schröder et al., 2007). Van Driel et al. (2008) found, in a different region, that the extinction for galaxies with $A_B$ extinctions in the range $6^{\mathrm{m}} < A_B < 12^{\mathrm{m}}$, ($0.^{\mathrm{m}}45 \lesssim A_{K_s} \lesssim 0.^{\mathrm{m}}9$), is about 69% of the quoted Schlegel et al. (1998)

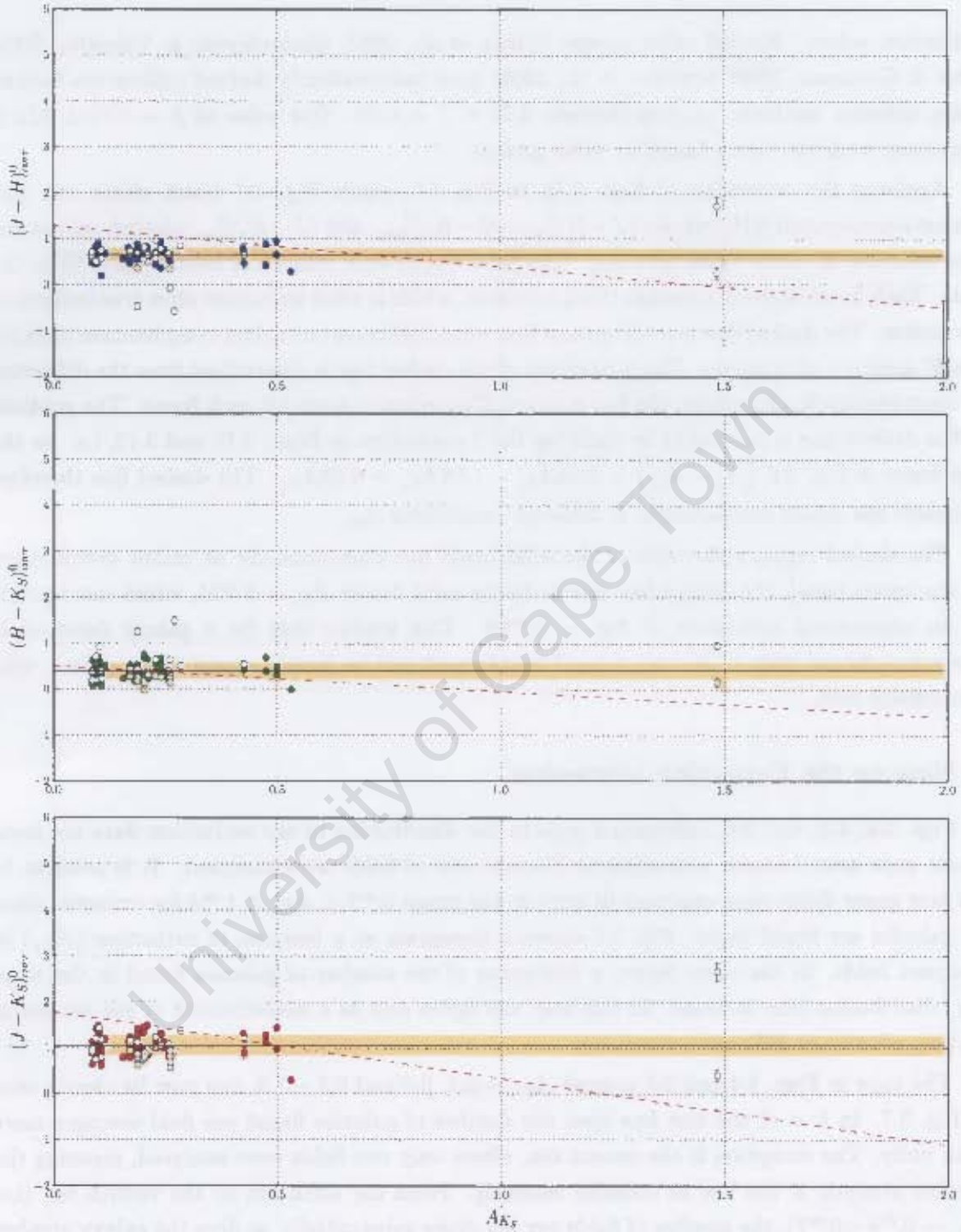


Figure 3.6: True extinction-corrected NIR colours of our sample plotted against true selective $K_s$-band extinction ($\tilde{A}_{K_s}$) derived from the DIRBE/IRAS maps and the modified extinction correction of Eqn. 3.18. The solid lines are a fit to the data, and the dashed lines indicate a colour completeness limit, above which the data is incomplete.

extinction values. Several other groups (Dutra et al., 2003; Choloniewski & Valentijn, 2003; Arce & Goodman, 1999; Schröder et al., 2005) have independently derived calibration factors, using different methods, ranging between $0.67 < f < 0.79$. Our value of $f = 0.75 \pm 0.12$ is consistent with the values found by other groups.

Applying the correction of Eqn. 3.18 to Fig. 3.5, yields Fig. 3.6 which shows the true extinction-corrected NIR colours $(J-H)^0_{corr}$, $(H-K_s)^0_{corr}$, and $(J-K_s)^0_{corr}$ plotted against the true selective $K_s$-band extinction $\tilde{A}_{K_s}$. The solid line in each frame is a least squares fit to the data. Each frame shows a constant trend in colour, which is what we expect after true extinction correction. The dashed line is a theoretical line which indicates our colour completeness limit for the $3''$ aperture photometry. The $y$-intercept of the dashed line is determined from the difference in completeness limit between the two relevant $3''$-aperture colours for each frame. The gradient of the dashed line is calculated by applying the $f$-correction to Eqns. 3.11 and 3.12, i.e. for the top frame in Fig. 3.6 $\left(\tilde{A}_J - \tilde{A}_H\right) = 2.44\tilde{A}_{K_s} - 1.56\tilde{A}_{K_s} = 0.88\tilde{A}_{K_s}$. The dashed line therefore indicates the colour completeness at different extinctions $\tilde{A}_{K_s}$.

The shaded region either side of the solid fitted line represents the $1\sigma$ colour distribution. In the lowest panel, the dashed line intersects the solid line at $\tilde{A}_{K_s} = 0.^{\mathrm{m}}51$, which corresponds to an uncorrected extinction of $A_{K_s} = 0.^{\mathrm{m}}68$. This implies that for a galaxy detected at the completeness limit in $K_s$, no $J$-band counterpart will be found, except if the galaxy were abnormally blue.

### A Note on the Extinction Discussion

In Figs. 3.4, 3.5, and 3.6, substantial gaps in the distribution of the extinction data are seen. These gaps arise because non-adjacent discrete sets of fields were analysed. It is prudent to see how many fields were analysed (if any) in the range $0.^{\mathrm{m}}7 < A_{K_s} < 1.^{\mathrm{m}}4$ for example, since no galaxies are found there. Fig. 3.7 shows a histogram as a function of extinction ($A_{K_s}$) of analysed fields. In the same figure, a histogram of the number of galaxies found in the same $A_{K_s}$ distribution bins is found. In this way, the figure acts as a measurement of the success of finding galaxies at different extinctions.

The gaps in Figs. 3.4 and 3.5 around $A_{K_s} \sim 0.2$, 0.5 and $0.8 - 1.8$, can now be clearly seen in Fig. 3.7. In four of the first five bins, the number of galaxies found per field averages more than unity. The exception is the second bin, where only two fields were analysed, meaning the number statistic is too low to consider seriously. From the sixth bin to the twelfth bin (i.e. $A_{K_s} \sim 0.^{\mathrm{m}}4 - 0.^{\mathrm{m}}7$), the number of fields per bin drops substantially, as does the galaxy number density. This could be a result of a poor number statistic, i.e. the same situation as the second bin. However, if one adds the number of fields observed in these seven bins (24 fields) and

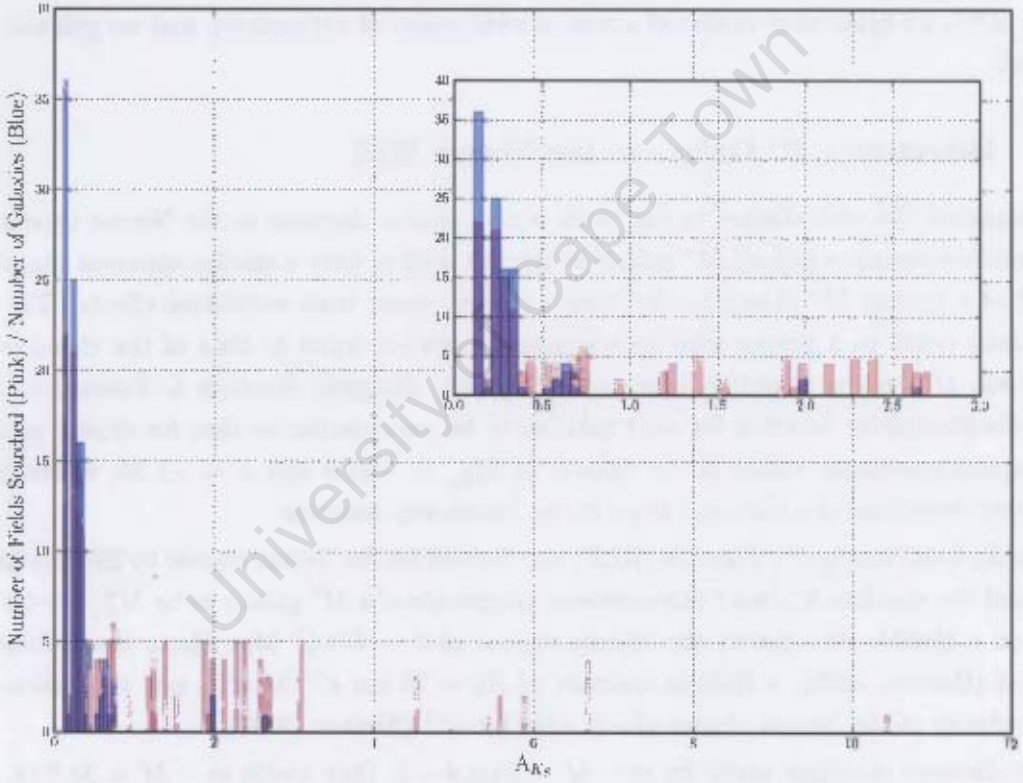




Figure 3.7: Histogram showing the number and distribution, in $A_{K_s}$, of all fields analysed (in light red). Overlaid is the histogram showing the number of galaxies found in the same bins (in light blue). The inset shows a zoomed in portion of the main plot for clarity.

divides by the number of galaxies detected (9 galaxies), the average galaxy number density per field certainly drops well below unity (0.38 galaxies per field). This is confirmation that as the extinction increases, the ability to detect galaxies drops substantially.

In the range $0.^{\rm m}7 < A_{K_s} < 2.^{\rm m}7$, the detection rate drops even further. Similar numbers of fields per bin were analysed in comparison to the range $0.^{\rm m}4 < A_{K_s} < 0.^{\rm m}7$, yet the galaxy number density is far lower. In this range, 53 fields were analysed, with only 3 detections, which means an average galaxy number density per field dropping to 0.06 galaxies per field. Above $A_{K_s} > 2.^{\rm m}7$, 22 fields were observed across a wide range of extinctions, and no galaxies were detected.

### 3.1.5 Detecting a $M^\star$ Galaxy in the Norma Wall

The suspected GA wall studied in this work is at a similar distance to the Norma cluster. We can therefore assume a typical $M^\star$ galaxy in the GA wall to have a similar apparent magnitude to that of a typical $M^\star$ galaxy in the Norma cluster, apart from extinction effects. The term $M^\star$ galaxy refers to a galaxy with an absolute magnitude equal to that of the characteristic magnitude $M^\star$ on the Schechter luminosity function. Binggeli, Sandage & Tammann (1988) found the luminosity function for field galaxies to be very similar to that for cluster galaxies, with typical parameter values in the optical of $M^\star_{B_T} \sim -21.0$ and $\alpha \sim -1.25$, where $\alpha$ is a parameter describing the faint-end slope of the luminosity function.

The $K_s$-band luminosity function (KLF) was derived for the Norma cluster by Skelton (2007). She found the absolute $K_s$-band characteristic magnitude of a $M^\star$ galaxy to be $M^\star_{K_s} = -24.^{\rm m}48$, based on a Hubble distance to the Norma cluster of $d = 67 h_{70}^{-1}$ Mpc (from the Hubble law $v = H_0 d$ (Hubble, 1929), a Hubble constant of $H_0 = 70$ km s$^{-1}$ Mpc$^{-1}$, and the heliocentric radial velocity of the Norma cluster of $v = 4844$ km s$^{-1}$ (Skelton, 2007).)

The distance modulus, given by $m - M = 5 \log d - 5$, then yields $m - M = 34.^{\rm m}14$. The apparent unobscured magnitude of a $M^\star$ galaxy at the distance of the Norma cluster is therefore $m^\star_{K_s} = -24.48 + 34.14 = 9.^{\rm m}66$. With typical NIR galaxy colours of $J - K_s \simeq 1.^{\rm m}0$ and $H - K_s \simeq 0.^{\rm m}27$ (Jarrett et al., 2003), we get $m^\star_H = 9.^{\rm m}93$ and $m^\star_J = 10.^{\rm m}66$. In our case, extinction needs to be taken into account to correct the characteristic apparent magnitude $m^\star$ at different extinction levels. Fig. 3.8 shows the apparent $J$, $H$, and $K_s$ Kron magnitudes of the detected galaxies plotted against true $K_s$-band extinction. The completeness limits for Kron magnitudes are shown as horizontal dashed lines. The solid line intercepts the $y$-axis at $m^\star$. The solid line shows the position in the diagram of an $M^\star$ galaxy in the Norma Wall at different extinction levels.

Where the solid line intersects the horizontal dashed line, we find the limiting true $K_s$-band

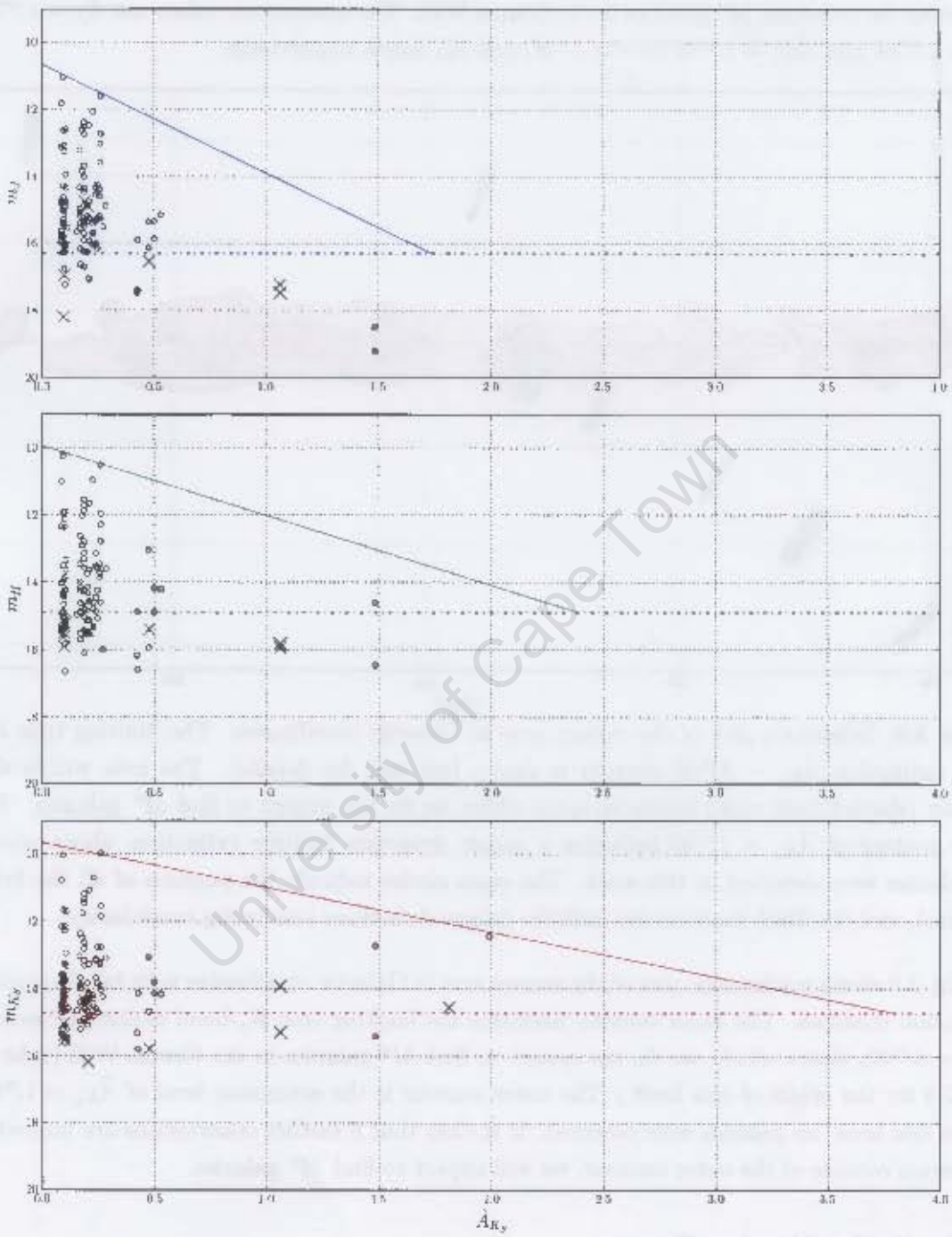




Figure 3.8: Apparent $J$, $H$, and $K_s$ Kron magnitudes plotted against true $K_s$-band extinction. Candidates are plotted as crosses. The horizontal dashed line indicates the completeness limit for Kron magnitudes (see Sect. 3.1.2). The solid line intercepts the $y$-axis at the apparent magnitude $m^*$ as discussed in the text. The intersection of the solid line and the dashed line indicates the limiting true $K_s$-band extinction at which detections of $m^*$ galaxies is still complete.

extinction for detecting $M^*$ galaxies in the Norma Wall. The intersection values are $\bar{A}_J = 1.^{\rm m}74$, $\bar{A}_H = 2.^{\rm m}39$, and $\bar{A}_{K_s} = 3.^{\rm m}80$ for the $J$, $H$, and $K_s$ bands respectively.

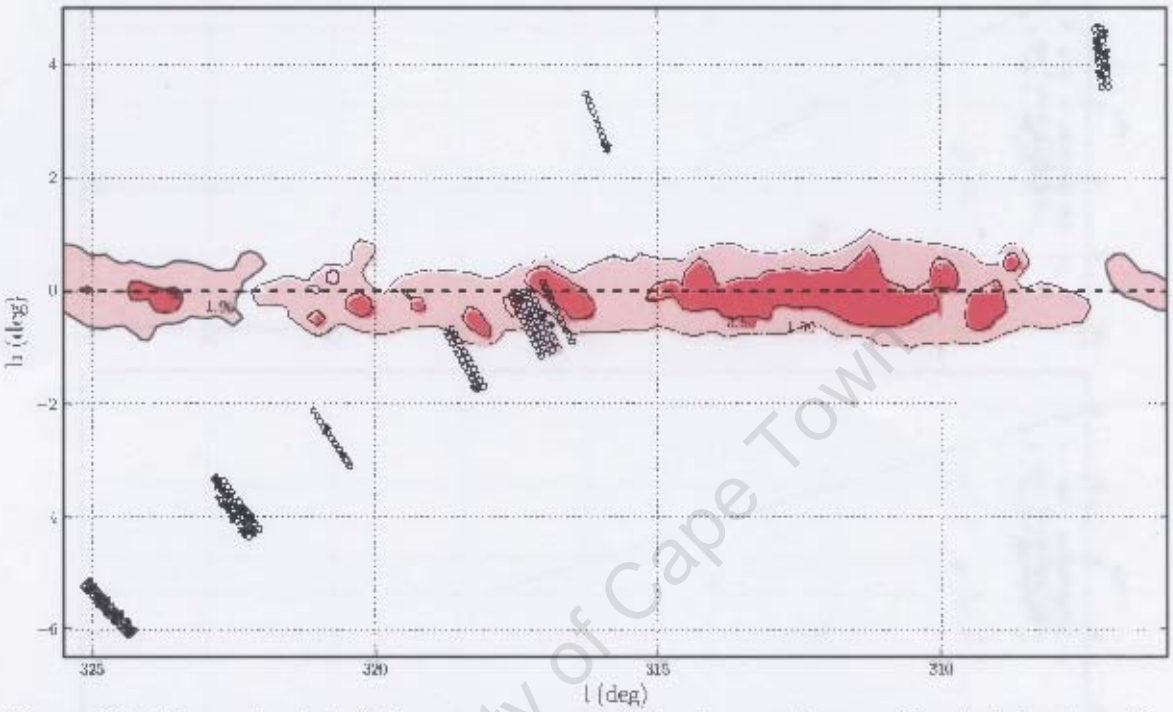


Figure 3.9: Schematic plot of the survey area in Galactic coordinates. The limiting true $K_s$-band extinction $\bar{A}_{K_s} = 3.^{\rm m}80$ contour is shown (see text for details). The area within this contour (shaded dark pink) indicates areas where we do not expect to find $M^*$ galaxies. The outer contour of $\bar{A}_{K_s} = 1.^{\rm m}99$ indicates a galaxy detection limiting extinction, above which, no galaxies were detected in this work. The open circles indicate the position of all the fields searched, and the filled black circles indicate galaxy detections (excluding candidates).

Fig. 3.9 shows a schematic plot of the survey area in Galactic coordinates with two important extinction contours. The inner contour indicates the limiting true $K_s$-band extinction level of $\bar{A}_{K_s} = 3.^{\rm m}80$, above which, we do not expect to find $M^*$ galaxies in the Norma Wall (refer to Fig. 3.8 for the origin of this limit.) The outer contour is the extinction level of $\bar{A}_{K_s} = 1.^{\rm m}99$. Above this level, no galaxies were detected. It is clear that if further observations are limited to the region outside of the outer contour, we will expect to find $M^*$ galaxies.

### 3.1.6 Stellar Number Density

Apart from extinction, the effect of star crowding, which is particularly strong in the NIR, hinders galaxy detection and photometry. Star crowding, or stellar number density, was quantified by

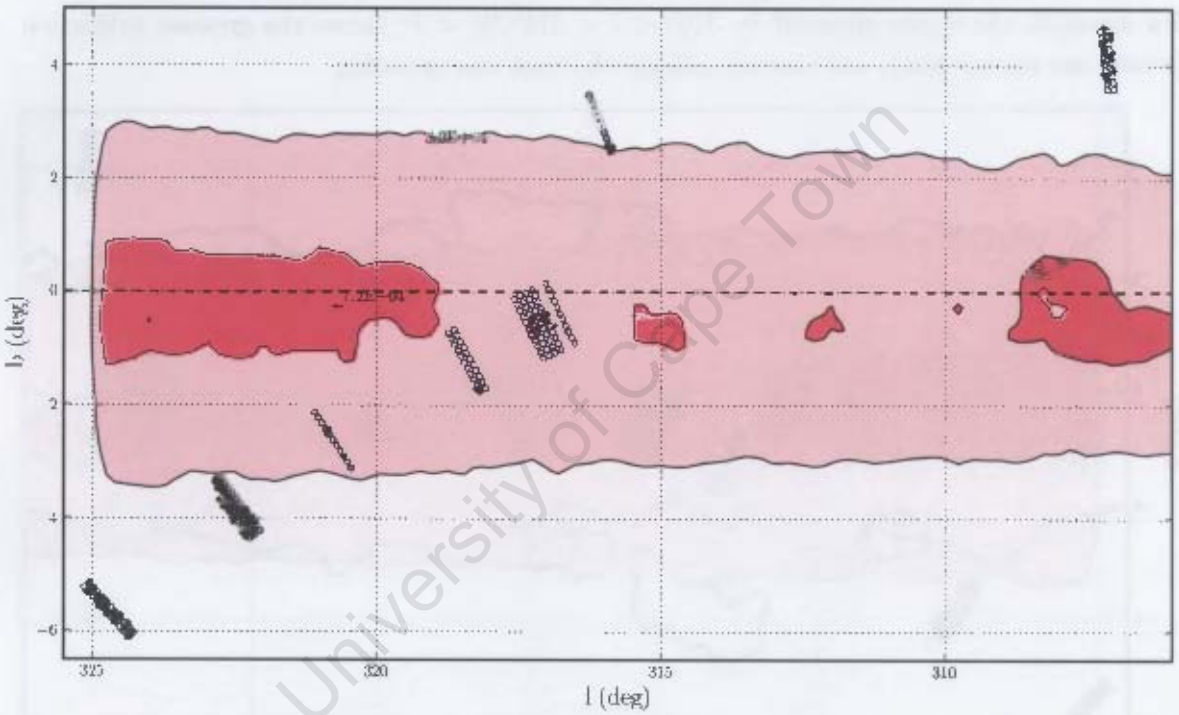




Figure 3.10: Schematic plot of the survey area in Galactic coordinates. The cut-off star number density level above which no galaxies were found in this work, is marked by the inner contour of $7.2 \times 10^4$ /deg$^2$. The area within this contour (shaded dark pink) indicates areas where we do not expect to find galaxies due to extreme star crowding. The outer contour of $3.2 \times 10^4$ /deg$^2$ indicates a star number density level above which 10% of all galaxies in this work were found. The open circles indicate the position of all the fields searched, and the filled black circles indicate galaxy detections (excluding candidates).

measuring the number of stars in the 2MASS Point Source Catalogue (PSC) brighter than $K_s = 14.^m0$ and dividing by the area of the field of interest. In this way, a map of the stellar density was created (see Fig. 2.3). The distribution in Fig. 2.3 shows an increase at low Galactic latitude, in addition to an increase toward the Galactic bulge. There are, however, very obvious gaps in the star density distribution at low latitudes. It appears that, as the interstellar extinction increases, the star density decreases, although this effect is only noticeable at very high extinction levels. For example, the region enclosed by $310° < l < 315°$, $b < 1°$ shows the greatest extinction (within our survey area), and correspondingly the least star crowding.

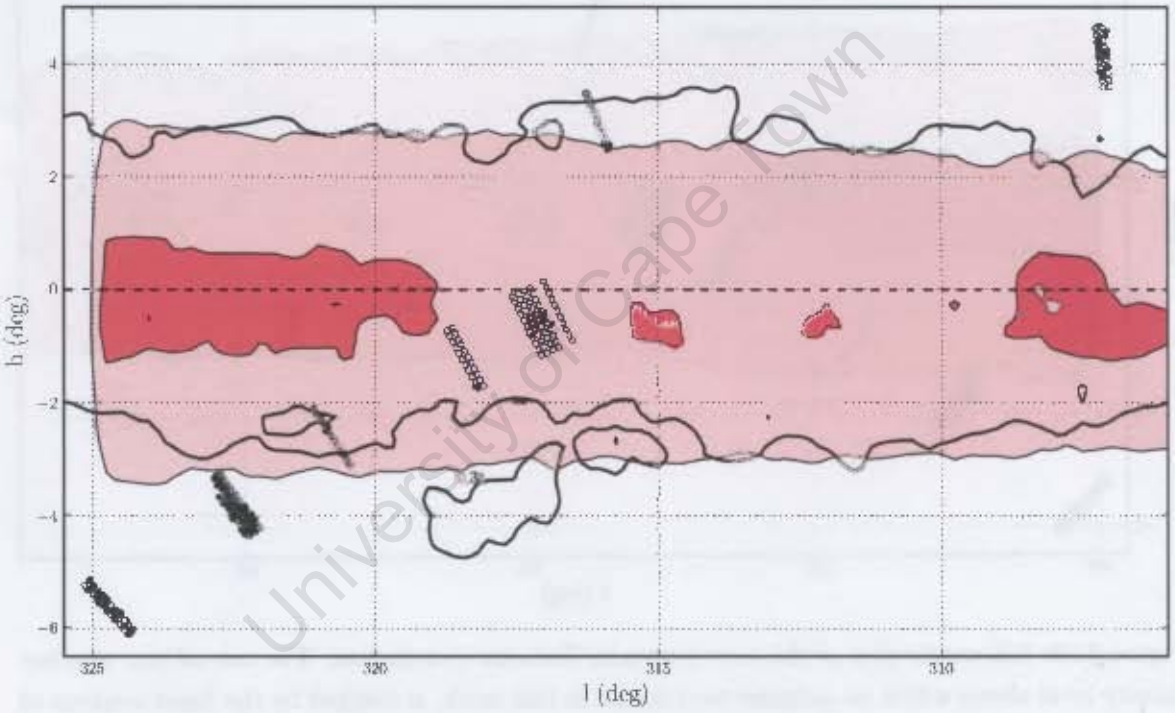




Figure 3.11: Schematic plot of the survey area in Galactic coordinates. The shaded regions are the same as in Fig. 3.10. The thick solid contour (unfilled) indicates the true extinction contour of $\bar{A}_{K_s} = 0.^m37$. The open circles indicate the position of all the fields searched, and the filled black circles indicate galaxy detections (excluding candidates).

A star number density map is shown in Fig. 3.10. The inner dark pink shaded region indicates area where we do not expect to find any galaxies due to extreme stellar confusion. The intermediate region between $3.2 \times 10^4$ /deg$^2$ $\longrightarrow$ $7.2 \times 10^4$ /deg$^2$ shaded light pink has an observed 10% galaxy detection rate, i.e. only 10% of all galaxy detections in this work were found in this region. The remaining 90% of galaxies lie at star number densities $< 3.2 \times 10^4$ /deg$^2$ (the outside region). We can make such a comparison because the number of fields searched in

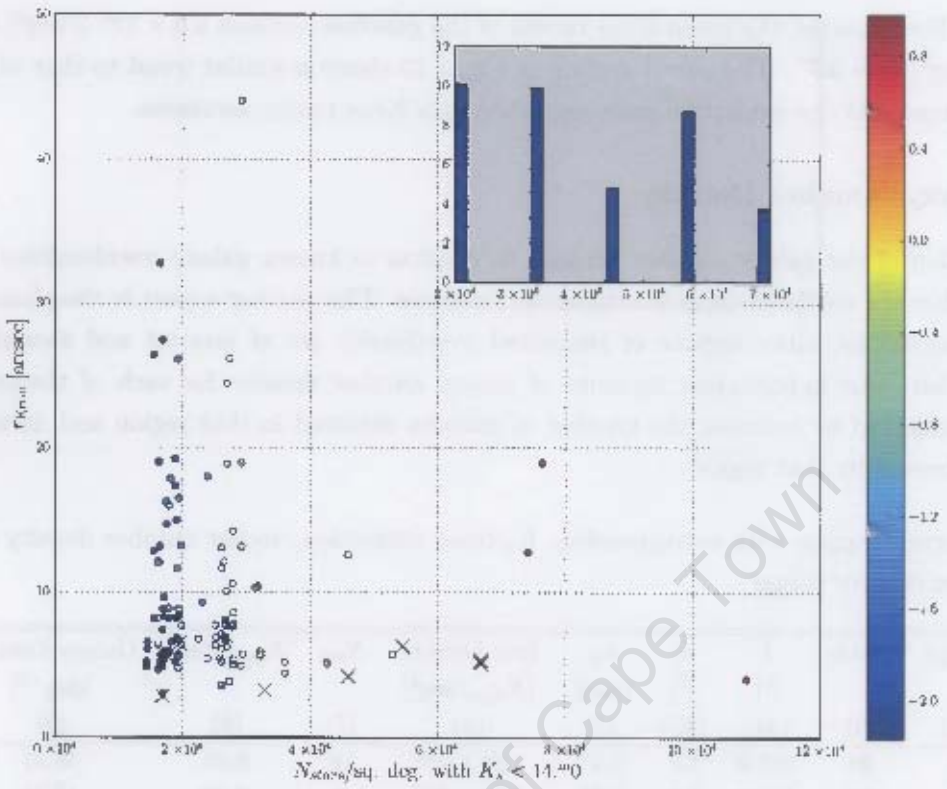

Figure 3.12: Kron radius (in arcseconds) versus star density. The star density is given by the number of stars per square degree brighter than $K_s < 14^m$ in the region immediately surrounding each galaxy. Candidates are shown as crosses. The image is colour coded by $\log_{10}(A_{K_s})$ so as to easily distinguish small differences in the extinction between different galaxies. The inset shows the mean Kron radius of galaxies up to certain star densities (see text for details).



the intermediate region (88 fields) is very similar to the number of fields searched in the outside region (85 fields).

In Fig. 3.11, the same star density contours of Fig. 3.10 are marked. The thick unfilled contour marks the true extinction contour of $A_{K_s} = 0.^m38$, which is equivalent to the uncorrected extinction contour of $A_{K_s} = 0.^m50$. This contour marks the observed 10% galaxy detection rate in terms of extinction. That is, above this contour, only $\sim 10\%$ of galaxy detections in this work were found.

Fig. 3.12 demonstrates the diameter reduction effect as a function of star crowding. Although the data is too sparse at high star density levels (leading to poor number statistics) to fit with a function, it does suggest a decreasing trend in Kron radius as a function of star density. The inset in Fig. 3.12 clarifies the trend by plotting the mean Kron radius of the galaxies in star

Galaxy density of three areas, including two rich clusters and one suspected overdensity, were calculated for comparison. These three areas were also mapped with the IRSF in a similar configuration to this survey. The Norma cluster $(l, b) = (324.3°, -7.2°)$ is a rich cluster, of which the galaxy density of the central 0.53 deg$^2$ area was calculated. In this area, the average extinction is $A_{K_s} = 0.^{\rm m}08$. CIZA J1324.7-5736 (CIZA J1324 hereafter) $(l, b) = (307.4°, 5.0°)$ is a less rich cluster than the Norma cluster, but is possibly the second richest cluster in the GA region (Nagayama et al., 2006). The galaxy density of CIZA J1324 was calculated for the central 0.34 deg$^2$. The average extinction in this area was $A_{K_s} = 0.^{\rm m}27$. The region surrounding PKS 1343-601 (PKS 1343 hereafter) $(l, b) = (309.7°, 1.7°)$ is a suspected overdensity. It is not as rich as the Norma cluster or CIZA J1324, and is more likely a galaxy group, poor cluster, or part of a filamentary structure. The galaxy density was calculated for the central 0.34 deg$^2$. The average extinction in this area was $A_{K_s} = 0.^{\rm m}68$.

Fig. 3.13 compares the measured galaxy density in the seven survey regions with known regions of overdensity: the Norma cluster, the region surrounding PKS 1343, and CIZA J1324. The density is calculated by measuring the number of galaxies with a $K_s$-band magnitude within the survey completeness limit of $K_s^{lim} = 14.^{\rm m}72$ and normalising to a number per square degrees. This limit is applied to all the survey regions and the known overdense regions. Artificial levels of extinction are applied to $K_s$-band magnitudes. If the applied extinction is greater than a galaxy's measured extinction, the difference is applied to the galaxy's $K_s$-band magnitude. If this causes the magnitude to drop beyond the completeness limit, the galaxy is not included in the density measurement at that specific $A_{K_s}$. The data for the Norma cluster was taken from Skelton (2007), CIZA J1324 from Nagayama et al. (2006) and PKS 1343-601 from Nagayama et al. (2004). The measured extinction is taken from the DIRBE/IRAS maps for the Norma cluster and CIZA J1324, since the DIRBE/IRAS values are calibrated at those latitudes. Nagayama et al. (2004) used the $J - K_s$ colour of giant foreground stars to measure the extinction, and found it to be systematically $0.^{\rm m}4$ lower than the DIRBE/IRAS values. We have kept their extinction values, because the DIRBE/IRAS values are not calibrated at the latitude of PKS 1343. For the survey regions, we have used the $f$-corrected DIRBE/IRAS extinction values (discussed in Sect. 3.1.4).

The galaxy densities are compared at $A_{K_s} = 0.^{\rm m}75$, $A_{K_s} = 1.^{\rm m}0$, and $A_{K_s} = 1.^{\rm m}5$, and summarised in Table 3.3.

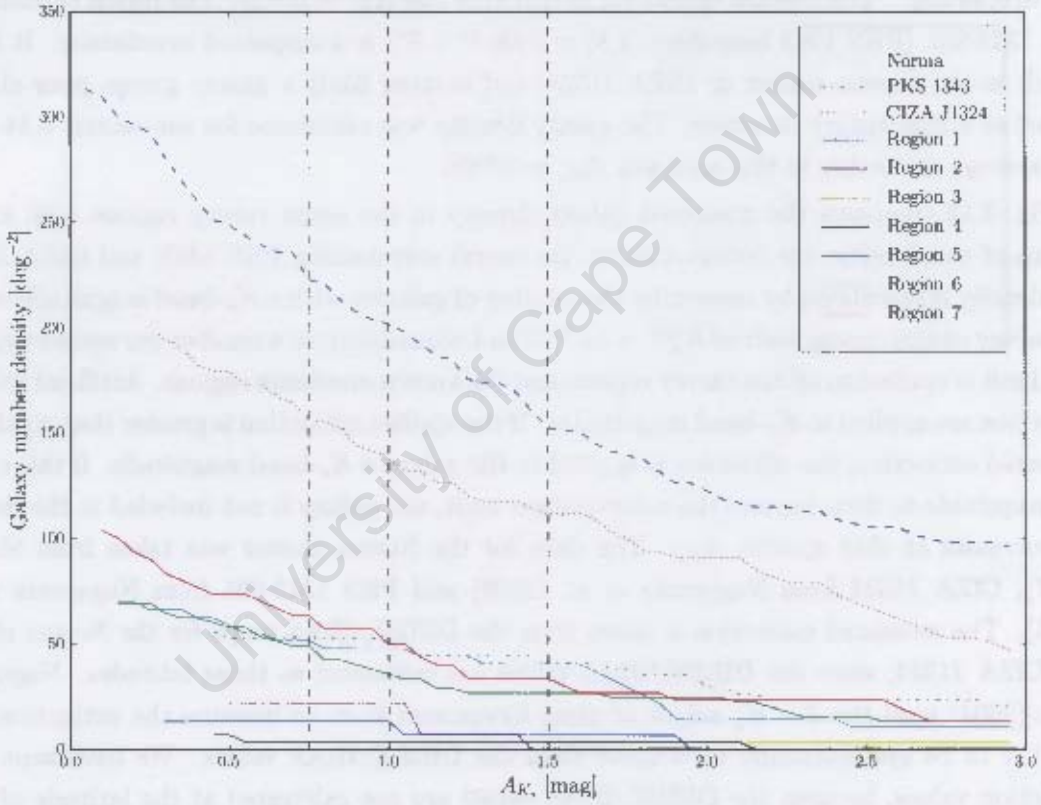




Figure 3.13: Comparison of galaxy number density as a function of applied extinction in the $K_s$ band for the seven survey regions as well as the PKS 1343-601 overdensity, the Norma cluster and CIZA J1324.7.

Table 3.3: Comparison of galaxy number density as a function of applied extinction in the $K_s$ band for the seven survey regions as well as the PKS 1343-601 overdensity, the Norma cluster and CIZA J1324.7

| Region | $\rho(A_{K_s} = 0.^{\rm m}75)$ [deg$^{-2}$] | $\rho(A_{K_s} = 1.^{\rm m}0)$ [deg$^{-2}$] | $\rho(A_{K_s} = 1.^{\rm m}5)$ [deg$^{-2}$] |
|---|---|---|---|
| (1) | (2a) | (2b) | (2c) |
| Norma | 222.6 | 201.9 | 152.8 |
| CIZA J1324.7 | 155.9 | 138.2 | 111.8 |
| PKS 1343-601 | 52.9 | 50.0 | 41.2 |
| Region 1 | 51.4 | 47.8 | 40.4 |
| Region 2 | 22.0 | 22.0 | 0.0 |
| Region 3 | 5.0 | 3.3 | 3.3 |
| Region 4 | 3.3 | 3.3 | 3.3 |
| Region 5 | 13.4 | 13.4 | 6.7 |
| Region 6 | 49.0 | 35.6 | 26.7 |
| Region 7 | 63.5 | 50.1 | 33.4 |

Regions 3 and 4 appear underdense. This is an effect arising due to the very high extinction (these two regions predominantly have $A_{K_s} > 1.^{\rm m}5$) and extreme star crowding. If we take the PKS 1343-601 density of 52.9 galaxies deg$^{-2}$ at $A_{K_s} = 0.^{\rm m}75$ as a mean density for inferring overdensities, we find Regions 2 and 5 fall short of this cut-off. Regions 1, 6 and 7 are consistent with the cut-off, and remain consistent with the galaxy density surrounding PKS 1343-601 at greater extinction levels.

To establish a context for the galaxy number densities listed in Table 3.2, a comparison with existing NIR galaxy number densities is necessary. To calculate the field galaxy number density, the 2MASS XSC was searched throughout the whole sky, with the exception of a band of $|b| \leq 10°$ centred on the Galactic equator for all Galactic longitudes. The total number of galaxies with $K_s$ magnitude brighter than the XSC completeness limit of $K_s^{lim} = 13.^{\rm m}5$ was $N(K_s \leq 13.^{\rm m}5) = 264227$. To calculate the area of the whole sky excluding the central band, the following calculation was done:

$$\begin{aligned} A &= 2\int_0^{2\pi}\int_0^{\frac{80}{180}\pi} \sin\phi \, d\phi \, d\theta \\ &= 4\pi \left[-\cos\phi\right]_0^{\frac{80}{180}\pi} \\ &= 0.826(4\pi) \text{ steradians} \end{aligned}$$

where $4\pi$ steradians is the area of the whole sky ($\sim$ 41253 deg$^2$). The area with $|b| > 10°$ is

therefore $A = 34089$ deg$^2$. The average galaxy density for which $K_s < 13.^{\rm m}5$ is $\rho(K_s \leq 13.^{\rm m}5) = 7.75$ gal/deg$^2$.

Table 3.4 compares the same regions already discussed with the average field density and the average density in the GA region[2]. The data for the field and GA regions is taken from the 2MASS XSC. In both the field and GA regions, the central $|b| \leq 5°$ is not included in the calculation, because of severe incompleteness close to the Galactic Plane. The average densities listed in Table 3.4 were calculated based on galaxies that were brighter than $K_s^{lim} = 13.^{\rm m}5$ after the artificial extinction was applied.

Table 3.4: Comparison of galaxy number density as a function of applied extinction in the $K_s$ band for the seven survey regions, the PKS 1343-601 overdensity, the Norma cluster, CIZA J1324.7, as well as the GA region and the general field. The detection limit is $K_s^{lim} = 13.^{\rm m}5$.

| Region | $\rho(A_{K_s} = 0.^{\rm m}5)$ [deg$^{-2}$] | $\rho(A_{K_s} = 1.^{\rm m}0)$ [deg$^{-2}$] | $\rho(A_{K_s} = 1.^{\rm m}5)$ [deg$^{-2}$] | $\rho(A_{K_s} = 2.^{\rm m}0)$ [deg$^{-2}$] |
|---|---|---|---|---|
| (1) | (2a) | (2b) | (2c) | (2d) |
| Field ($\|b\| > 5°$) | 3.7 | 1.8 | 0.9 | 0.5 |
| GA ($\|b\| > 5°$) | 6.6 | 3.3 | 1.7 | 0.9 |
| Norma | 139.6 | 115.1 | 98.1 | 77.4 |
| CIZA J1324.7 | 102.9 | 82.4 | 55.9 | 41.2 |
| PKS 1343-601 | 38.2 | 23.5 | 23.5 | 14.7 |
| Region 1 | 33.1 | 14.7 | 11.0 | 7.3 |
| Region 2 | 0.0 | 0.0 | 0.0 | 0.0 |
| Region 3 | 3.3 | 3.3 | 3.3 | 3.3 |
| Region 4 | 3.3 | 0.0 | 0.0 | 0.0 |
| Region 5 | 6.7 | 0.0 | 0.0 | 0.0 |
| Region 6 | 24.5 | 17.8 | 13.4 | 11.1 |
| Region 7 | 26.7 | 23.4 | 13.4 | 6.7 |

Table 3.4 indicates that the average GA density at all extinctions is approximately twice that of the average field density. At the completeness limit of $K_s^{lim} = 13.^{\rm m}5$, Regions 1, 6, and 7 are still consistent with the density 'enhancement' (Nagayama et al., 2004) around PKS 1343-601. Regions 2, 3, 4, and 5 have number statistics that are too low for meaningful comparison at this completeness limit.

Fig. 3.14 shows regions 1, 6, and 7 in relation to known overdensities in the GA region. Region 7 has a clear overdensity, which could be due to its close proximity with the Norma

[2]The GA region here follows the definition of $290° < l < 250°$, $-25° < b < 45°$ (Lynden-Bell, Lahav & Burstein, 1989)

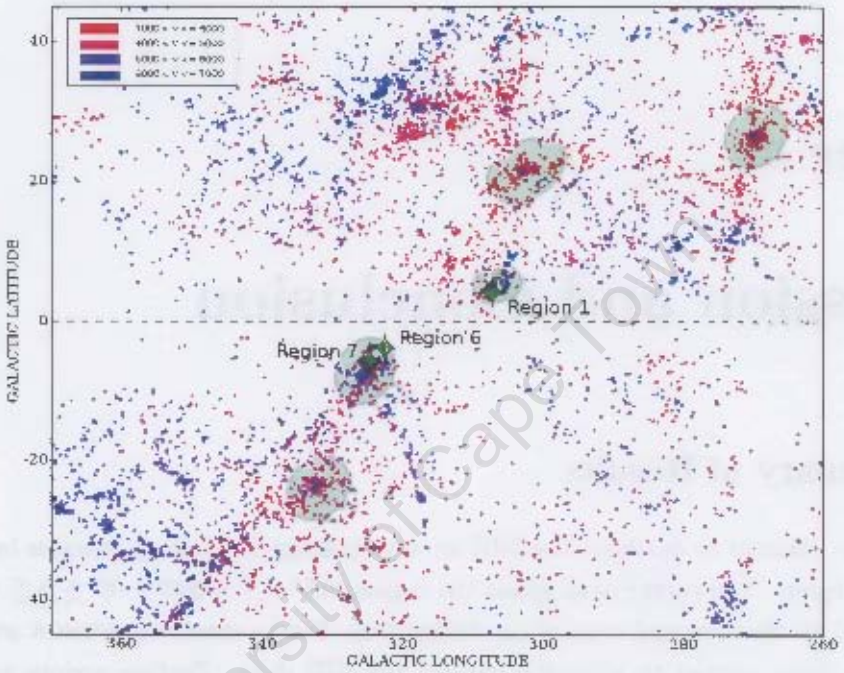


Figure 3.14: Schematic plot showing large-scale structures in the GA region. Galaxies are shown as coloured dots, with colour indicating heliocentric radial velocity. PKS 1343-601 and Regions 1, 6, and 7 are marked. The faint shaded regions highlight known overdensities and can be seen in Fig. 1.2.

cluster, although redshifts were not measured for our data, and hence distances are not known. Region 6 lies on the outskirts of the Norma cluster. Region 1 is most likely an extension of the Cen-Crux cluster and the CIZA J1324 cluster. These three regions show similar densities to the region surrounding PKS 1343-601. It should be noted that a possible filamentary structure extends from Region 1 through PKS 1343 to Region 7. This is suggested based on the alignment of Regions 1, 6, and 7 with PKS 1343 and the similar galaxy densities found in these regions.

# Chapter 4

# Discussion and Conclusion

## 4.1 Summary of Results

This thesis was planned to optimise the NIR survey strategy for finding galaxies in the highly obscured GA region. The survey area spans the region $305° \lesssim l \lesssim 325°, -6° \lesssim b \lesssim 4°$, a region highly obscured by the dust and stars of the Milky Way. Semi-automatic PYTHON scripts, using IRAF packages, were written to efficiently reduce the NIR data. Further scripts were written to utilise IRAF packages such as KILLALL to remove foreground stellar contamination which is substantial at these longitudes and latitudes, as well as blemishes from reduced NIR images. Galaxies were then extracted and photometry performed by writing a fully automatic script to make use of Source Extractor (Bertin & Arnouts, 1996). The photometry of the 106 identified galaxies and 9 candidates found in the 162 examined fields in the survey area, are given in the catalogue (see Appendix A). Extinction estimates derived from the DIRBE/IRAS maps (Schlegel et al., 1998) for each galaxy are also listed, and an estimate of the star number density around each galaxy, based on the 2MASS PSC. The diameter of each galaxy is also listed, based on the Kron radius in the $K_s$-band.

The magnitudes were analysed with respect to each galaxy's Galactic coordinates, and the corresponding foreground interstellar extinction and star number density. An analysis of the NIR galaxy colours revealed an overestimate in the extinction values calculated from the DIRBE/IRAS maps. This overestimate was corrected for when analysing extinction related effects. Certain key results to consider when optimising the survey strategy are listed below:

1. At true $K_s$-band extinction levels greater than $\tilde{A}_{K_s} > 0.^{\mathrm{m}}51$, detections of galaxies with true extinction-corrected $J - K_s$ colours typical of those found in this thesis, will be incomplete.

2. No galaxies were detected in regions where $\tilde{A}_{K_s} > 1.^{\rm m}99$ $(A_{K_s} > 2.^{\rm m}65)$. $M^\star$ galaxies (based on the Norma Cluster $K_s$-band luminosity function (Skelton, 2007)), should have been detected up to a limiting extinction of $\tilde{A}_{K_s} \leq 3.^{\rm m}80$ $(A_{K_s} \leq 5.^{\rm m}06)$. This indicates that our fields do not cover a Norma-like cluster.

3. No galaxies were detected in regions where the star number density exceeds $7.2 \times 10^4$ deg$^{-2}$ in the 2MASS PSC for stars with $K_s < 14^{\rm m}$. Ninety percent of galaxy detections were made in regions where the star number density is less than $3.2 \times 10^4$ deg$^{-2}$. The remaining galaxies were found in regions of higher star density. An equivalent number of fields were searched to find those remaining ten percent.

4. The true $K_s$-band extinction corresponding to the star number density contour of $3.2 \times 10^4$ deg$^{-2}$, seems to correspond and follow closely a matching extinction contour of $\tilde{A}_{K_s} = 0.^{\rm m}38$ $(A_{K_s} = 0.^{\rm m}50)$.

5. Analysis of the region surrounding the radio bright galaxy PKS1343-601 situated at $(l, b) = (309.^\circ7, +1.^\circ8)$ by Nagayama et al. (2004), revealed an apparent 'enhancement' in the galaxy number density with respect to the general galaxy number density in the GA. Using the galaxy density in this area as an indicator of the possibility of a galaxy overdensity, we found three of the seven regions analysed in this thesis to be likely regions of galaxy overdensities. These three regions are situated in environments where the star number density and foreground interstellar extinction are below the limits set out in the points above. Furthermore, these regions in alignment with PKS 1343-601, could form part of a filamentary of wall-like structure which extends from Region 1, through PKS 1343-601 to Region 7. The other four regions lie above the limits discussed.

These key results are useful in optimising future observations for the overall survey. The proposed extinction and star number density limits are based on what we have found in a relatively small number of fields. More data would allow for better constraints to the proposed survey strategy, but would require more time to analyse.

### 4.1.1 A Proposed Survey Strategy

We have seen that it is primarily star crowding and extinction that determine the apparent galaxy distribution in the survey area, rather than the true underlying galaxy distribution. To maximise the number of galaxy detections for this survey, future observations should be limited to regions where star crowding and extinction do not significantly delimit our perception of the underlying galaxy distribution.

Currently, the three regions that were found to be likely overdensities adhere to environments that lie below the thresholds for star crowding and extinction as set out in Sect. 4.1. This correlation implies that if future observations are limited to similar environments, and continue along an extension of these three regions, they will be more successful in unveiling galaxies than observations in environments lying above the set out thresholds. In particular, the following observation plan should be considered:

1. Completion of observations along the Upper Northern Branch (see Sect. 2.1.1) as well as an extension of that branch toward Region 2
2. Extension of the Lower Northern Branch block toward $l = 305°$
3. Completion of observations along the Southern Branch running from Region 6 to Region 5
4. Possible addition of a lower Southern Branch adjacent to the existing branch, running from $(l, b) \sim (320°, -5°) \longrightarrow (317°, -3°)$

These planned observations, together with analysis of existing survey data should yield a more efficient means for revealing many galaxies which trace the inherent underlying large-scale structure. Application of the reduction and analysis scripts and routines that were written for this thesis will facilitate efficient treatment of survey data.

# Appendix A

# Catalogue of Galaxies in the Survey Area

A catalogue of galaxies and galaxy candidates identified in this thesis is presented in Table A.1. Galaxies labelled with a * symbol have uncertain magnitudes. Galaxies labelled with a † symbol are listed in the 2MASS Extended Source Catalogue. The catalogue contains 115 objects divided into 106 galaxies and 9 candidates. The catalogue has the following columns:

**Column 1:** Identification number. This matches the numbering scheme on the stamp image catalogue presented in Appendix C
**Column 2:** Right Ascension (RA) and Declination (Dec) (J2000)
**Column 3:** Galactic longitude ($l$) and latitude ($b$)
**Column 4:** Interstellar extinction in the $K_s$-band ($A_{K_s}$) as determined from the Schlegel et al. (1998) Galactic reddening maps (see Sect. 3.1.4)
**Column 5:** Stellar number density measured in number of stars with $K_s < 14^{\mathrm{m}}$ per square degree as found in the 2MASS PSC (see Sect. 3.1.6)
**Column 6:** Galaxy (O) or Candidate (X) classification based on visual inspection of FITS images, SE star/galaxy classification and $J - K_s$ colour.
**Column 7:** Kron $J$-band magnitude and error. Not corrected for extinction.
**Column 8:** Kron $H$-band magnitude and error. Not corrected for extinction.
**Column 9:** Kron $K_s$-band magnitude and error. Not corrected for extinction.
**Column 10:** Central 3″-radius aperture $J$-band magnitude and error. Not corrected for extinction.
**Column 11:** Central 3″-radius aperture $H$-band magnitude and error. Not corrected for extinction.

**Column 12:** Central $3''$-radius aperture $K_s$-band magnitude and error. Not corrected for extinction.

**Column 13:** Diameter ($D$) of the object in arcseconds in the $K_s$-band. This is determined from the relation $D = 2\times$ `KRON_RADIUS`$\times$`A`, where `A` represents the maximum spatial rms of the object profile in any direction, and `KRON_RADIUS` represents a numerical factor describing the extent of the semi-major axis of the Kron aperture.

Table A.1: Catalogue of galaxies and galaxy candidates with NIR photometry

| Ident. | RA | Dec | $l$ | $b$ | $A_{K_s}$ | S.D. | Class | $J_{Kron}$ | $H_{Kron}$ | $K_{s_{Kron}}$ | $J_{Ap}$ | $H_{Ap}$ | $K_{s_{Ap}}$ | $D_{K_s}^{Kron}$ |
|---|---|---|---|---|---|---|---|---|---|---|---|---|---|---|
| | [hms] | [° ′ ″] | [°] | [°] | [mag] | [$10^4$deg$^{-2}$] | | [mag] | [mag] | [mag] | [mag] | [mag] | [mag] | [″] |
| (1) | (2a) | (2b) | (3a) | (3b) | (4) | (5) | (6) | (7) | (8) | (9) | (10) | (11) | (12) | (13) |
| 1 | 14 31 13.0 | -57 44 36.5 | 315.95 | 2.58 | 0.66 | 3.23 | O | 15.34 ± 0.04 | 14.18 ± 0.04 | 13.81 ± 0.05 | 15.74 ± 0.04 | 14.64 ± 0.04 | 14.04 ± 0.05 | 11.8 |
| 2 | 14 30 34.3 | -57 47 48.7 | 315.85 | 2.57 | 0.70 | 3.23 | O | 15.15 ± 0.05 | 14.20 ± 0.04 | 14.16 ± 0.06 | 15.51 ± 0.04 | 14.75 ± 0.04 | 14.43 ± 0.05 | 11.3 |
| 3 | 14 31 12.5 | -57 52 16.7 | 315.90 | 2.47 | 0.66 | 3.18 | O | 15.86 ± 0.05 | 14.88 ± 0.05 | 14.14 ± 0.06 | 16.85 ± 0.05 | 15.47 ± 0.05 | 14.68 ± 0.06 | 20.8 |
| 4* | 14 48 35.8 | -60 07 02.8 | 317.04 | -0.49 | 1.97 | 7.64 | O | 19.21 ± 0.16 | 14.61 ± 0.05 | 12.72 ± 0.05 | 19.02 ± 0.20 | 16.00 ± 0.05 | 14.21 ± 0.05 | 37.9 |
| 5* | 14 47 50.1 | -60 02 42.9 | 316.99 | -0.39 | 1.97 | 10.84 | O | 18.49 ± 0.12 | 16.47 ± 0.06 | 15.41 ± 0.08 | 18.24 ± 0.11 | 16.68 ± 0.06 | 15.69 ± 0.08 | 08.1 |
| 6* | 14 47 45.0 | -60 17 02.1 | 316.87 | -0.60 | 2.65 | 7.41 | O | ... | ... | 12.44 ± 0.05 | ... | ... | 13.96 ± 0.05 | 25.6 |
| 7 | 14 50 12.0 | -60 01 23.0 | 317.26 | -0.50 | 2.41 | 5.45 | X | ... | ... | 14.53 ± 0.07 | ... | ... | 15.05 ± 0.06 | 12.6 |
| 8 | 15 01 26.0 | -60 12 17.0 | 318.42 | -1.30 | 1.41 | 6.67 | X | 17.48 ± 0.06 | 15.81 ± 0.06 | 15.29 ± 0.07 | 17.46 ± 0.07 | 16.08 ± 0.05 | 15.47 ± 0.07 | 10.3 |
| 9 | 15 01 53.2 | -60 12 34.4 | 318.47 | -1.33 | 1.41 | 6.67 | X | 17.22 ± 0.09 | 15.93 ± 0.07 | 13.92 ± 0.06 | 17.26 ± 0.09 | 15.96 ± 0.06 | 14.29 ± 0.06 | 10.7 |
| 10 | 15 01 50.9 | -60 38 01.3 | 318.26 | -1.70 | 0.63 | 5.29 | O | 16.14 ± 0.06 | 15.94 ± 0.06 | 14.68 ± 0.07 | 16.81 ± 0.06 | 15.97 ± 0.05 | 14.99 ± 0.06 | 11.4 |
| 11 | 15 01 15.4 | -60 42 36.9 | 318.16 | -1.74 | 0.63 | 4.59 | X | 16.52 ± 0.07 | 15.39 ± 0.05 | 15.77 ± 0.10 | 16.75 ± 0.06 | 15.53 ± 0.05 | 15.73 ± 0.09 | 08.5 |
| 12 | 15 01 14.6 | -60 42 10.2 | 318.16 | -1.73 | 0.63 | 4.59 | O | 15.35 ± 0.06 | 13.05 ± 0.04 | 13.07 ± 0.06 | 16.14 ± 0.05 | 14.83 ± 0.04 | 14.17 ± 0.05 | 25.2 |
| 13 | 15 23 22.8 | -59 57 58.5 | 320.89 | -2.50 | 0.56 | 4.27 | O | 17.46 ± 0.07 | 16.17 ± 0.06 | 15.32 ± 0.08 | 17.46 ± 0.06 | 16.31 ± 0.05 | 15.53 ± 0.07 | 10.3 |
| 14* | 15 22 43.9 | -59 54 47.4 | 320.85 | -2.41 | 0.57 | 3.61 | O | 15.90 ± 0.05 | 14.88 ± 0.04 | 14.13 ± 0.05 | 16.08 ± 0.05 | 15.04 ± 0.04 | 14.25 ± 0.05 | 10.5 |
| 15 | 15 22 38.0 | -59 55 17.7 | 320.84 | -2.41 | 0.57 | 3.61 | O | 17.40 ± 0.10 | 16.61 ± 0.07 | 15.80 ± 0.09 | 17.45 ± 0.09 | 16.60 ± 0.08 | 15.93 ± 0.10 | 08.8 |
| 16* | 15 22 52.9 | -60 28 38.4 | 320.56 | -2.90 | 0.38 | 3.14 | O | 14.88 ± 0.04 | 13.60 ± 0.04 | 13.09 ± 0.05 | 15.66 ± 0.04 | 14.54 ± 0.04 | 13.87 ± 0.05 | 20.6 |
| 17 | 15 23 11.3 | -60 44 06.2 | 320.45 | -3.13 | 0.27 | 3.30 | X | 14.88 ± 0.05 | 15.45 ± 0.05 | 16.15 ± 0.09 | 17.07 ± 0.05 | 16.56 ± 0.06 | 16.04 ± 0.08 | 06.6 |
| 18 | 15 39 14.2 | -59 36 32.5 | 322.73 | -3.35 | 0.33 | 2.80 | O | 16.15 ± 0.05 | 15.08 ± 0.05 | 14.71 ± 0.06 | 16.37 ± 0.04 | 15.40 ± 0.04 | 14.88 ± 0.06 | 10.0 |
| 19 | 15 38 43.1 | -60 16 09.7 | 322.29 | -3.84 | 0.28 | 2.54 | O | 17.05 ± 0.06 | 15.54 ± 0.05 | 14.82 ± 0.07 | 17.14 ± 0.05 | 16.13 ± 0.05 | 15.35 ± 0.06 | 13.8 |
| 20 | 15 39 08.6 | -60 25 42.3 | 322.23 | -4.00 | 0.25 | 2.68 | O | 15.34 ± 0.05 | 14.28 ± 0.04 | 14.34 ± 0.06 | 16.65 ± 0.05 | 15.82 ± 0.04 | 15.28 ± 0.06 | 15.8 |
| 21 | 15 39 07.5 | -60 24 49.4 | 322.24 | -3.99 | 0.25 | 2.68 | X | 14.72 ± 0.04 | 14.67 ± 0.04 | 14.35 ± 0.06 | 15.92 ± 0.04 | 15.24 ± 0.04 | 14.72 ± 0.05 | 14.0 |
| 22* | 15 39 06.2 | -60 25 40.2 | 322.23 | -4.00 | 0.25 | 2.68 | O | 15.91 ± 0.05 | 16.11 ± 0.06 | 14.98 ± 0.07 | 16.34 ± 0.04 | 16.65 ± 0.06 | 15.28 ± 0.06 | 13.4 |
| 23 | 15 38 51.3 | -60 26 06.6 | 322.20 | -3.99 | 0.25 | 2.68 | O | 15.47 ± 0.04 | 14.83 ± 0.04 | 14.30 ± 0.06 | 15.89 ± 0.04 | 15.09 ± 0.04 | 14.62 ± 0.05 | 16.2 |
| 24 | 15 38 46.5 | -60 25 51.1 | 322.20 | -3.98 | 0.25 | 2.68 | O | 14.01 ± 0.04 | 13.12 ± 0.04 | 12.81 ± 0.05 | 14.44 ± 0.04 | 13.58 ± 0.04 | 13.13 ± 0.05 | 13.8 |
| 25 | 15 38 55.0 | -60 31 08.7 | 322.16 | -4.06 | 0.25 | 2.40 | O | 16.69 ± 0.05 | 15.45 ± 0.05 | 14.88 ± 0.06 | 16.75 ± 0.05 | 15.80 ± 0.04 | 15.18 ± 0.06 | 10.9 |
| 26* | 15 38 41.7 | -60 26 25.3 | 322.18 | -3.98 | 0.25 | 2.40 | O | 13.68 ± 0.04 | 12.79 ± 0.04 | 12.62 ± 0.05 | 15.19 ± 0.04 | 14.65 ± 0.04 | 14.28 ± 0.05 | 36.0 |
| 27* | 15 39 38.2 | -60 08 45.9 | 322.45 | -3.81 | 0.30 | 2.79 | O | 15.42 ± 0.04 | 14.79 ± 0.04 | 14.29 ± 0.06 | 16.24 ± 0.04 | 15.37 ± 0.04 | 14.89 ± 0.05 | 21.2 |
| 28* | 15 40 01.6 | -60 03 39.6 | 322.54 | -3.77 | 0.30 | 2.95 | O | 16.04 ± 0.05 | 15.35 ± 0.04 | 14.51 ± 0.06 | 16.46 ± 0.04 | 15.68 ± 0.04 | 14.90 ± 0.05 | 11.5 |
| 29 | 15 39 46.3 | -59 55 16.5 | 322.60 | -3.64 | 0.30 | 2.93 | O | 15.71 ± 0.04 | 15.31 ± 0.04 | 14.82 ± 0.06 | 16.26 ± 0.04 | 15.61 ± 0.04 | 14.92 ± 0.05 | 09.9 |
| 30* | 15 39 39.3 | -59 53 47.1 | 322.60 | -3.61 | 0.36 | 2.93 | O | 15.49 ± 0.04 | 16.00 ± 0.05 | 14.24 ± 0.06 | 16.38 ± 0.04 | 16.71 ± 0.06 | 15.06 ± 0.06 | 26.3 |

**Table A.1** continued...

| Ident. | RA | Dec | $l$ | $b$ | $A_{K_s}$ | S.D. | Class | $J_{Kron}$ | $H_{Kron}$ | $K_{s_{Kron}}$ | $J_{Ap}$ | $H_{Ap}$ | $K_{s_{Ap}}$ | $D_{K_s}^{Kron}$ |
|---|---|---|---|---|---|---|---|---|---|---|---|---|---|---|
| | [hms] | [° ′ ″] | [°] | [°] | [mag] | [$10^4$deg$^{-2}$] | | [mag] | [mag] | [mag] | [mag] | [mag] | [mag] | [″] |
| (1) | (2a) | (2b) | (3a) | (3b) | (4) | (5) | (6) | (7) | (8) | (9) | (10) | (11) | (12) | (13) |
| 31* | 15 40 00.6 | -59 44 41.2 | 322.73 | -3.52 | 0.35 | 2.93 | O | 11.60 ± 0.04 | 10.51 ± 0.04 | 9.97 ± 0.05 | 12.63 ± 0.04 | 12.48 ± 0.04 | 11.68 ± 0.05 | 88.1 |
| 32* | 15 39 44.5 | -59 45 59.0 | 322.69 | -3.52 | 0.35 | 2.93 | O | 13.03 ± 0.04 | 12.28 ± 0.04 | 11.85 ± 0.05 | 14.17 ± 0.04 | 13.28 ± 0.04 | 12.87 ± 0.05 | 37.8 |
| 33* | 15 40 16.6 | -59 39 06.4 | 322.81 | -3.46 | 0.35 | 2.70 | O | 12.71 ± 0.04 | 11.95 ± 0.04 | 11.53 ± 0.05 | 13.10 ± 0.04 | 12.53 ± 0.04 | 12.02 ± 0.05 | 20.1 |
| 34 | 15 39 56.5 | -59 41 08.4 | 322.76 | -3.47 | 0.35 | 2.70 | O | 15.26 ± 0.04 | 14.59 ± 0.04 | 14.03 ± 0.06 | 15.84 ± 0.04 | 15.10 ± 0.04 | 14.67 ± 0.05 | 15.6 |
| 35* | 15 39 45.9 | -59 40 02.1 | 322.75 | -3.44 | 0.35 | 2.70 | O | 13.57 ± 0.04 | 12.76 ± 0.04 | 12.76 ± 0.05 | 15.51 ± 0.04 | 14.61 ± 0.04 | 14.31 ± 0.05 | 37.8 |
| 36 | 15 40 00.4 | -59 32 18.8 | 322.85 | -3.35 | 0.33 | 2.80 | O | 15.26 ± 0.04 | 14.24 ± 0.04 | 13.84 ± 0.05 | 15.54 ± 0.04 | 14.56 ± 0.04 | 14.13 ± 0.05 | 15.3 |
| 37 | 15 39 31.0 | -59 30 09.1 | 322.83 | -3.29 | 0.33 | 2.80 | O | 14.25 ± 0.04 | 13.57 ± 0.04 | 12.77 ± 0.05 | 15.60 ± 0.04 | 14.68 ± 0.04 | 14.23 ± 0.05 | 28.4 |
| 38 | 15 39 42.0 | -60 16 33.7 | 322.38 | -3.92 | 0.27 | 2.81 | O | 16.24 ± 0.05 | 15.15 ± 0.04 | 14.37 ± 0.06 | 16.38 ± 0.04 | 15.43 ± 0.04 | 14.62 ± 0.05 | 10.7 |
| 39 | 15 39 35.8 | -60 13 51.5 | 322.40 | -3.88 | 0.27 | 2.81 | O | 16.27 ± 0.05 | 15.54 ± 0.05 | 14.65 ± 0.06 | 16.57 ± 0.04 | 15.81 ± 0.04 | 14.94 ± 0.05 | 15.6 |
| 40* | 15 39 23.2 | -60 14 05.2 | 322.37 | -3.87 | 0.28 | 2.81 | O | 14.74 ± 0.04 | 13.62 ± 0.04 | 13.26 ± 0.05 | 15.24 ± 0.04 | 14.54 ± 0.04 | 14.04 ± 0.05 | 17.2 |
| 41* | 15 39 26.0 | -60 20 52.8 | 322.31 | -3.96 | 0.25 | 2.66 | O | 12.74 ± 0.04 | 11.85 ± 0.04 | 11.18 ± 0.05 | 13.41 ± 0.04 | 12.56 ± 0.04 | 12.00 ± 0.05 | 24.2 |
| 42* | 15 40 02.5 | -60 26 23.3 | 322.32 | -4.08 | 0.25 | 2.68 | O | 15.36 ± 0.04 | 14.80 ± 0.04 | 14.60 ± 0.06 | 16.19 ± 0.04 | 15.33 ± 0.04 | 15.04 ± 0.06 | 15.4 |
| 43 | 15 39 37.6 | -60 37 35.9 | 322.16 | -4.20 | 0.23 | 2.32 | O | 15.06 ± 0.04 | 13.98 ± 0.04 | 13.67 ± 0.05 | 15.59 ± 0.04 | 14.94 ± 0.04 | 14.35 ± 0.05 | 18.6 |
| 44 | 15 40 11.4 | -60 40 46.1 | 322.19 | -4.28 | 0.23 | 2.26 | O | 15.53 ± 0.04 | 14.62 ± 0.04 | 14.00 ± 0.05 | 15.91 ± 0.04 | 15.05 ± 0.04 | 14.41 ± 0.05 | 13.6 |
| 45*† | 15 40 44.8 | -60 05 21.4 | 322.60 | -3.85 | 0.30 | 2.71 | O | 12.06 ± 0.04 | 10.95 ± 0.04 | 10.69 ± 0.05 | 13.96 ± 0.04 | 12.80 ± 0.04 | 12.39 ± 0.05 | 48.9 |
| 46 | 15 40 37.9 | -60 07 29.5 | 322.56 | -3.87 | 0.30 | 2.71 | O | 15.68 ± 0.04 | 14.61 ± 0.04 | 14.20 ± 0.05 | 15.83 ± 0.04 | 14.93 ± 0.04 | 14.42 ± 0.05 | 12.5 |
| 47*† | 15 41 11.8 | -59 58 47.5 | 322.71 | -3.80 | 0.28 | 2.75 | O | 12.48 ± 0.04 | 11.64 ± 0.04 | 11.06 ± 0.05 | 14.31 ± 0.04 | 13.47 ± 0.04 | 13.03 ± 0.05 | 52.4 |
| 48 | 15 41 00.0 | -60 00 11.3 | 322.67 | -3.80 | 0.28 | 2.75 | O | 15.92 ± 0.04 | 15.14 ± 0.04 | 14.80 ± 0.06 | 16.00 ± 0.04 | 15.20 ± 0.04 | 14.84 ± 0.06 | 07.7 |
| 49 | 15 40 59.7 | -59 50 30.4 | 322.77 | -3.67 | 0.28 | 2.60 | O | 15.24 ± 0.04 | 14.57 ± 0.04 | 14.16 ± 0.05 | 15.47 ± 0.04 | 14.67 ± 0.04 | 14.29 ± 0.05 | 10.9 |
| 50* | 15 41 19.4 | -60 17 36.0 | 322.53 | -4.06 | 0.27 | 2.52 | O | 14.87 ± 0.04 | 13.75 ± 0.04 | 13.82 ± 0.06 | 15.54 ± 0.04 | 14.81 ± 0.04 | 14.50 ± 0.05 | 15.5 |
| 51 | 15 40 44.3 | -60 15 41.5 | 322.49 | -3.99 | 0.27 | 2.52 | O | 16.24 ± 0.05 | 15.48 ± 0.05 | 15.08 ± 0.06 | 16.51 ± 0.04 | 15.68 ± 0.04 | 15.24 ± 0.06 | 12.7 |
| 52* | 15 41 14.8 | -60 38 33.6 | 322.31 | -4.33 | 0.23 | 2.62 | O | 13.22 ± 0.04 | 12.61 ± 0.04 | 12.37 ± 0.05 | 14.08 ± 0.04 | 13.26 ± 0.04 | 12.88 ± 0.05 | 23.3 |
| 53 | 15 41 10.8 | -60 33 27.5 | 322.36 | -4.26 | 0.23 | 2.62 | O | 15.17 ± 0.04 | 14.89 ± 0.04 | 14.40 ± 0.06 | 15.92 ± 0.04 | 15.29 ± 0.04 | 14.86 ± 0.05 | 12.3 |
| 54 | 15 41 10.3 | -60 37 36.1 | 322.32 | -4.31 | 0.23 | 2.62 | O | 16.16 ± 0.04 | 15.52 ± 0.04 | 14.98 ± 0.06 | 16.30 ± 0.04 | 15.59 ± 0.04 | 15.06 ± 0.06 | 10.4 |
| 55 | 15 41 03.5 | -60 33 15.4 | 322.35 | -4.25 | 0.23 | 2.62 | O | 15.40 ± 0.05 | 14.16 ± 0.04 | 13.91 ± 0.06 | 16.54 ± 0.04 | 15.74 ± 0.04 | 15.36 ± 0.06 | 26.1 |
| 56* | 15 41 01.6 | -60 37 07.3 | 322.31 | -4.29 | 0.23 | 2.62 | O | 14.97 ± 0.04 | 14.23 ± 0.04 | 13.87 ± 0.05 | 15.63 ± 0.04 | 14.77 ± 0.04 | 14.27 ± 0.05 | 14.2 |
| 57* | 15 40 37.4 | -60 38 30.1 | 322.25 | -4.28 | 0.23 | 2.62 | O | 16.62 ± 0.04 | 15.71 ± 0.04 | 15.21 ± 0.06 | 16.64 ± 0.04 | 15.76 ± 0.04 | 15.23 ± 0.06 | 07.2 |
| 58 | 16 02 48.2 | -60 02 22.7 | 324.77 | -5.55 | 0.13 | 1.45 | O | 15.99 ± 0.05 | 15.24 ± 0.04 | 14.49 ± 0.06 | 16.23 ± 0.04 | 15.47 ± 0.04 | 14.77 ± 0.05 | 12.2 |
| 59 | 16 02 07.2 | -59 58 48.1 | 324.74 | -5.45 | 0.13 | 1.45 | O | 14.92 ± 0.04 | 14.24 ± 0.04 | 13.75 ± 0.05 | 15.28 ± 0.04 | 14.55 ± 0.04 | 14.07 ± 0.05 | 13.1 |
| 60 | 16 02 40.3 | -59 53 13.2 | 324.86 | -5.43 | 0.13 | 1.64 | O | 14.75 ± 0.04 | 13.87 ± 0.04 | 13.26 ± 0.05 | 15.71 ± 0.04 | 14.88 ± 0.04 | 14.19 ± 0.05 | 26.4 |
| 61 | 16 02 35.9 | -59 48 14.2 | 324.91 | -5.36 | 0.14 | 1.73 | O | 14.76 ± 0.04 | 14.22 ± 0.04 | 14.05 ± 0.05 | 15.05 ± 0.04 | 14.76 ± 0.04 | 14.27 ± 0.05 | 11.9 |
| 62 | 16 02 32.9 | -59 39 35.6 | 325.00 | -5.25 | 0.14 | 1.65 | O | 13.95 ± 0.04 | 13.33 ± 0.04 | 12.94 ± 0.05 | 15.85 ± 0.04 | 15.14 ± 0.04 | 14.74 ± 0.05 | 65.5 |
| 63 | 16 02 12.6 | -59 31 07.0 | 325.06 | -5.11 | 0.15 | 1.82 | O | 15.53 ± 0.04 | 15.04 ± 0.04 | 14.57 ± 0.06 | 16.36 ± 0.04 | 15.56 ± 0.04 | 14.98 ± 0.05 | 13.1 |
| 64*† | 16 02 45.3 | -60 17 27.7 | 324.60 | -5.74 | 0.11 | 1.66 | O | 14.74 ± 0.04 | 14.03 ± 0.04 | 13.60 ± 0.05 | 14.91 ± 0.04 | 14.24 ± 0.04 | 13.80 ± 0.05 | 10.3 |
| 65 | 16 02 39.0 | -60 14 58.8 | 324.61 | -5.70 | 0.11 | 1.66 | O | 14.81 ± 0.04 | 14.01 ± 0.04 | 13.82 ± 0.05 | 15.04 ± 0.04 | 14.24 ± 0.04 | 14.01 ± 0.05 | 11.3 |

**Table A.1** continued...

| Ident. | RA | Dec | $l$ | $b$ | $A_{K_s}$ | S.D. | Class | $J_{Kron}$ | $H_{Kron}$ | $K_{s_{Kron}}$ | $J_{Ap}$ | $H_{Ap}$ | $K_{s_{Ap}}$ | $D_{K_s}^{Kron}$ |
|---|---|---|---|---|---|---|---|---|---|---|---|---|---|---|
| | [hms] | [° ′ ″] | [°] | [°] | [mag] | [$10^4$deg$^{-2}$] | | [mag] | [mag] | [mag] | [mag] | [mag] | [mag] | [″] |
| (1) | (2a) | (2b) | (3a) | (3b) | (4) | (5) | (6) | (7) | (8) | (9) | (10) | (11) | (12) | (13) |
| 66*† | 16 02 27.5 | -60 19 41.0 | 324.54 | -5.74 | 0.11 | 1.91 | O | 13.12 ± 0.04 | 12.34 ± 0.04 | 12.16 ± 0.05 | 14.20 ± 0.04 | 13.45 ± 0.04 | 13.17 ± 0.05 | 30.0 |
| 67* | 16 02 26.1 | -60 20 34.5 | 324.53 | -5.75 | 0.11 | 1.91 | O | 15.95 ± 0.04 | 15.25 ± 0.04 | 14.69 ± 0.06 | 16.21 ± 0.04 | 15.50 ± 0.04 | 15.06 ± 0.05 | 16.3 |
| 68 | 16 02 13.0 | -60 21 12.5 | 324.50 | -5.74 | 0.11 | 1.91 | O | 15.63 ± 0.04 | 14.92 ± 0.04 | 14.42 ± 0.05 | 15.76 ± 0.04 | 15.21 ± 0.04 | 14.75 ± 0.05 | 13.7 |
| 69 | 16 01 56.6 | -60 20 10.2 | 324.49 | -5.70 | 0.11 | 1.91 | O | 15.73 ± 0.04 | 15.41 ± 0.05 | 14.52 ± 0.06 | 16.20 ± 0.04 | 15.61 ± 0.04 | 14.92 ± 0.05 | 13.6 |
| 70 | 16 01 55.2 | -60 31 25.4 | 324.36 | -5.84 | 0.12 | 1.93 | O | 15.81 ± 0.04 | 15.05 ± 0.04 | 14.36 ± 0.05 | 15.89 ± 0.04 | 15.18 ± 0.04 | 14.62 ± 0.05 | 11.5 |
| 71† | 16 02 33.7 | -60 33 23.8 | 324.40 | -5.92 | 0.13 | 1.75 | O | 12.64 ± 0.04 | 11.93 ± 0.04 | 11.66 ± 0.05 | 13.49 ± 0.04 | 12.75 ± 0.04 | 12.44 ± 0.05 | 29.4 |
| 72 | 16 02 29.9 | -60 40 29.3 | 324.32 | -6.00 | 0.13 | 1.95 | O | 15.43 ± 0.04 | 14.39 ± 0.04 | 13.82 ± 0.05 | 16.02 ± 0.04 | 15.16 ± 0.04 | 14.45 ± 0.05 | 16.7 |
| 73 | 16 02 19.3 | -60 39 43.9 | 324.31 | -5.98 | 0.13 | 1.95 | X | 16.13 ± 0.05 | 15.51 ± 0.05 | 15.01 ± 0.06 | 16.49 ± 0.04 | 16.27 ± 0.05 | 15.30 ± 0.06 | 13.0 |
| 74† | 16 03 34.8 | -60 08 55.6 | 324.77 | -5.70 | 0.12 | 1.63 | O | 11.04 ± 0.04 | 10.23 ± 0.04 | 10.04 ± 0.05 | 12.38 ± 0.04 | 11.61 ± 0.04 | 11.34 ± 0.05 | 38.1 |
| 75 | 16 03 24.0 | -60 07 37.3 | 324.77 | -5.67 | 0.12 | 1.63 | O | 15.76 ± 0.04 | 14.88 ± 0.04 | 14.60 ± 0.06 | 16.08 ± 0.04 | 15.25 ± 0.04 | 14.83 ± 0.05 | 09.4 |
| 76 | 16 03 34.4 | -59 57 26.2 | 324.89 | -5.55 | 0.13 | 1.43 | O | 16.76 ± 0.05 | 15.84 ± 0.06 | 15.08 ± 0.07 | 16.85 ± 0.05 | 16.09 ± 0.05 | 15.34 ± 0.07 | 10.4 |
| 77* | 16 03 17.8 | -60 02 46.5 | 324.81 | -5.60 | 0.13 | 1.43 | O | 17.22 ± 0.06 | 16.64 ± 0.06 | 15.60 ± 0.07 | 17.30 ± 0.05 | 16.70 ± 0.06 | 15.71 ± 0.07 | 10.3 |
| 78 | 16 02 48.1 | -60 02 22.8 | 324.77 | -5.55 | 0.13 | 1.43 | O | 16.07 ± 0.05 | 15.18 ± 0.05 | 14.67 ± 0.06 | 16.14 ± 0.05 | 15.45 ± 0.04 | 14.86 ± 0.06 | 09.7 |
| 79 | 16 03 21.1 | -59 52 55.9 | 324.92 | -5.48 | 0.13 | 1.88 | O | 13.09 ± 0.04 | 12.12 ± 0.04 | 12.27 ± 0.05 | 15.35 ± 0.04 | 14.60 ± 0.04 | 14.14 ± 0.05 | 38.5 |
| 80 | 16 03 18.1 | -59 56 20.6 | 324.88 | -5.52 | 0.13 | 1.88 | O | 16.27 ± 0.04 | 15.05 ± 0.04 | 14.66 ± 0.06 | 16.44 ± 0.04 | 15.46 ± 0.04 | 14.83 ± 0.06 | 10.5 |
| 81† | 16 03 09.2 | -59 51 46.9 | 324.92 | -5.45 | 0.13 | 1.88 | O | 13.26 ± 0.04 | 12.35 ± 0.04 | 12.13 ± 0.05 | 14.24 ± 0.04 | 13.48 ± 0.04 | 13.21 ± 0.05 | 34.7 |
| 82 | 16 03 04.4 | -59 50 18.8 | 324.93 | -5.42 | 0.13 | 1.69 | O | 15.13 ± 0.04 | 14.44 ± 0.04 | 14.23 ± 0.06 | 15.99 ± 0.04 | 15.21 ± 0.04 | 14.97 ± 0.06 | 17.7 |
| 83* | 16 03 32.8 | -59 37 41.7 | 325.11 | -5.31 | 0.14 | 1.55 | O | 14.34 ± 0.04 | 13.63 ± 0.04 | 13.32 ± 0.05 | 15.27 ± 0.04 | 14.42 ± 0.04 | 13.93 ± 0.05 | 25.7 |
| 84*† | 16 03 29.3 | -59 39 47.4 | 325.08 | -5.33 | 0.14 | 1.55 | O | 12.58 ± 0.04 | 11.90 ± 0.04 | 11.70 ± 0.05 | 13.96 ± 0.04 | 13.29 ± 0.04 | 12.99 ± 0.05 | 52.9 |
| 85 | 16 03 10.3 | -59 37 41.1 | 325.08 | -5.27 | 0.14 | 1.55 | O | 16.19 ± 0.05 | 15.26 ± 0.05 | 15.48 ± 0.08 | 16.90 ± 0.05 | 16.11 ± 0.05 | 15.95 ± 0.08 | 16.4 |
| 86 | 16 02 59.0 | -60 15 15.1 | 324.64 | -5.73 | 0.12 | 1.68 | X | 18.17 ± 0.10 | 15.62 ± 0.06 | 15.40 ± 0.06 | 17.97 ± 0.09 | 16.66 ± 0.06 | 15.41 ± 0.06 | 05.8 |
| 87* | 16 02 56.7 | -60 13 11.7 | 324.66 | -5.70 | 0.12 | 1.68 | O | 15.01 ± 0.04 | 14.32 ± 0.04 | 14.04 ± 0.05 | 15.15 ± 0.04 | 14.52 ± 0.04 | 14.26 ± 0.05 | 14.8 |
| 88 | 16 03 28.7 | -60 19 41.3 | 324.64 | -5.82 | 0.12 | 1.69 | O | 16.28 ± 0.05 | 15.35 ± 0.04 | 15.19 ± 0.06 | 16.36 ± 0.05 | 15.42 ± 0.04 | 15.22 ± 0.07 | 06.1 |
| 89 | 16 03 25.3 | -60 21 36.4 | 324.61 | -5.84 | 0.11 | 1.69 | O | 15.79 ± 0.05 | 15.28 ± 0.05 | 15.36 ± 0.08 | 16.29 ± 0.04 | 15.64 ± 0.05 | 15.50 ± 0.07 | 09.8 |
| 90* | 16 03 15.3 | -60 21 26.1 | 324.60 | -5.83 | 0.11 | 1.69 | O | 11.82 ± 0.04 | 10.99 ± 0.04 | 10.76 ± 0.05 | 13.35 ± 0.04 | 12.54 ± 0.04 | 12.28 ± 0.05 | 54.9 |
| 91 | 16 03 00.9 | -60 33 09.7 | 324.45 | -5.95 | 0.13 | 1.79 | O | 15.40 ± 0.04 | 14.65 ± 0.04 | 14.16 ± 0.06 | 16.12 ± 0.04 | 15.40 ± 0.04 | 14.86 ± 0.06 | 16.4 |
| 92 | 16 03 32.0 | -60 42 28.1 | 324.39 | -6.11 | 0.13 | 1.71 | O | 14.62 ± 0.04 | 13.92 ± 0.04 | 13.58 ± 0.05 | 14.80 ± 0.04 | 14.17 ± 0.04 | 13.78 ± 0.05 | 11.6 |
| 93 | 16 03 25.6 | -60 42 41.2 | 324.38 | -6.10 | 0.13 | 1.71 | X | 16.95 ± 0.05 | 15.90 ± 0.05 | 15.52 ± 0.09 | 17.05 ± 0.05 | 16.30 ± 0.05 | 15.77 ± 0.08 | 11.7 |
| 94 | 16 03 20.5 | -60 43 36.9 | 324.36 | -6.11 | 0.13 | 1.71 | O | 15.01 ± 0.04 | 14.32 ± 0.04 | 13.68 ± 0.05 | 15.29 ± 0.04 | 14.75 ± 0.04 | 14.12 ± 0.05 | 19.3 |
| 95 | 16 03 10.2 | -60 44 29.8 | 324.33 | -6.11 | 0.13 | 1.71 | O | 14.28 ± 0.04 | 13.51 ± 0.04 | 13.73 ± 0.05 | 15.00 ± 0.04 | 14.26 ± 0.04 | 13.97 ± 0.05 | 10.7 |
| 96* | 16 03 05.8 | -60 41 25.3 | 324.36 | -6.06 | 0.13 | 1.71 | O | 15.31 ± 0.05 | 14.34 ± 0.04 | 14.21 ± 0.06 | 16.21 ± 0.04 | 15.62 ± 0.04 | 14.85 ± 0.06 | 16.6 |
| 97* | 13 23 38.9 | -57 55 29.1 | 307.21 | 4.68 | 0.27 | 1.94 | O | 15.35 ± 0.04 | 14.32 ± 0.04 | 14.31 ± 0.05 | 15.77 ± 0.04 | 14.83 ± 0.04 | 14.57 ± 0.05 | 09.6 |
| 98* | 13 22 54.1 | -58 02 25.5 | 307.10 | 4.58 | 0.34 | 1.94 | O | 14.59 ± 0.04 | 13.73 ± 0.04 | 13.29 ± 0.05 | 14.91 ± 0.04 | 14.02 ± 0.04 | 13.46 ± 0.05 | 11.2 |
| 99 | 13 22 40.1 | -58 02 20.1 | 307.07 | 4.58 | 0.34 | 1.94 | O | 15.19 ± 0.05 | 13.85 ± 0.04 | 13.91 ± 0.06 | 15.86 ± 0.04 | 15.01 ± 0.04 | 14.66 ± 0.06 | 17.6 |
| 100† | 13 23 38.8 | -58 07 49.3 | 307.19 | 4.48 | 0.25 | 1.98 | O | 12.38 ± 0.04 | 11.53 ± 0.04 | 11.45 ± 0.05 | 13.31 ± 0.04 | 12.48 ± 0.04 | 12.12 ± 0.05 | 26.4 |

**Table A.1** continued...

| Ident. | RA | Dec | $l$ | $b$ | $A_{K_s}$ | S.D. | Class | $J_{Kron}$ | $H_{Kron}$ | $K_{s_{Kron}}$ | $J_{Ap}$ | $H_{Ap}$ | $K_{s_{Ap}}$ | $D_{K_s}^{Kron}$ |
|---|---|---|---|---|---|---|---|---|---|---|---|---|---|---|
| | [hms] | [° ′ ″] | [°] | [°] | [mag] | [$10^4$deg$^{-2}$] | | [mag] | [mag] | [mag] | [mag] | [mag] | [mag] | [″] |
| (1) | (2a) | (2b) | (3a) | (3b) | (4) | (5) | (6) | (7) | (8) | (9) | (10) | (11) | (12) | (13) |
| 101† | 13 22 47.8 | -58 07 22.0 | 307.08 | 4.50 | 0.34 | 1.98 | O | 14.38 ± 0.04 | 13.46 ± 0.04 | 13.20 ± 0.05 | 14.71 ± 0.04 | 13.84 ± 0.04 | 13.47 ± 0.05 | 12.8 |
| 102 | 13 22 46.7 | -58 22 38.5 | 307.04 | 4.24 | 0.32 | 1.92 | O | 16.01 ± 0.05 | 14.88 ± 0.04 | 14.59 ± 0.06 | 16.57 ± 0.04 | 15.57 ± 0.04 | 14.90 ± 0.05 | 13.5 |
| 103*† | 13 23 10.6 | -58 25 23.5 | 307.09 | 4.19 | 0.32 | 1.78 | O | 14.33 ± 0.04 | 13.14 ± 0.04 | 13.16 ± 0.05 | 15.19 ± 0.04 | 14.19 ± 0.04 | 13.78 ± 0.05 | 17.8 |
| 104 | 13 23 09.0 | -58 25 57.1 | 307.08 | 4.18 | 0.32 | 1.78 | O | 14.55 ± 0.04 | 13.53 ± 0.04 | 13.11 ± 0.05 | 15.67 ± 0.04 | 14.52 ± 0.04 | 14.02 ± 0.05 | 32.0 |
| 105 | 13 23 05.9 | -58 28 57.4 | 307.07 | 4.13 | 0.32 | 1.78 | O | 15.34 ± 0.04 | 14.44 ± 0.04 | 13.67 ± 0.05 | 15.45 ± 0.04 | 14.87 ± 0.04 | 14.04 ± 0.05 | 11.7 |
| 106 | 13 22 55.4 | -58 40 38.6 | 307.02 | 3.94 | 0.22 | 1.74 | O | 14.34 ± 0.04 | 13.46 ± 0.04 | 13.03 ± 0.05 | 15.32 ± 0.04 | 14.36 ± 0.04 | 13.93 ± 0.05 | 32.6 |
| 107* | 13 23 39.5 | -57 55 05.8 | 307.21 | 4.69 | 0.27 | 1.99 | O | 15.18 ± 0.04 | 14.14 ± 0.04 | 14.13 ± 0.06 | 15.79 ± 0.04 | 14.80 ± 0.04 | 14.70 ± 0.05 | 15.3 |
| 108 | 13 23 39.8 | -58 07 25.1 | 307.19 | 4.48 | 0.25 | 1.94 | O | 12.50 ± 0.04 | 11.71 ± 0.04 | 11.34 ± 0.05 | 13.48 ± 0.04 | 12.61 ± 0.04 | 12.22 ± 0.05 | 33.0 |
| 109 | 13 24 04.1 | -58 12 27.9 | 307.23 | 4.39 | 0.25 | 1.91 | O | 16.24 ± 0.04 | 15.04 ± 0.04 | 14.43 ± 0.06 | 16.74 ± 0.04 | 15.69 ± 0.04 | 15.04 ± 0.05 | 23.3 |
| 110 | 13 23 54.2 | -58 18 15.2 | 307.20 | 4.30 | 0.24 | 1.81 | O | 13.84 ± 0.04 | 12.90 ± 0.04 | 12.49 ± 0.05 | 15.07 ± 0.04 | 14.23 ± 0.04 | 13.93 ± 0.05 | 35.7 |
| 111† | 13 23 48.0 | -58 24 05.7 | 307.17 | 4.20 | 0.24 | 1.92 | O | 12.60 ± 0.04 | 12.02 ± 0.04 | 11.76 ± 0.05 | 14.29 ± 0.04 | 13.43 ± 0.04 | 13.06 ± 0.05 | 52.3 |
| 112 | 13 24 17.1 | -58 30 09.8 | 307.22 | 4.10 | 0.21 | 1.78 | O | 15.64 ± 0.04 | 14.98 ± 0.04 | 14.66 ± 0.06 | 15.90 ± 0.04 | 15.20 ± 0.04 | 14.87 ± 0.05 | 11.9 |
| 113 | 13 24 27.4 | -58 44 08.9 | 307.21 | 3.86 | 0.25 | 1.61 | O | 14.35 ± 0.04 | 13.30 ± 0.04 | 13.30 ± 0.05 | 15.89 ± 0.04 | 15.17 ± 0.04 | 14.53 ± 0.05 | 24.1 |
| 114 | 13 24 02.4 | -58 50 04.8 | 307.15 | 3.77 | 0.25 | 1.61 | O | 15.70 ± 0.04 | 14.79 ± 0.04 | 14.38 ± 0.05 | 16.07 ± 0.04 | 15.18 ± 0.04 | 14.71 ± 0.05 | 16.4 |
| 115 | 13 23 57.6 | -58 45 23.7 | 307.15 | 3.85 | 0.25 | 1.61 | O | 14.45 ± 0.04 | 13.57 ± 0.04 | 13.16 ± 0.05 | 14.81 ± 0.04 | 13.95 ± 0.04 | 13.51 ± 0.05 | 12.8 |

# Appendix B

# Fields Searched

Table B.1: Complete list of fields, with associated colour excess and number of galaxies

| Region | RA | Dec | $l$ | $b$ | $E(B-V)$ | $N_{detections}$ |
|---|---|---|---|---|---|---|
| | [hms] | [° ′ ″] | [°] | [°] | [mag] | |
| (1) | (2a) | (2b) | (3a) | (3b) | (4) | (5) |
| 1 | 13 23 11 | -59 01 41 | 307.02 | +3.59 | 1.15 | - |
| 1 | 13 23 11 | -58 54 41 | 307.03 | +3.71 | 0.83 | - |
| 1 | 13 23 11 | -58 47 41 | 307.04 | +3.82 | 0.83 | - |
| 1 | 13 23 11 | -58 40 41 | 307.06 | +3.94 | 0.60 | 1 |
| 1 | 13 23 11 | -58 33 41 | 307.07 | +4.05 | 0.60 | - |
| 1 | 13 23 11 | -58 26 41 | 307.09 | +4.17 | 0.87 | 3 |
| 1 | 13 23 11 | -58 19 41 | 307.10 | +4.29 | 0.87 | 1 |
| 1 | 13 23 11 | -58 12 41 | 307.12 | +4.40 | 0.93 | - |
| 1 | 13 23 11 | -58 05 41 | 307.13 | +4.52 | 0.68 | 2 |
| 1 | 13 23 11 | -57 58 41 | 307.15 | +4.63 | 0.74 | 3 |
| 1 | 13 24 04 | -59 01 41 | 307.13 | +3.58 | 0.97 | - |
| 1 | 13 24 04 | -58 54 41 | 307.14 | +3.69 | 0.68 | - |
| 1 | 13 24 04 | -58 47 41 | 307.16 | +3.81 | 0.68 | 3 |
| 1 | 13 24 04 | -58 40 41 | 307.17 | +3.92 | 0.56 | - |
| 1 | 13 24 04 | -58 33 41 | 307.19 | +4.04 | 0.56 | 1 |
| 1 | 13 24 04 | -58 26 41 | 307.20 | +4.16 | 0.65 | 1 |
| 1 | 13 24 04 | -58 19 41 | 307.22 | +4.27 | 0.65 | 1 |
| 1 | 13 24 04 | -58 12 41 | 307.23 | +4.39 | 0.68 | 1 |
| 1 | 13 24 04 | -58 05 41 | 307.25 | +4.50 | 0.68 | 1 |
| 1 | 13 24 04 | -57 58 41 | 307.26 | +4.62 | 0.68 | 1 |

**Table B.1** continued...

| Region | RA [hms] | Dec [° ′ ″] | $l$ [°] | $b$ [°] | $E(B-V)$ [mag] | $N_{detections}$ |
|---|---|---|---|---|---|---|
| (1) | (2a) | (2b) | (3a) | (3b) | (4) | (5) |
| 2 | 14 30 52 | -56 48 41 | 316.26 | +3.46 | 1.15 | - |
| 2 | 14 30 52 | -56 55 41 | 316.22 | +3.36 | 1.45 | - |
| 2 | 14 30 52 | -57 02 41 | 316.17 | +3.25 | 1.45 | - |
| 2 | 14 30 52 | -57 09 41 | 316.13 | +3.14 | 1.45 | - |
| 2 | 14 30 52 | -57 16 41 | 316.09 | +3.03 | 1.82 | - |
| 2 | 14 30 52 | -57 23 41 | 316.04 | +2.92 | 1.82 | - |
| 2 | 14 30 52 | -57 30 41 | 315.10 | +2.82 | 1.54 | - |
| 2 | 14 30 52 | -57 37 41 | 315.95 | +2.71 | 1.54 | - |
| 2 | 14 30 52 | -57 44 41 | 315.91 | +2.60 | 1.81 | 2 |
| 2 | 14 30 52 | -57 51 41 | 315.87 | +2.49 | 1.92 | 1 |
| 3 | 14 48 19 | -59 33 23 | 317.25 | +0.03 | 12.4 | - |
| 3 | 14 48 19 | -59 40 23 | 317.20 | -0.08 | 12.4 | - |
| 3 | 14 48 19 | -59 47 23 | 317.15 | -0.18 | 8.40 | - |
| 3 | 14 48 19 | -59 54 23 | 317.10 | -0.29 | 7.05 | - |
| 3 | 14 48 19 | -60 01 23 | 317.05 | -0.40 | 5.38 | 1 |
| 3 | 14 48 19 | -60 08 23 | 317.00 | -0.50 | 5.38 | 1 |
| 3 | 14 48 19 | -60 15 23 | 316.95 | -0.61 | 5.38 | 1 |
| 3 | 14 48 19 | -60 22 23 | 316.90 | -0.71 | 5.20 | - |
| 3 | 14 48 19 | -60 29 23 | 316.85 | -0.82 | 5.32 | - |
| 3 | 14 48 19 | -60 36 23 | 316.80 | -0.92 | 3.19 | - |
| 3 | 14 48 19 | -60 43 23 | 316.75 | -1.03 | 3.19 | - |
| 3 | 14 49 15 | -59 33 23 | 317.36 | -0.03 | 12.4 | - |
| 3 | 14 49 15 | -59 40 23 | 317.31 | -0.13 | 8.40 | - |
| 3 | 14 49 15 | -59 47 23 | 317.26 | -0.24 | 8.40 | - |
| 3 | 14 49 15 | -59 54 23 | 317.21 | -0.34 | 8.40 | - |
| 3 | 14 49 15 | -60 01 23 | 317.16 | -0.45 | 6.57 | - |
| 3 | 14 49 15 | -60 08 23 | 317.10 | -0.55 | 5.38 | - |
| 3 | 14 49 15 | -60 15 23 | 317.05 | -0.66 | 5.20 | - |
| 3 | 14 49 15 | -60 22 23 | 317.00 | -0.76 | 5.20 | - |
| 3 | 14 49 15 | -60 29 23 | 316.95 | -0.87 | 5.20 | - |
| 3 | 14 49 15 | -60 36 23 | 316.90 | -0.97 | 3.45 | - |
| 3 | 14 49 15 | -60 43 23 | 316.85 | -1.08 | 3.19 | - |
| 3 | 14 50 11 | -59 33 23 | 317.47 | -0.08 | 13.4 | - |
| 3 | 14 50 11 | -59 40 23 | 317.42 | -0.18 | 18.3 | - |
| 3 | 14 50 11 | -59 47 23 | 317.36 | -0.29 | 8.40 | - |
| 3 | 14 50 11 | -59 54 23 | 317.31 | -0.39 | 6.57 | - |
| 3 | 14 50 11 | -60 01 23 | 317.26 | -0.50 | 6.57 | 1 |

**Table B.1** continued...

| Region | RA [hms] | Dec [° ′ ″] | $l$ [°] | $b$ [°] | $E(B-V)$ [mag] | $N_{detections}$ |
|---|---|---|---|---|---|---|
| (1) | (2a) | (2b) | (3a) | (3b) | (4) | (5) |
| 3 | 14 50 11 | -60 08 23 | 317.21 | -0.60 | 6.57 | - |
| 3 | 14 50 11 | -60 15 23 | 317.16 | -0.71 | 5.84 | - |
| 3 | 14 50 11 | -60 22 23 | 317.11 | -0.81 | 5.20 | - |
| 3 | 14 50 11 | -60 29 23 | 317.06 | -0.92 | 3.45 | - |
| 3 | 14 50 11 | -60 36 23 | 317.00 | -1.02 | 3.45 | - |
| 3 | 14 50 11 | -60 43 23 | 316.95 | -1.13 | 2.50 | - |
| 3 | 14 51 08 | -59 33 23 | 317.57 | -0.13 | 18.3 | - |
| 3 | 14 51 08 | -59 40 23 | 317.52 | -0.24 | 18.3 | - |
| 3 | 14 51 08 | -59 47 23 | 317.47 | -0.34 | 18.3 | - |
| 3 | 14 51 08 | -59 54 23 | 317.42 | -0.44 | 14.9 | - |
| 3 | 14 51 08 | -60 01 23 | 317.37 | -0.55 | 6.57 | - |
| 3 | 14 51 08 | -60 08 23 | 317.31 | -0.65 | 5.84 | - |
| 3 | 14 51 08 | -60 15 23 | 317.26 | -0.76 | 5.84 | - |
| 3 | 14 51 08 | -60 22 23 | 317.21 | -0.86 | 5.84 | - |
| 3 | 14 51 08 | -60 29 23 | 317.16 | -0.97 | 4.25 | - |
| 3 | 14 51 08 | -60 36 23 | 317.11 | -1.07 | 3.45 | - |
| 3 | 14 51 08 | -60 43 23 | 317.06 | -1.18 | 2.50 | - |
| 4 | 15 00 30 | -60 43 23 | 318.07 | -1.70 | 1.95 | - |
| 4 | 15 00 30 | -60 36 23 | 318.13 | -1.60 | 1.95 | - |
| 4 | 15 00 30 | -60 29 23 | 318.18 | -1.50 | 1.95 | - |
| 4 | 15 00 30 | -60 22 23 | 318.24 | -1.40 | 1.95 | - |
| 4 | 15 00 30 | -60 15 23 | 318.30 | -1.29 | 3.76 | - |
| 4 | 15 00 30 | -60 08 23 | 318.35 | -1.19 | 3.76 | - |
| 4 | 15 00 30 | -60 01 23 | 318.41 | -1.09 | 6.25 | - |
| 4 | 15 00 30 | -59 54 23 | 318.46 | -0.98 | 6.25 | - |
| 4 | 15 00 30 | -59 47 23 | 318.52 | -0.88 | 6.25 | - |
| 4 | 15 00 30 | -59 40 23 | 318.57 | -0.78 | 7.37 | - |
| 4 | 15 00 30 | -59 33 23 | 318.63 | -0.68 | 7.03 | - |
| 4 | 15 01 26 | -60 43 23 | 318.17 | -1.76 | 1.72 | 2 |
| 4 | 15 01 26 | -60 36 23 | 318.23 | -1.66 | 1.72 | 1 |
| 4 | 15 01 26 | -60 29 23 | 318.29 | -1.55 | 1.95 | - |
| 4 | 15 01 26 | -60 22 23 | 318.34 | -1.45 | 1.95 | - |
| 4 | 15 01 26 | -60 15 23 | 318.40 | -1.35 | 3.84 | 2 |
| 4 | 15 01 26 | -60 08 23 | 318.45 | -1.25 | 3.84 | - |
| 4 | 15 01 26 | -60 01 23 | 318.51 | -1.14 | 3.84 | - |
| 4 | 15 01 26 | -59 54 23 | 318.56 | -1.04 | 6.25 | - |
| 4 | 15 01 26 | -59 47 23 | 318.62 | -0.94 | 6.25 | - |

**Table B.1** continued...

| Region | RA [hms] | Dec [° ′ ″] | $l$ [°] | $b$ [°] | $E(B-V)$ [mag] | $N_{detections}$ |
|---|---|---|---|---|---|---|
| (1) | (2a) | (2b) | (3a) | (3b) | (4) | (5) |
| 4 | 15 01 26 | -59 40 23 | 318.68 | -0.84 | 7.03 | - |
| 4 | 15 01 26 | -59 33 23 | 318.73 | -0.73 | 7.03 | - |
| 5 | 15 23 00 | -59 33 23 | 321.08 | -2.13 | 1.25 | - |
| 5 | 15 23 00 | -59 40 23 | 321.01 | -2.23 | 1.25 | - |
| 5 | 15 23 00 | -59 47 23 | 320.95 | -2.33 | 1.25 | - |
| 5 | 15 23 00 | -59 54 23 | 320.88 | -2.43 | 1.53 | 2 |
| 5 | 15 23 00 | -60 01 23 | 320.82 | -2.52 | 1.54 | 1 |
| 5 | 15 23 00 | -60 08 23 | 320.76 | -2.62 | 1.54 | - |
| 5 | 15 23 00 | -60 15 23 | 320.69 | -2.72 | 1.84 | - |
| 5 | 15 23 00 | -60 22 23 | 320.63 | -2.82 | 1.84 | - |
| 5 | 15 23 00 | -60 29 23 | 320.57 | -2.92 | 1.02 | 1 |
| 5 | 15 23 00 | -60 36 23 | 320.50 | -3.01 | 1.02 | - |
| 5 | 15 23 00 | -60 43 23 | 320.44 | -3.11 | 1.02 | 1 |
| 6 | 15 38 56 | -59 33 23 | 322.73 | -3.29 | 0.89 | 1 |
| 6 | 15 38 56 | -59 40 23 | 322.66 | -3.38 | 0.94 | - |
| 6 | 15 38 56 | -59 47 23 | 322.60 | -3.47 | 0.98 | - |
| 6 | 15 38 56 | -59 54 23 | 322.53 | -3.57 | 0.98 | - |
| 6 | 15 38 56 | -60 01 23 | 322.46 | -3.66 | 0.83 | - |
| 6 | 15 38 56 | -60 08 23 | 322.39 | -3.76 | 0.83 | - |
| 6 | 15 38 56 | -60 15 23 | 322.32 | -3.85 | 0.76 | 1 |
| 6 | 15 38 56 | -60 22 23 | 322.25 | -3.94 | 0.68 | 5 |
| 6 | 15 38 56 | -60 29 23 | 322.18 | -4.04 | 0.68 | 2 |
| 6 | 15 38 56 | -60 36 23 | 322.11 | -4.13 | 0.66 | - |
| 6 | 15 38 56 | -60 43 23 | 322.04 | -4.22 | 0.66 | - |
| 6 | 15 39 52 | -59 33 23 | 322.83 | -3.36 | 0.89 | 2 |
| 6 | 15 39 52 | -59 40 23 | 322.76 | -3.45 | 0.94 | 3 |
| 6 | 15 39 52 | -59 47 23 | 322.69 | -3.55 | 0.94 | 2 |
| 6 | 15 39 52 | -59 54 23 | 322.62 | -3.64 | 0.83 | 2 |
| 6 | 15 39 52 | -60 01 23 | 322.55 | -3.73 | 0.83 | 1 |
| 6 | 15 39 52 | -60 08 23 | 322.48 | -3.83 | 0.83 | 1 |
| 6 | 15 39 52 | -60 15 23 | 322.41 | -3.92 | 0.73 | 3 |
| 6 | 15 39 52 | -60 22 23 | 322.34 | -4.01 | 0.68 | 1 |
| 6 | 15 39 52 | -60 29 23 | 322.27 | -4.11 | 0.68 | 1 |
| 6 | 15 39 52 | -60 36 23 | 322.20 | -4.20 | 0.61 | 1 |
| 6 | 15 39 52 | -60 43 23 | 322.13 | -4.29 | 0.61 | 1 |
| 6 | 15 40 48 | -59 33 23 | 322.93 | -3.43 | 0.87 | N/A |
| 6 | 15 40 48 | -59 40 23 | 322.85 | -3.52 | 0.94 | N/A |

**Table B.1** continued...

| Region | RA [hms] | Dec [° ′ ″] | $l$ [°] | $b$ [°] | $E(B-V)$ [mag] | $N_{detections}$ |
|---|---|---|---|---|---|---|
| (1) | (2a) | (2b) | (3a) | (3b) | (4) | (5) |
| 6 | 15 40 48 | -59 47 23 | 322.78 | -3.62 | 0.94 | N/A |
| 6 | 15 40 48 | -59 54 23 | 322.71 | -3.71 | 0.76 | 1 |
| 6 | 15 40 48 | -60 01 23 | 322.64 | -3.80 | 0.76 | 2 |
| 6 | 15 40 48 | -60 08 23 | 322.57 | -3.90 | 0.73 | 2 |
| 6 | 15 40 48 | -60 15 23 | 322.50 | -4.00 | 0.73 | 2 |
| 6 | 15 40 48 | -60 22 23 | 322.43 | -4.08 | 0.73 | - |
| 6 | 15 40 48 | -60 29 23 | 322.36 | -4.18 | 0.61 | - |
| 6 | 15 40 48 | -60 36 23 | 322.29 | -4.27 | 0.61 | 6 |
| 6 | 15 40 48 | -60 43 23 | 322.22 | -4.36 | 0.61 | - |
| 7 | 16 02 22 | -60 43 23 | 324.27 | -6.03 | 0.34 | 2 |
| 7 | 16 02 22 | -60 36 23 | 324.35 | -5.94 | 0.34 | 1 |
| 7 | 16 02 22 | -60 29 23 | 324.43 | -5.85 | 0.31 | 1 |
| 7 | 16 02 22 | -60 22 23 | 324.51 | -5.77 | 0.31 | 4 |
| 7 | 16 02 22 | -60 15 23 | 324.58 | -5.68 | 0.31 | 2 |
| 7 | 16 02 22 | -60 08 23 | 324.66 | -5.59 | 0.37 | - |
| 7 | 16 02 22 | -60 01 23 | 324.74 | -5.50 | 0.37 | 2 |
| 7 | 16 02 22 | -59 54 23 | 324.82 | -5.42 | 0.37 | 1 |
| 7 | 16 02 22 | -59 47 23 | 324.89 | -5.33 | 0.39 | 1 |
| 7 | 16 02 22 | -59 40 23 | 324.97 | -5.24 | 0.39 | 1 |
| 7 | 16 02 22 | -59 33 23 | 325.05 | -5.15 | 0.39 | 1 |
| 7 | 16 03 18 | -60 43 23 | 324.36 | -6.10 | 0.34 | 5 |
| 7 | 16 03 18 | -60 36 23 | 324.44 | -6.02 | 0.35 | 1 |
| 7 | 16 03 18 | -60 29 23 | 324.51 | -5.93 | 0.35 | - |
| 7 | 16 03 18 | -60 22 23 | 324.59 | -5.84 | 0.31 | 3 |
| 7 | 16 03 18 | -60 15 23 | 324.67 | -5.76 | 0.34 | 2 |
| 7 | 16 03 18 | -60 08 23 | 324.75 | -5.67 | 0.34 | 2 |
| 7 | 16 03 18 | -60 01 23 | 324.83 | -5.58 | 0.37 | 3 |
| 7 | 16 03 18 | -59 54 23 | 324.90 | -5.49 | 0.36 | 3 |
| 7 | 16 03 18 | -59 47 23 | 324.98 | -5.41 | 0.36 | 1 |
| 7 | 16 03 18 | -59 40 23 | 325.06 | -5.32 | 0.39 | 3 |
| 7 | 16 03 18 | -59 33 23 | 325.14 | -5.23 | 0.33 | - |

# Appendix C

# Postage Stamps of Galaxies and Candidates

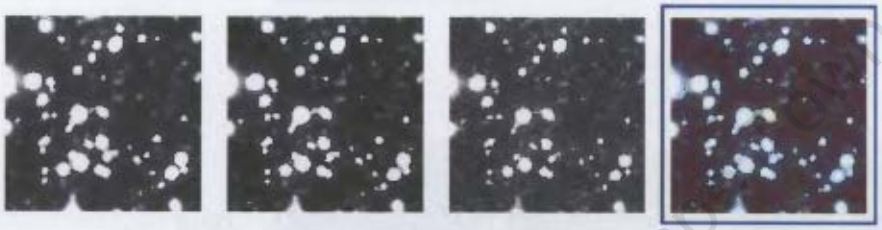

$ID: 1$
$l = 315.95°$
$b = 2.58°$
$A_K = 0.66^m$
$S.D. = 3.23E-04 stars/deg^2$

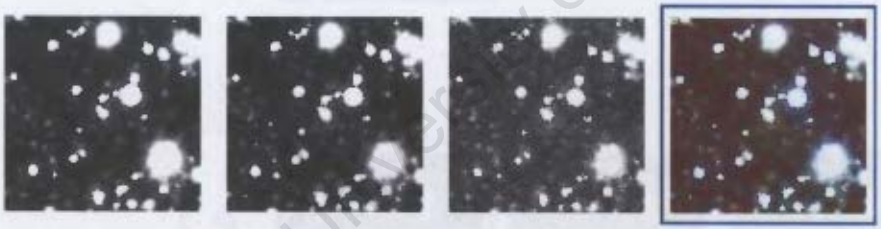

$ID: 2$
$l = 315.85°$
$b = 2.57°$
$A_K = 0.70^m$
$S.D. = 3.23E-04 stars/deg^2$

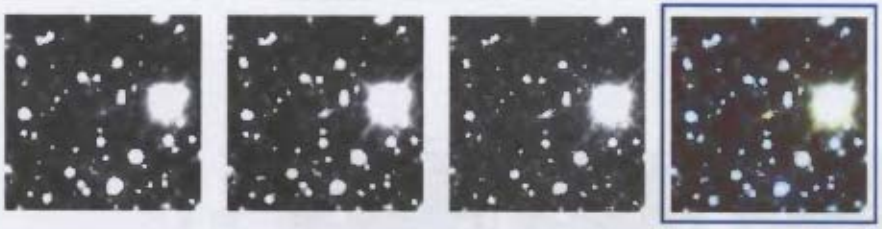

$ID: 3$
$l = 315.90°$
$b = 2.47°$
$A_K = 0.66^m$
$S.D. = 3.18E+04 stars/deg^2$

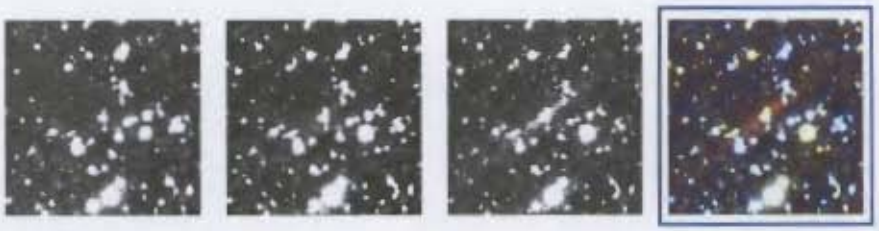

*ID* : 4
$l = 317.04°$
$b = -0.49°$
$A_K = 1.97^m$
$S.D. = 7.64E+04 stars/deg^2$

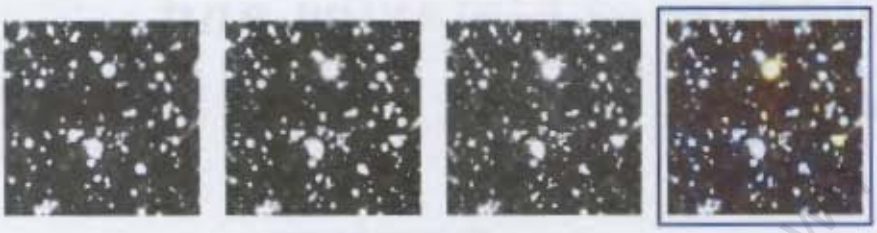

*ID* : 5
$l = 316.90°$
$b = -0.39°$
$A_K = 1.97^m$
$S.D. = 1.08E+05 stars/deg^2$

*ID* : 6
$l = 316.87°$
$b = 0.60°$
$A_K = 2.65^m$
$S.D. = 7.41E-04 stars/deg^2$

*ID* : 7
$l = 317.26°$
$b = 0.50°$
$A_K = 2.41^m$
$S.D. = 5.44E+04 stars/deg^2$

*ID* : 8
$l = 318.42°$
$b = -1.36°$
$A_K = 1.41^m$
$S.D. = 6.67E-04 stars/deg^2$

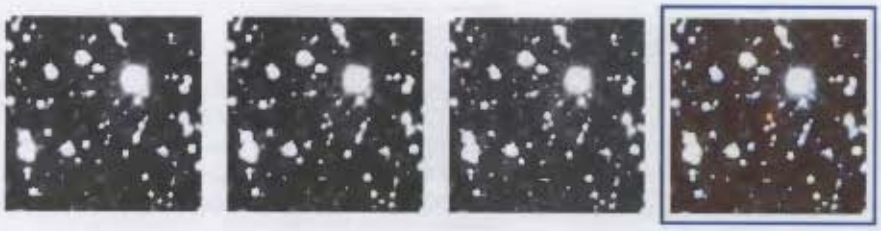

$ID: 9$
$l = 318.47°$
$b = -1.33°$
$A_K = 1.41^m$
$S.D. = 6.67E+04 stars/deg^2$

$ID: 10$
$l = 318.26°$
$b = -1.70°$
$A_K = 0.63^m$
$S.D. = 5.20E+04 stars/deg^2$

$ID: 11$
$l = 318.16°$
$b = -1.74°$
$A_K = 0.63^m$
$S.D. = 4.59E+04 stars/deg^2$

$ID: 12$
$l = 318.16°$
$b = -1.73°$
$A_K = 0.63^m$
$S.D. = 4.59E+04 stars/deg^2$

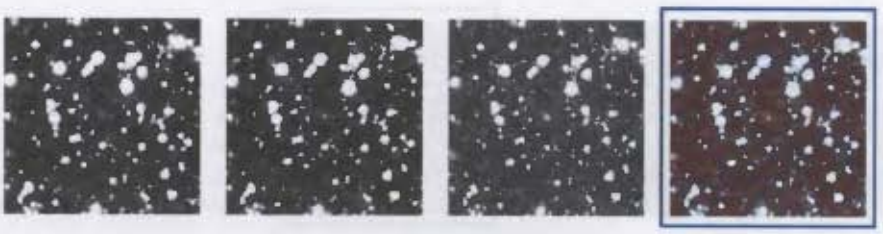

$ID: 13$
$l = 320.89°$
$b = -2.50°$
$A_K = 0.56^m$
$S.D. = 4.27E+04 stars/deg^2$

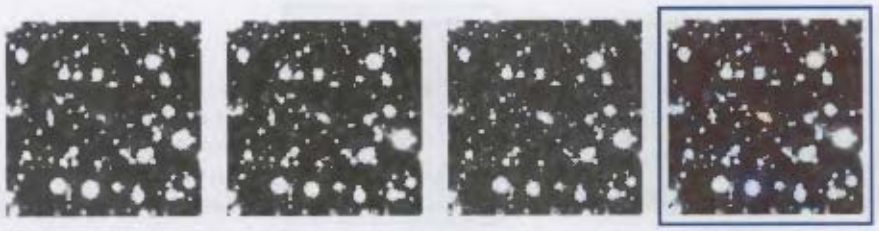

$ID: 14$
$l = 320.85^{\circ}$
$b = -2.41^{\circ}$
$A_K = 0.57^{m}$
$S.D. = 3.61E-04 stars/deg^2$

$ID: 15$
$l = 320.81^{\circ}$
$b = -2.41^{\circ}$
$A_K = 0.57^{m}$
$S.D. = 3.61E+04 stars/deg^2$

$ID: 16$
$l = 320.56^{\circ}$
$b = -2.90^{\circ}$
$A_K = 0.38^{m}$
$S.D. = 3.14E+04 stars/deg^2$

$ID: 17$
$l = 320.45^{\circ}$
$b = -3.13^{\circ}$
$A_K = 0.27^{m}$
$S.D. = 3.30E+04 stars/deg^2$

$ID: 18$
$l = 322.73^{\circ}$
$b = -3.35^{\circ}$
$A_K = 0.33^{m}$
$S.D. = 2.80E+04 stars/deg^2$

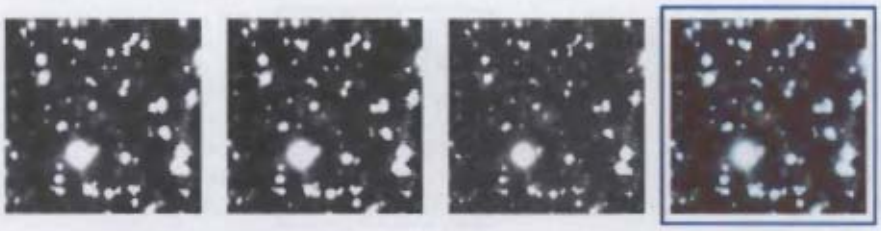

$ID: 19$
$l = 322.29^{\circ}$
$b = -3.84^{\circ}$
$A_K = 0.28^{m}$
$S.D. = 2.54E-04 stars/deg^2$

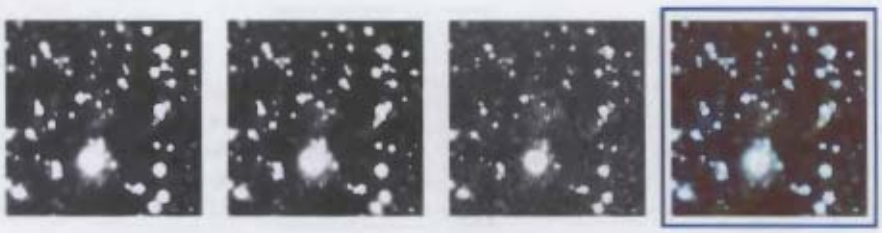

$ID: 20$
$l = 322.23^{\circ}$
$b = -4.00^{\circ}$
$A_K = 0.25^{m}$
$S.D. = 2.68E+04 stars/deg^2$

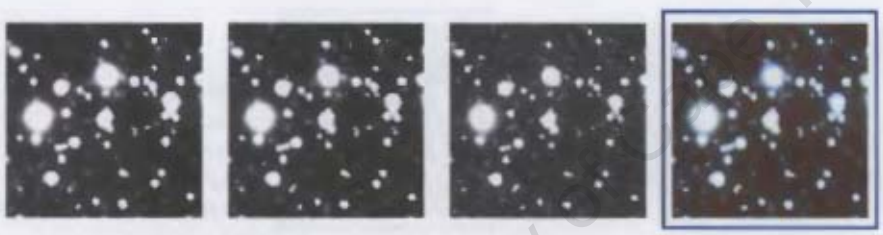

$ID: 21$
$l = 322.24^{\circ}$
$b = -3.99^{\circ}$
$A_K = 0.25^{m}$
$S.D. = 2.68E+04 stars/deg^2$

$ID: 22$
$l = 322.23^{\circ}$
$b = -4.00^{\circ}$
$A_K = 0.25^{m}$
$S.D. = 2.68E+04 stars/deg^2$

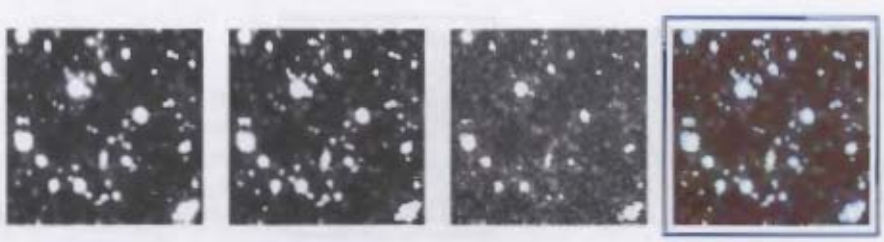

$ID: 23$
$l = 322.20^{\circ}$
$b = -3.99^{\circ}$
$A_K = 0.25^{m}$
$S.D. = 2.68E-04 stars/deg^2$

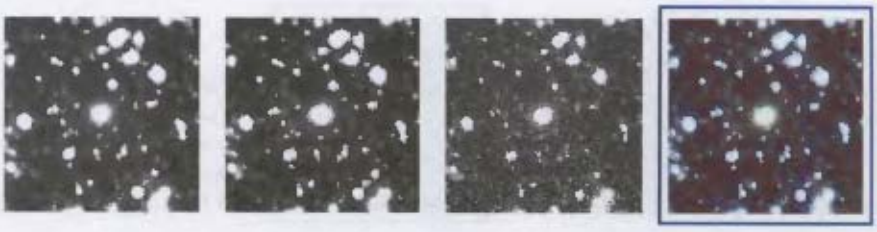

$ID: 24$
$l - 322.20°$
$b - \quad 3.98°$
$A_K - 0.25^m$
$S.D. - 2.68\mathrm{E} - 04\mathrm{stars/deg}^2$

$ID: 25$
$l = 322.16°$
$b = \quad 4.06°$
$A_K - 0.25^m$
$S.D. - 2.40\mathrm{E} + 04\mathrm{stars/deg}^2$

$ID: 26$
$l = 322.18°$
$b = -3.98°$
$A_K - 0.25^m$
$S.D. - 2.40\mathrm{E} + 04\mathrm{stars/deg}^2$

$ID: 27$
$l = 322.45°$
$b = -3.81°$
$A_K = 0.30^m$
$S.D. = 2.79\mathrm{E} + 04\mathrm{stars/deg}^2$

$ID: 28$
$l = 322.54°$
$b = -3.77°$
$A_K - 0.30^m$
$S.D. - 2.95\mathrm{E} + 04\mathrm{stars/deg}^2$

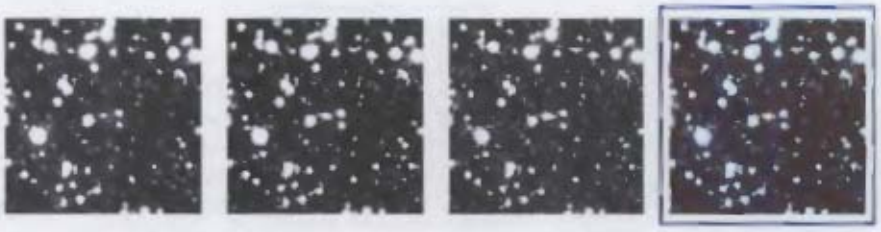

$ID: 29$
$l = 322.60°$
$b = -3.64°$
$A_K = 0.30^m$
$S.D. = 2.93E+04 stars/deg^2$

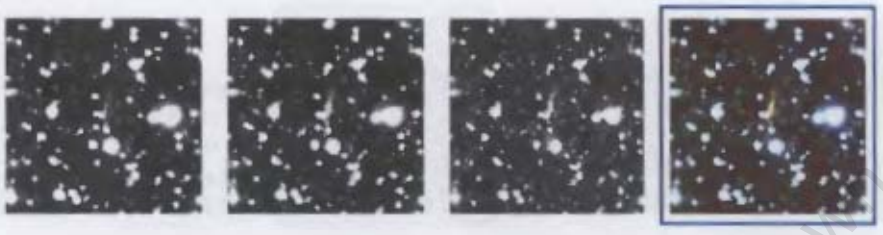

$ID: 30$
$l = 322.60°$
$b = -3.61°$
$A_K = 0.36^m$
$S.D. = 2.93E+04 stars/deg^2$

$ID: 31$
$l = 322.73°$
$b = -3.52°$
$A_K = 0.35^m$
$S.D. = 2.93E+04 stars/deg^2$

$ID: 32$
$l = 322.69°$
$b = -3.52°$
$A_K = 0.35^m$
$S.D. = 2.93E+04 stars/deg^2$

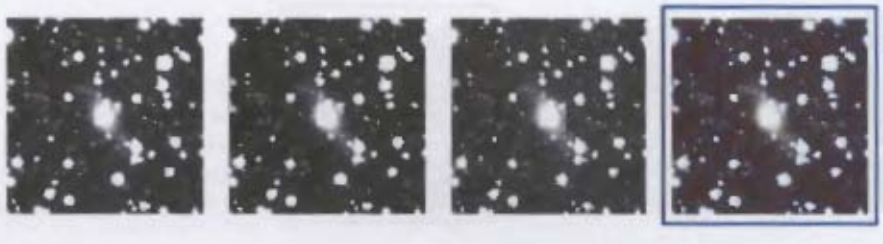

$ID: 33$
$l = 322.81°$
$b = -3.46°$
$A_K = 0.35^m$
$S.D. = 2.70E+04 stars/deg^2$

$ID: 34$
$l = 322.76°$
$b = -3.47°$
$A_K = 0.33^m$
$S.D. = 2.70E-04 stars/deg^2$

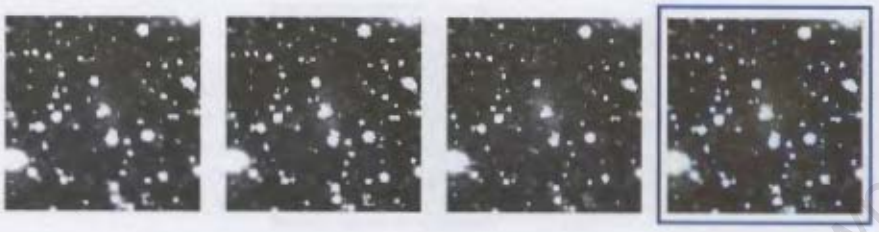

$ID: 35$
$l = 322.75°$
$b = -3.44°$
$A_K = 0.35^m$
$S.D. = 2.70E+04 stars/deg^2$

$ID: 36$
$l = 322.85°$
$b = -3.35°$
$A_K = 0.33^m$
$S.D. = 2.80E+04 stars/deg^2$

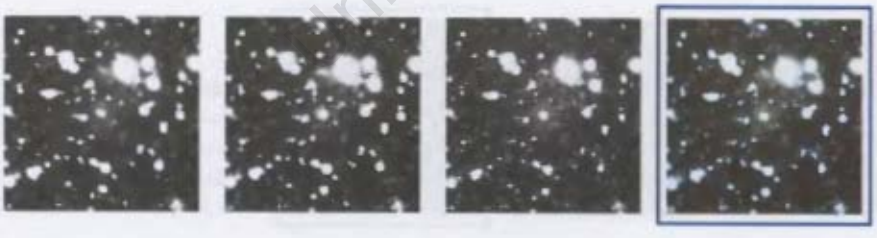

$ID: 37$
$l = 322.83°$
$b = -3.29°$
$A_K = 0.33^m$
$S.D. = 2.80E-04 stars/deg^2$

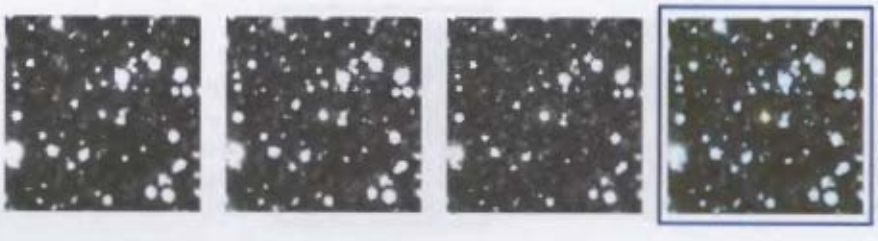

$ID: 38$
$l = 322.38°$
$b = -3.92°$
$A_K = 0.27^m$
$S.D. = 2.81E-04 stars/deg^2$

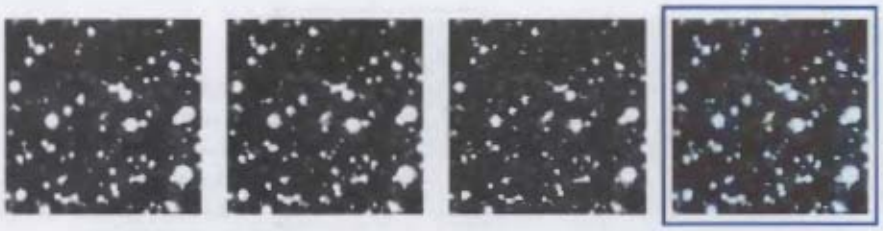

$ID$ : 39
$l = 322.40°$
$b = -3.88°$
$A_K = 0.27^m$
$S.D. = 2.81E + 04 stars/deg^2$

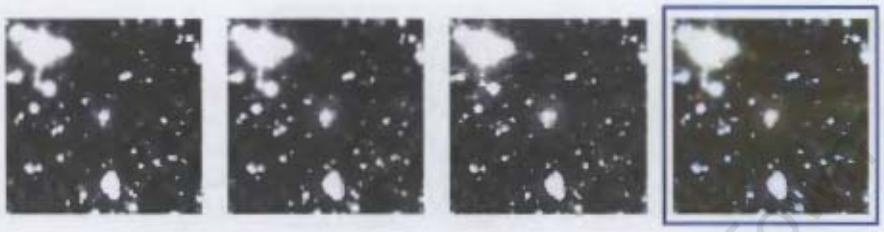

$ID$ : 40
$l = 322.37°$
$b = -3.87°$
$A_K = 0.28^m$
$S.D. = 2.81E + 04 stars/deg^2$

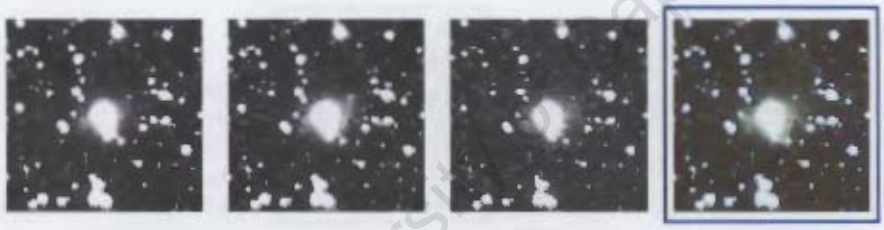

$ID$ : 41
$l = 322.31°$
$b = -3.96°$
$A_K = 0.25^m$
$S.D. = 2.86E + 04 stars/deg^2$

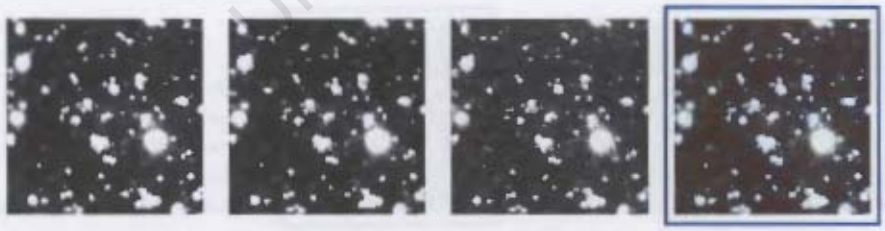

$ID$ : 42
$l = 322.32°$
$b = -4.08°$
$A_K = 0.25^m$
$S.D. = 2.68E + 04 stars/deg^2$

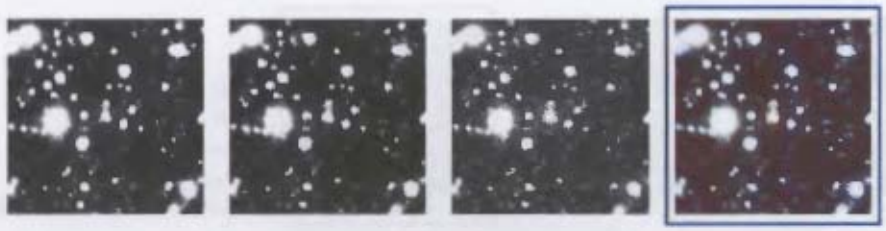

$ID$ : 43
$l = 322.16°$
$b = -4.20°$
$A_K = 0.23^m$
$S.D. = 2.32E + 04 stars/deg^2$

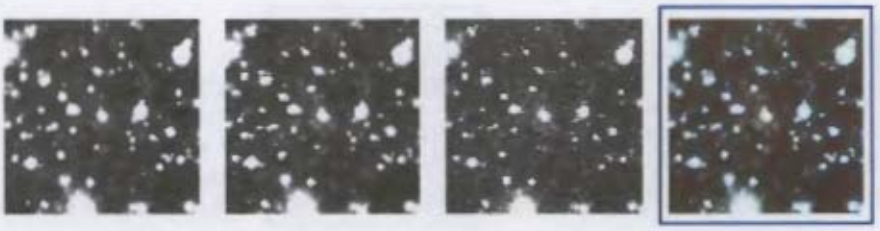

$ID: 44$
$l = 322.19°$
$b = -4.28°$
$A_K = 0.23^m$
$S.D. = 2.26E+04 stars/deg^2$

$ID: 45$
$l = 322.60°$
$b = -3.85°$
$A_K = 0.30^m$
$S.D. = 2.71E-04 stars/deg^2$

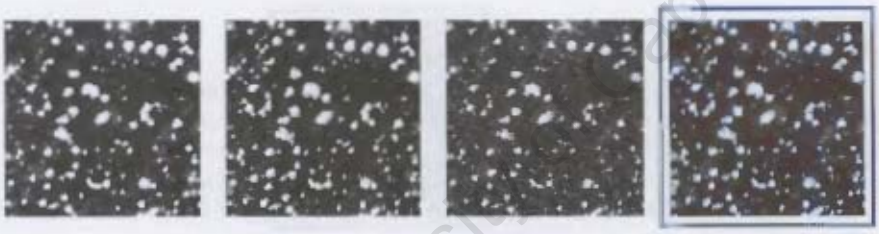

$ID: 46$
$l = 322.56°$
$b = -3.87°$
$A_K = 0.30^m$
$S.D. = 3.71E+04 stars/deg^2$

$ID: 47$
$l = 322.71°$
$b = -3.80°$
$A_K = 0.28^m$
$S.D. = 2.74E-04 stars/deg^2$

$ID: 48$
$l = 322.67°$
$b = -3.80°$
$A_K = 0.28^m$
$S.D. = 2.74E+04 stars/deg^2$

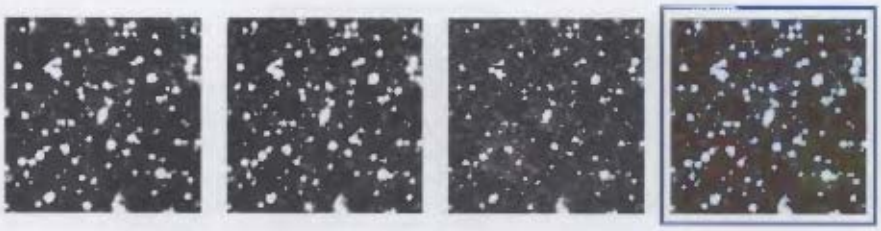

$ID: 49$
$l = 322.77°$
$b = -3.67°$
$A_K = 0.28^m$
$S.D. = 2.60E+04 stars/deg^2$

$ID: 50$
$l = 322.53°$
$b = -4.06°$
$A_K = 0.27^m$
$S.D. = 2.52E+04 stars/deg^2$

$ID: 51$
$l = 322.49°$
$b = -3.99°$
$A_K = 0.27^m$
$S.D. = 2.52E+04 stars/deg^2$

$ID: 52$
$l = 322.31°$
$b = -4.33°$
$A_K = 0.23^m$
$S.D. = 2.62E+04 stars/deg^2$

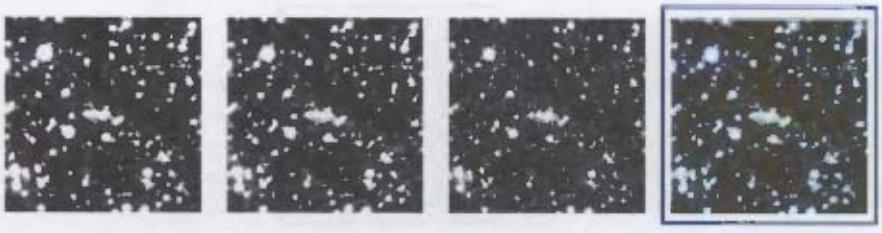

$ID: 53$
$l = 322.36°$
$b = -4.26°$
$A_K = 0.23^m$
$S.D. = 2.62E-04 stars/deg^2$

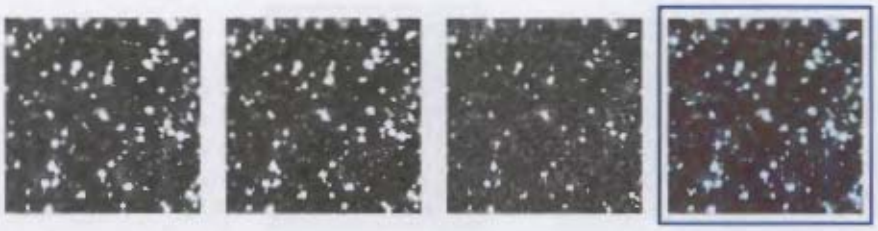

$ID: 54$
$l = 322.32°$
$b = -1.31°$
$A_K = 0.23^m$
$S.D. = 2.62E-04 stars/deg^2$

$ID: 55$
$l = 322.35°$
$b = -1.25°$
$A_K = 0.23^m$
$S.D. = 2.62E+04 stars/deg^2$

$ID: 56$
$l = 322.31°$
$b = -1.29°$
$A_K = 0.23^m$
$S.D. = 2.62E+04 stars/deg^2$

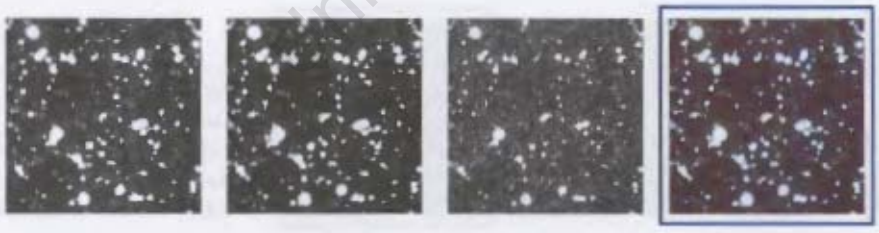

$ID: 57$
$l = 322.25°$
$b = -1.28°$
$A_K = 0.23^m$
$S.D. = 2.62E+04 stars/deg^2$

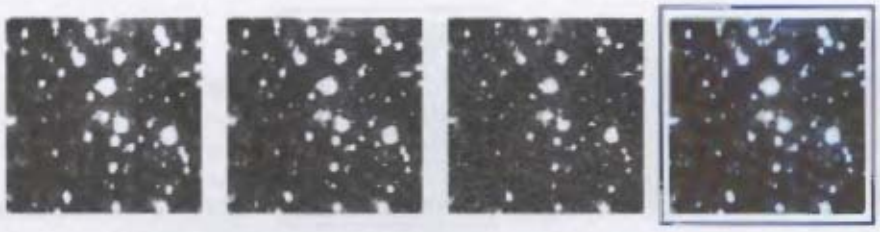

$ID: 58$
$l = 324.77°$
$b = -5.55°$
$A_K = 0.13^m$
$S.D. = 1.45E-04 stars/deg^2$

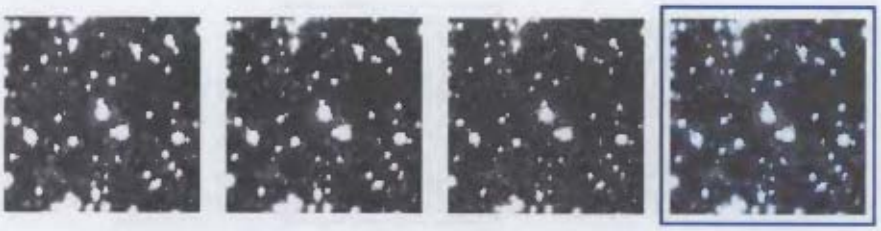

$ID: 59$
$l = 324.74^{\circ}$
$b = \quad 5.45^{\circ}$
$A_K = 0.13^{\mathrm{m}}$
$S.D. = 1.45\mathrm{E}+04\mathrm{stars/deg}^2$

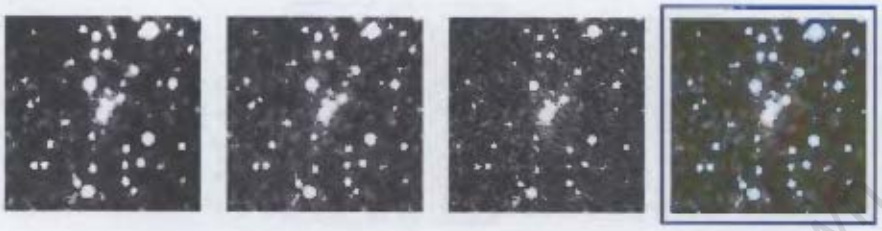

$ID: 60$
$l = 324.86^{\circ}$
$b = \quad 5.43^{\circ}$
$A_K \quad 0.13^{\mathrm{m}}$
$S.D. = 1.64\mathrm{E}+04\mathrm{stars/deg}^2$

$ID: 61$
$l = 324.91^{\circ}$
$b = -5.36^{\circ}$
$A_K = 0.14^{\mathrm{m}}$
$S.D. = 1.73\mathrm{E}+04\mathrm{stars/deg}^2$

$ID: 62$
$l = 325.00^{\circ}$
$b = \quad 5.25^{\circ}$
$A_K = 0.14^{\mathrm{m}}$
$S.D. = 1.65\mathrm{E}+04\mathrm{stars/deg}^2$

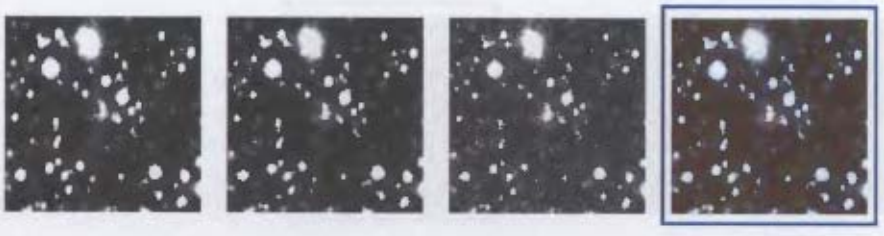

$ID: 63$
$l = 325.06^{\circ}$
$b \quad -5.11^{\circ}$
$A_K = 0.15^{\mathrm{m}}$
$S.D. = 1.82\mathrm{E}+04\mathrm{stars/deg}^2$

$ID: 64$
$l = 324.60°$
$b = -5.74°$
$A_K = 0.11^m$
$S.D. = 1.66E+04 stars/deg^2$

$ID: 65$
$l = 324.61°$
$b = -5.70°$
$A_K = 0.11^m$
$S.D. = 1.66E+04 stars/deg^2$

$ID: 66$
$l = 324.54°$
$b = -5.74°$
$A_K = 0.11^m$
$S.D. = 1.91E-04 stars/deg^2$

$ID: 67$
$l = 324.53°$
$b = -5.73°$
$A_K = 0.11^m$
$S.D. = 1.91E+04 stars/deg^2$

$ID: 68$
$l = 324.50°$
$b = -5.74°$
$A_K = 0.11^m$
$S.D. = 1.91E+04 stars/deg^2$

$ID: 69$
$l = 324.49°$
$b = -5.70°$
$A_K \sim 0.11^m$
$S.D. \sim 1.91E+04 stars/deg^2$

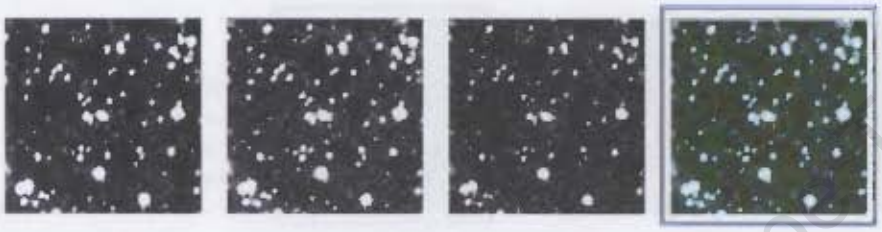

$ID: 70$
$l \sim 324.36°$
$b \sim -5.84°$
$A_K = 0.12^m$
$S.D. = 1.93E+04 stars/deg^2$

$ID: 71$
$l = 324.10°$
$b = -5.92°$
$A_K \sim 0.13^m$
$S.D. = 1.75E+04 stars/deg^2$

$ID: 72$
$l = 324.32°$
$b \sim 6.00°$
$A_K = 0.13^m$
$S.D. = 1.95E+04 stars/deg^2$

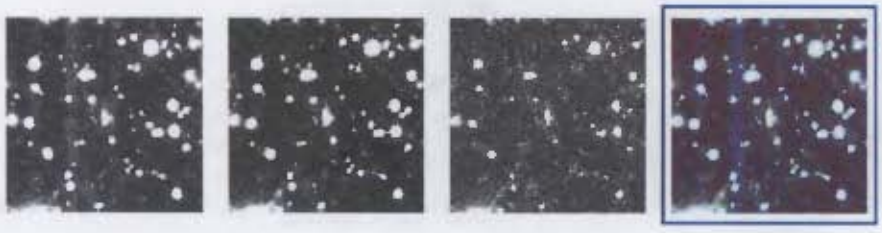

$ID: 73$
$l \sim 324.31°$
$b = -5.98°$
$A_K = 0.13^m$
$S.D. = 1.95E+04 stars/deg^2$

$ID: 74$
$l = 324.77°$
$b = \ \ 5.70°$
$A_K \ - 0.12^m$
$S.D. \ - 1.63E+04 stars/deg^2$

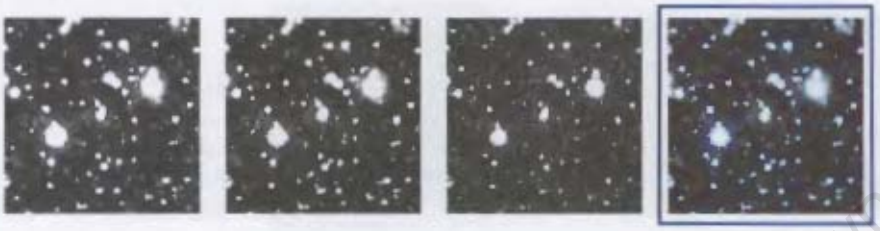

$ID: 75$
$l = 324.77°$
$b = \ \ 5.67°$
$A_K - 0.12^m$
$S.D. = 1.63E+04 stars/deg^2$

$ID: 76$
$l = 324.89°$
$b = \ \ 5.55°$
$A_K - 0.13^m$
$S.D. = 1.43E-04 stars/deg^2$

$ID: 77$
$l = 324.81°$
$b = \ \ 5.60°$
$A_K - 0.13^m$
$S.D. = 1.43E+04 stars/deg^2$

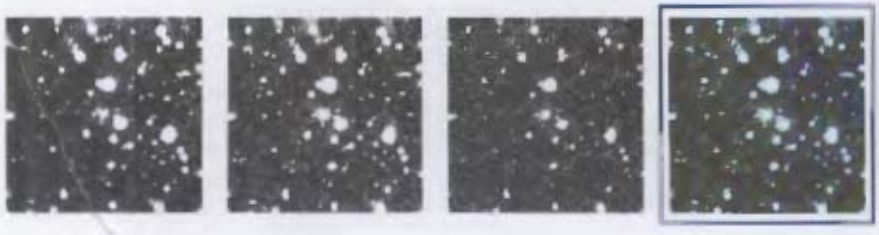

$ID: 78$
$l = 324.77°$
$b = -5.55°$
$A_K \ - 0.13^m$
$S.D. = 1.43E+04 stars/deg^2$

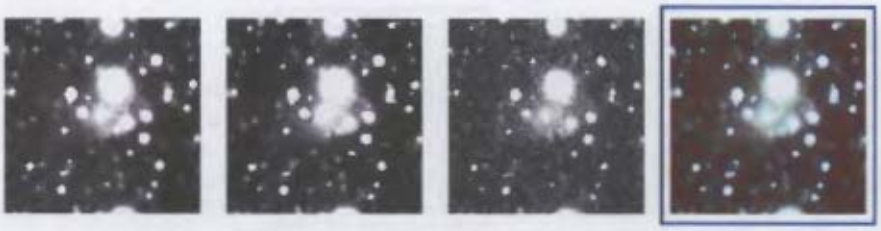

$ID: 79$
$l = 324.92°$
$b = -5.48°$
$A_K = 0.13^m$
$S.D. = 1.88E-04 stars/deg^2$

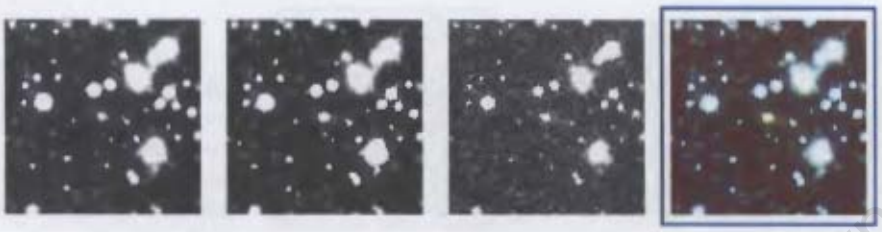

$ID: 80$
$l = 324.88°$
$b = -5.52°$
$A_K = 0.13^m$
$S.D. = 1.88E-04 stars/deg^2$

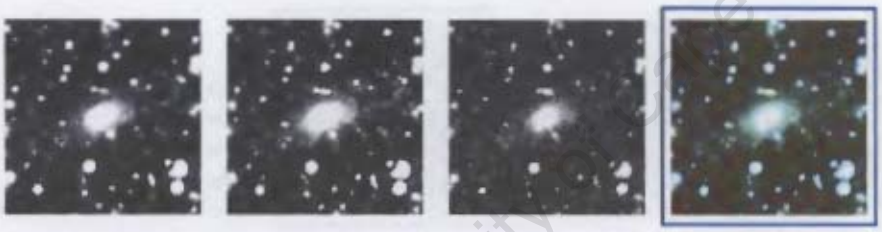

$ID: 81$
$l = 324.92°$
$b = -5.45°$
$A_K = 0.13^m$
$S.D. = 1.88E+04 stars/deg^2$

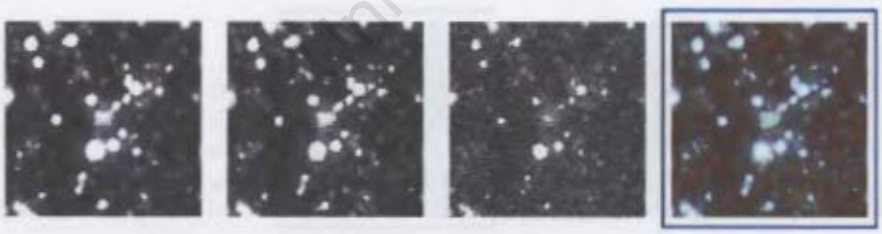

$ID: 82$
$l = 324.93°$
$b = -5.42°$
$A_K = 0.13^m$
$S.D. = 1.69E-04 stars/deg^2$

$ID: 83$
$l = 325.11°$
$b = -5.31°$
$A_K = 0.14^m$
$S.D. = 1.55E+04 stars/deg^2$

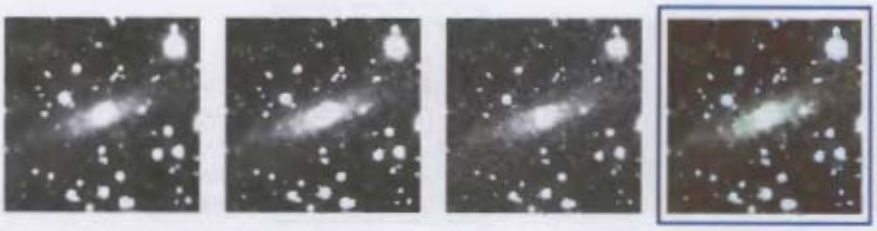

*ID* : 84
$l = 325.08°$
$b = -5.33°$
$A_K = 0.14^m$
*S.D.* 1.55E + 04stars/deg$^2$

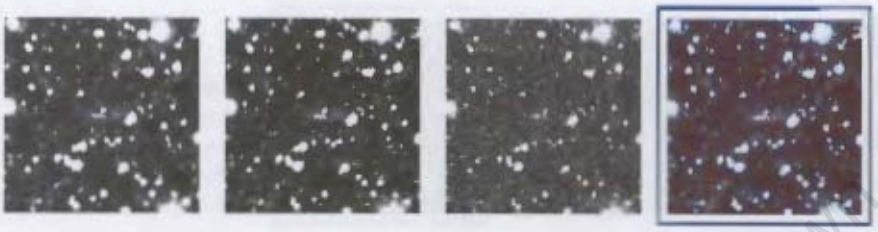

*ID* : 85
$l = 325.08°$
$b = -5.27°$
$A_K = 0.14^m$
*S.D.* = 1.55E + 04stars/deg$^2$

*ID* : 86
$l = 324.64°$
$b = -5.73°$
$A_K = 0.12^m$
*S.D.* = 1.68E + 04stars/deg$^2$

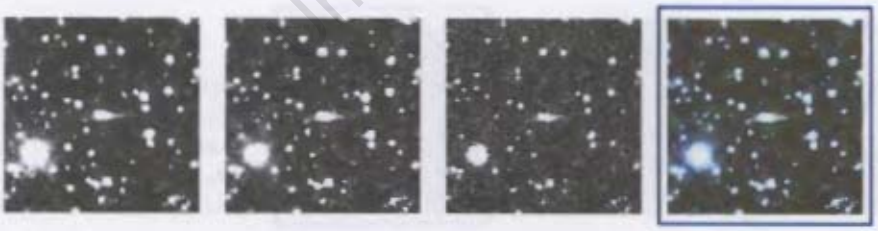

*ID* : 87
$l = 324.66°$
$b = -5.70°$
$A_K = 0.12^m$
*S.D.* = 1.68E + 04stars/deg$^2$

*ID* : 88
$l = 324.64°$
$b = -5.52°$
$A_K = 0.12^m$
*S.D.* = 1.69E + 04stars/deg$^2$

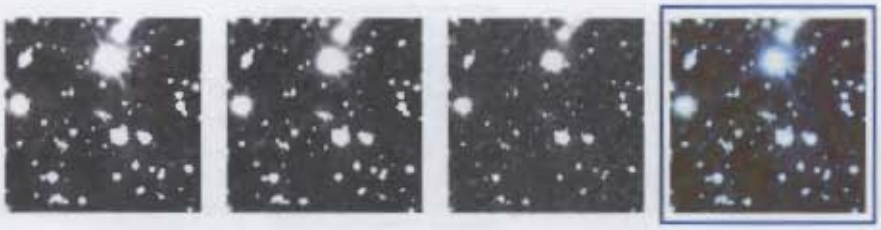

$ID: 89$
$l = 324.61^{\circ}$
$b = -5.84^{\circ}$
$A_K = 0.11^{m}$
$S.D. = 1.09E-04 stars/deg^2$

$ID: 90$
$l = 324.60^{\circ}$
$b = -5.83^{\circ}$
$A_K = 0.11^{m}$
$S.D. = 1.09E+04 stars/deg^2$

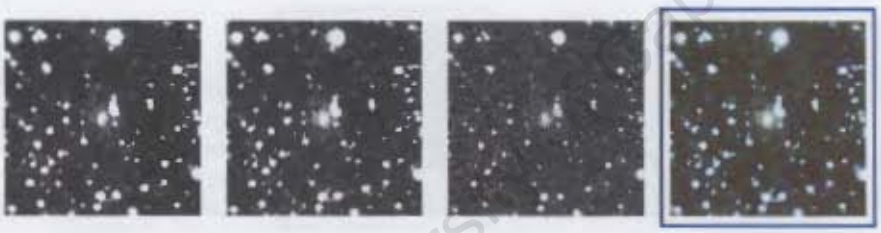

$ID: 91$
$l = 324.45^{\circ}$
$b = -5.93^{\circ}$
$A_K = 0.13^{m}$
$S.D. = 1.79E+04 stars/deg^2$

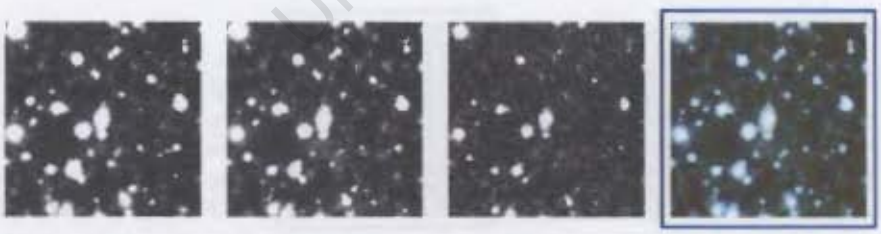

$ID: 92$
$l = 324.39^{\circ}$
$b = -6.11^{\circ}$
$A_K = 0.13^{m}$
$S.D. = 1.71E+04 stars/deg^2$

$ID: 93$
$l = 324.38^{\circ}$
$b = -6.10^{\circ}$
$A_K = 0.13^{m}$
$S.D. = 1.71E+04 stars/deg^2$

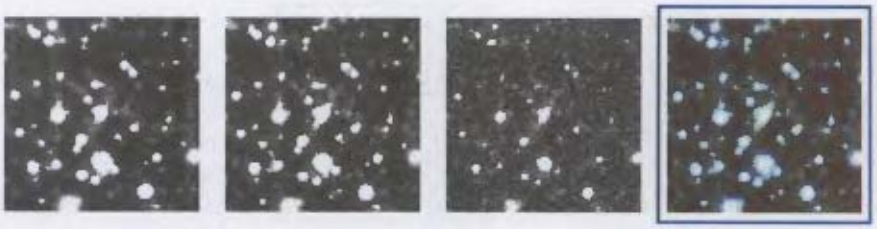

$ID: 94$
$l = 324.36°$
$b = -6.11°$
$A_K = 0.13^{m}$
$S.D. = 1.71E + 04 stars/deg^2$

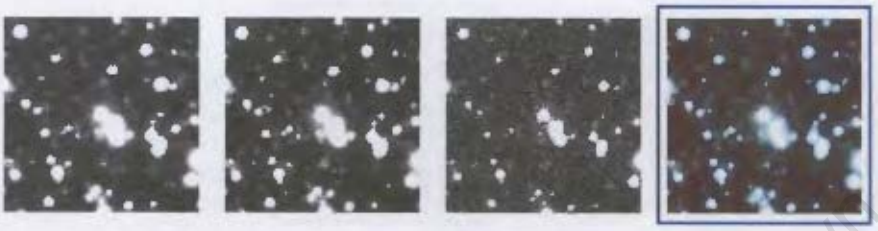

$ID: 95$
$l = 324.33°$
$b = -6.11°$
$A_K = 0.13^{m}$
$S.D. = 1.71E + 04 stars/deg^2$

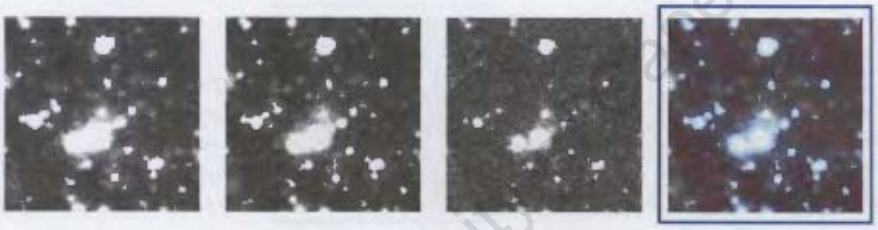

$ID: 96$
$l = 324.36°$
$b = -6.06°$
$A_K = 0.13^{m}$
$S.D. = 1.71E + 04 stars/deg^2$

$ID: 97$
$l = 307.21°$
$b = 4.68°$
$A_K = 0.27^{m}$
$S.D. = 1.94E + 04 stars/deg^2$

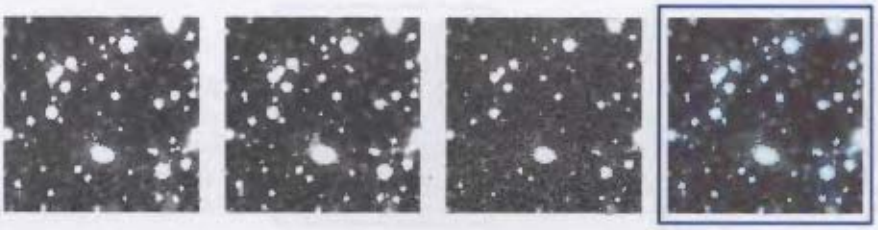

$ID: 98$
$l = 307.10°$
$b = 4.58°$
$A_K = 0.34^{m}$
$S.D. = 1.94E + 04 stars/deg^2$

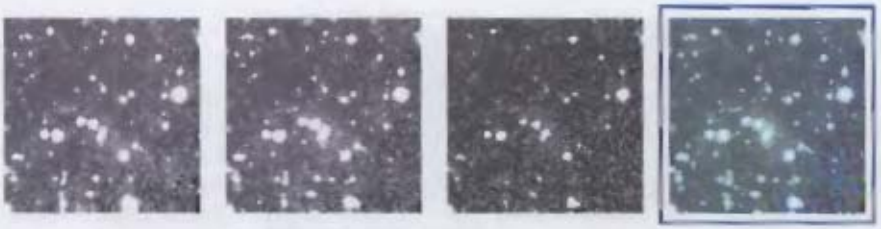

$ID$ : 99
$l = 307.07°$
$b = 4.58°$
$A_K = 0.34^m$
$S.D. = 1.04E + 04 stars/deg^2$

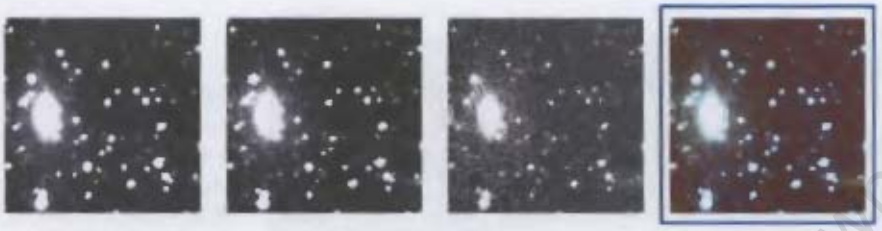

$ID$ : 100
$l = 307.19°$
$b = 4.48°$
$A_K = 0.25^m$
$S.D. = 1.98E - 04 stars/deg^2$

$ID$ : 101
$l = 307.08°$
$b = 4.58°$
$A_K = 0.34^m$
$S.D = 1.98E + 04 stars/deg^2$

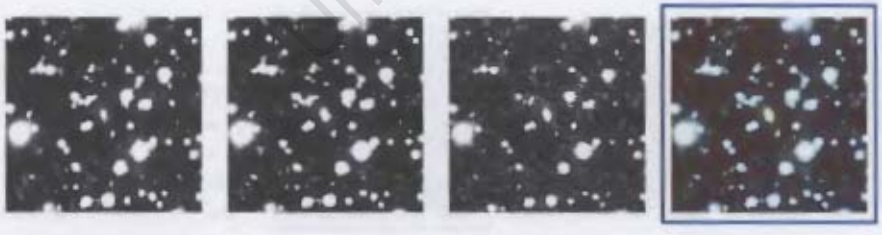

$ID$ : 102
$l = 307.04°$
$b = 4.24°$
$A_K = 0.32^m$
$S.D. = 1.92E + 04 stars/deg^2$

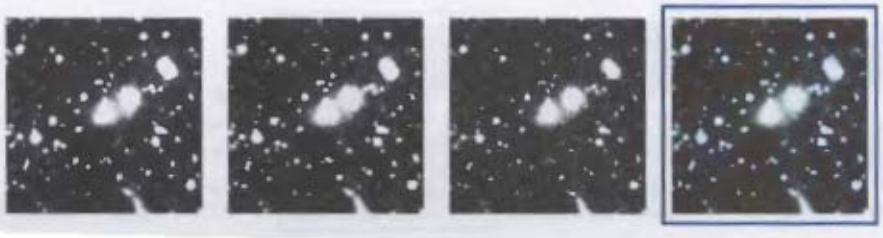

$ID$ : 103
$l = 307.09°$
$b = 4.19°$
$A_K = 0.32^m$
$S.D. = 1.78E + 04 stars/deg^2$

$ID$ : 104
$l = 307.08°$
$b = 4.18°$
$A_K = 0.32^m$
$S.D. = 1.78E + 04 stars/deg^2$

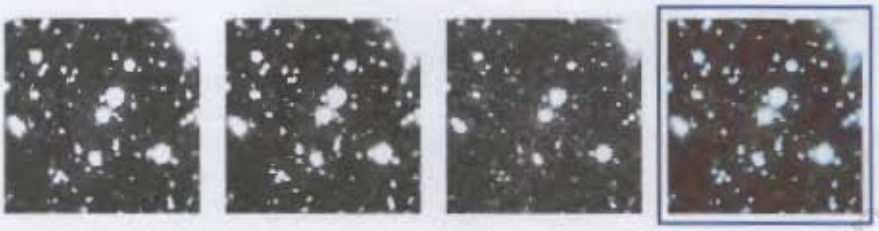

$ID$ : 105
$l = 307.07°$
$b = 4.13°$
$A_K = 0.32^m$
$S.D. = 1.78E + 04 stars/deg^2$

$ID$ : 106
$l = 307.02°$
$b = 3.94°$
$A_K = 0.22^m$
$S.D. = 1.74E + 04 stars/deg^2$

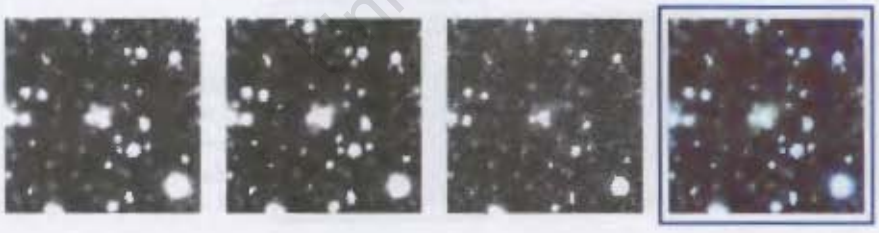

$ID$ : 107
$l = 307.21°$
$b = 4.09°$
$A_K = 0.27^m$
$S.D. = 1.90E + 04 stars/deg^2$

$ID$ : 108
$l = 307.19°$
$b = 4.48°$
$A_K = 0.25^m$
$S.D. = 1.94E + 04 stars/deg^2$

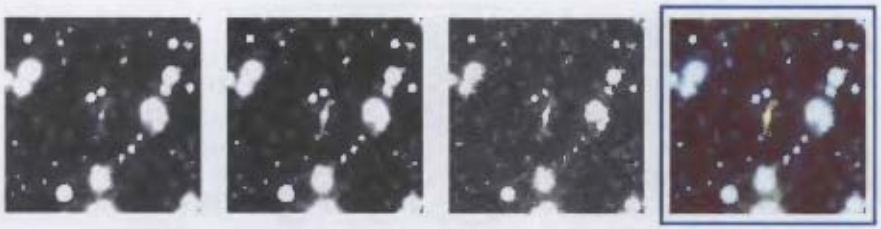

$ID: 109$
$l - 307.23°$
$b - 4.39°$
$A_K = 0.25^m$
$S.D. = 1.91E - 04 stars/deg^2$

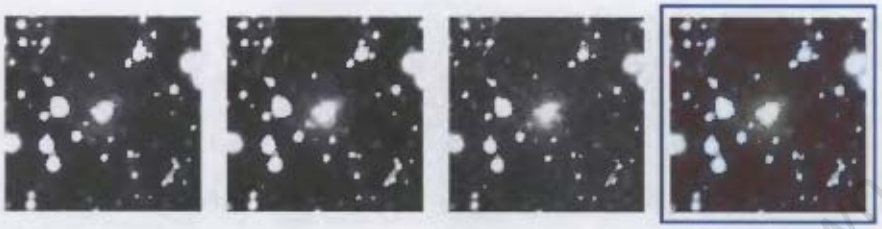

$ID: 110$
$l \quad 307.20°$
$b = 4.30°$
$A_K = 0.24^m$
$S.D. = 1.81E - 04 stars/deg^2$

$ID: 111$
$l = 307.17°$
$b = 4.20°$
$A_K - 0.24^m$
$S.D. - 1.92E - 04 stars/deg^2$

$ID: 112$
$l - 307.22°$
$b = 4.10°$
$A_K = 0.21^m$
$S.D. = 1.78E + 04 stars/deg^2$

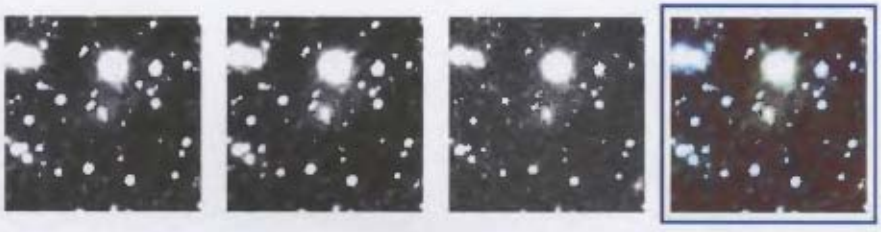

$ID: 113$
$l = 307.21°$
$b = 3.86°$
$A_K = 0.25^m$
$S.D. - 1.61E + 04 stars/deg^2$

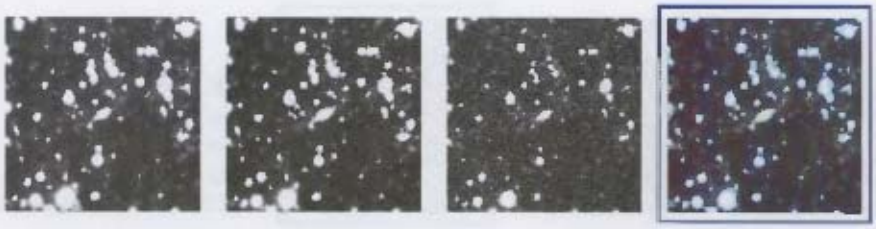

$ID$ : 114
$l = 307.15°$
$b = 3.77°$
$A_K = 0.25^m$
$S.D. = 1.61\mathrm{E}+04 \mathrm{stars/deg}^2$

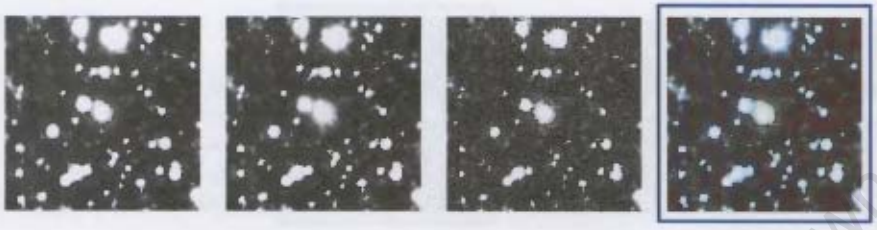

$ID$ : 115
$l = 307.15°$
$b = 3.85°$
$A_K = 0.25^m$
$S.D. = 1.61\mathrm{E}+04 \mathrm{stars/deg}^2$

# Appendix D

# Photometry Script

```
## James Tagg 2008
##
## This script acts as a wrapper for the Source Extractor (SE) software. It allows for configuration of SE input parameters such as aperture sizes,
## magnitude zeropoint, and detector gain, etc. After configuration, SE performs J, H, and Ks band photometry on each galaxy in all the postage stamp
## FITS files in the working directory. Input lists of magnitude zeropoints and galaxies that aren't centered in their stamp must be given. Output is
## written to a file specified by the user. Any objects which give problems (i.e. are not detected in one or two bands) are described in an output
## problem file.

from os import system
import os, time
from math import *
import numpy as n
import sextractor

# Path must be working directory where FITS images are stored
path = '/home/james/work/fields/working/final2/'
os.chdir(path)
flist = n.array(os.listdir(os.getcwd()))
flist.sort()

# Files for I/O
offcenter = file('/home/james/active/offcenter.dat','r')
magzp_file = file('/home/james/work/magzp/all.magzp.list','r')
position = magzp_file.tell()
#outfile = file('../../galpos_new.dat','w')
#problemfile = file('../../problems_new.dat','w')
outfile = file('../../galpos_83gain.dat','w')
problemfile = file('../../problems_83gain.dat','w')

problemfile.write('Field\tError flag (0 for no objects, 1 for no nearby objects)\n\n')

## Source Extractor Parameters
##------------------------------------------------------------------

# Create a SExtractor instance
sex = sextractor.SExtractor()

# Modify the SExtractor configuration
sex.config['DETECT_THRESH'] = 2.5
sex.config['ANALYSIS_THRESH'] = 2.5
# Give single or multiple apertures in pixels
sex.config['PHOT_APERTURES'] = 13.33 #22.2222
sex.config['PHOT_AUTOPARAMS'] = [2.5, 3.5]
#sex.config['PHOT_PETROPARAMS'] = [1.2, 3.5]
sex.config['MAG_ZEROPOINT'] = 20.398
sex.config['GAIN'] = 83.3333
sex.config['PIXEL_SCALE'] = 0.45
```

```
sex.config['VERBOSE_TYPE'] = "NORMAL"
sex.config['BACK_SIZE'] = 128
sex.config['CHECKIMAGE_TYPE'] = "APERTURES"

# Add a parameter to the parameter list
sex.config['CATALOG_NAME'] = "test.cat"

##--------------------------------------------------------------

# Initialise variables

exposure = 24.0 # Exposure time in seconds

offlist = [None]*0
offgals = [33,61,108,109,110,111]
xlist = [None]*0
ylist = [None]*0
count = 0

##--------------------------------------------------------------

# Make a list of galaxy co-ordinates for SExtractor to use

while True:
line = offcenter.readline()
if line == "":
break

linesplit = line.split()
offlist.append(linesplit)

offarray = n.array(offlist)
offgals = n.array(offgals)

for i in range(len(flist)/3):
if n.any(offgals == (i+1)):
# Galaxy is offcenter

x = int(offarray[count][1])
y = int(offarray[count][2])

count += 1
else:
# Galaxy is in center of image
x = 67
y = 67

xlist.append(x)
ylist.append(y)

##--------------------------------------------------------------

# Initialise photometry array : Each galaxy
phot = n.zeros((28,len(flist)/3))

# Do SExtractor Photometry


# Set catalog name
catalog_name = sex.config['CATALOG_NAME']

for k in range(len(flist)/3):

himage = flist[k]
jimage = flist[k + (len(flist)/3)]
kimage = flist[k + 2*(len(flist)/3)]

for band in range(3):
if band == 0:
current_file = himage
```

```
elif band == 1:
current_file = jimage
else:
current_file = kimage

# Define check image path and name
sex.config['CHECKIMAGE_NAME'] = '../checks/' + current_file[0:len(current_file)-12] + '.aper.fits'
# Define magzp lookup for magzp list
current_magzp_file = current_file[0:len(current_file)-17]+'.fits'
#print current_magzp_file

magzp_file.seek(position)

# Set magzp to a default 100 - this will get modified when correct magzp is found
print 'SETTING MAGZP TO : 100.0'
sex.config['MAG_ZEROPOINT'] = 100.0

# If magzp lookup is found, set correct magzp for field
while True:
line = magzp_file.readline()
if line == "":
break

linesplit = line.split()

if str(linesplit[0]) == current_magzp_file:
magzp = float(linesplit[2])
print 'SETTING MAGZP TO : ' + str(magzp)
sex.config['MAG_ZEROPOINT'] = magzp
break

# Lauch SExtractor on a FITS file
sex.run(current_file)

# Read the resulting catalog file
catalog_f = sextractor.open(catalog_name)
catalog = catalog_f.readlines()

# If there is a problem with catalog, record it
if (len(catalog) == 0):
print 'WARNING : No objects found in '+current_file+'!'
problemfile.write(current_file+'\t0\n')
time.sleep(3.0)

found = -1

# best_dist is a free parameter which is used to find the galaxy. I.e., any object within a radius of best_dist pixels around the stamp
# center must be the target galaxy. Don't change this parameter unless sources are being confused.
best_dist = 21.0

for j in range(len(catalog)):
xreal = catalog[j]['X_IMAGE']
yreal = catalog[j]['Y_IMAGE']
dist = sqrt((xreal-xlist[k])**2.0 + (yreal-ylist[k])**2.0)
print 'Distance : ' + str(dist)

if (dist < best_dist):
best_dist = dist
found = j

# If galaxy not found close to predicted position, record it as a problem
if (j == len(catalog) - 1) & (best_dist == 21.0):
print 'WARNING : No nearby objects!'
problemfile.write(current_file+'\t1\n')
#time.sleep(1.0)
#found = -1

# If galaxy is not found, put '-1' into the photometry array
if (found == -1):
phot[:,k] = -1
```

```
phot[0,k] = k+1

# Else put it's photometry details in the phot array
else:
A = catalog[found]['KRON_RADIUS'] * catalog[found]['A_IMAGE'] #Semi-major axis
B = catalog[found]['KRON_RADIUS'] * catalog[found]['B_IMAGE'] #Semi-minor axis
area = pi * A * B #Area of ellipse defined by Kron Aperture
mag = catalog[found]['MAG_AUTO'] + 2.5*log10(exposure) #Magnitude from Kron Aperture

phot[0,k] = k+1

phot[(band*9)+1,k] = catalog[found]['NUMBER']
phot[(band*9)+2,k] = catalog[found]['MAG_APER'] + 2.5*log10(exposure)
phot[(band*9)+3,k] = catalog[found]['MAGERR_APER']
phot[(band*9)+4,k] = mag
phot[(band*9)+5,k] = catalog[found]['MAGERR_AUTO']
phot[(band*9)+6,k] = catalog[found]['CLASS_STAR']
phot[(band*9)+7,k] = A * 0.45 #Kron Radius in Arcsec
phot[(band*9)+8,k] = catalog[found]['MU_MAX'] + 2.5*log10(exposure) #Central Pixel Surface Brightness
phot[(band*9)+9,k] = mag + 2.5*log10(area) #Surface Brightness

catalog_f.close()

sex.clean(config=True, catalog=True, check=False)
#system('rm aper.fits')
#system('rm back.fits')
#system('rm seg.fits')

problemfile.close()

# Write photometry array to file
for m in range(len(flist)/3):
for n in range(28):
if (n < 27):
outfile.write(str(phot[n,m])+'\t')
else:
outfile.write(str(phot[n,m])+'\n')
```

# Bibliography


Abell, G.O., Corwin, H.G., Olowin, R.P. 1989, ApJS, 70, 1

Arce, H.G. & Goodman, A.A. 1999, ApJ, 512, L135

Bertin, E., Arnouts, S. 1996, A&AS 117, 393

Binggeli, B., Sandage, A. & Tammann, G.A. 1988, ARA&A 26, 509

Buta, R.J. & McCall, M.L. 1999, ApJS, 124, 33

Cameron, L.M. 1990, A&A, 233, 16

Cardelli, J.A., Clayton, G.C., Mathis, J.S. 1989, ApJ, 345, 245

Choloniewski, J. & Valentijn, E.A. 2003, Acta Astron., 53, 265

Cutri, R.M., Skrutskie, M.F., van Dyk, S., et al. 2003 : *The IRSA 2MASS All-Sky Point Source Catalog, NASA/IPAC Infrared Science Archive*, http://irsa.ipac.caltech.edu/applications/Gator/

Da Costa, G.S. 1992, in "Astronomical CCD observing and reduction techniques", ed. Howell, S.B., ASP Vol. 23 (San Francisco)

de Vaucouleurs, G., de Vaucouleurs, A., Corwin, J.R., *Second reference catalogue of bright galaxies*, (Austin: University of Texas Press, 1976)

Dekel, A. 1994, ARA&A 233, 16

Dutra, C.M., Ahumada, A.V., Clariá, J.J., Bica, E., & Barbuy, B. 2003, A&A, 408, 287

Ebeling, H., Mullis, C.R., Tully, R.B. 2002, ApJ, 580, 774

Einasto, M., Saar, E., Einasto, J., Tago, E., Liivamägi, L.J., Martínez, V.J., Starck, J.-L., Müller, V., Heinämäki, P., Nurmi, P., Gramann, M., Hütsi, G. 2007 (arXiv:0706.1126)

Epchtein, N. 1997, in 2nd Euroconference, The Impact of Large Scale Near-Infrared Surveys, eds. Garzón et al., (Dordrecht: Kluwer), 15

Erdoğdu, P., Huchra, J.P., Lahav, O., Colless, M., Cutri, R.M., Falco, E., George, T., Jarrett, T., Jones, D.H., Kochankek, C.S., Macri, L., Mader, J., Martimbeau, N., Pahre, M., Parker, Q., Rassat, A., Saunders, W. 2006, MNRAS, 368, 1515

Fairall, A.P., Woudt, P.A., Kraan-Korteweg, R.C. 1998, A&AS, 127, 463

Garilli, B., Maccagni, D. & Andreon, S. 1999, A&A 342, 408

Henning, P.A., Staveley-Smith, L., Ekers, R.D., et al. 2000, AJ, 119, 2686

Henning, P.A., Kraan-Korteweg, R.C., Staveley-Smith, L., 2005, in "Nearby Large-Scale Structures and the Zone of Avoidance", eds. Fairall, A.P. & Woudt, P.A., ASP Conf. Ser. 329 (Cape Town: ASP)

Hoffman, Y. 2000, in "Mapping the Hidden Universe: The Universe Behind the Milky Way - The Universe in HI", eds. Kraan-Korteweg, R.C., Henning, P.A., & Andernach, H., ASP Conf. Ser. 218 (San Francisco: ASP)

Hubble, E. 1929, Proceedings of the National Academy of Sciences of the United States of America, Volume 15, Issue 3, 168

Hudson, M.J. & Lynden-Bell, D. 1991, MNRAS, 252, 219

Jarrett, T.H., Cutri, R., et al. 2000, AJ 119, 2498

Jarrett, T.H., Chester, T., Cutri, R., Schneider, S.E., Huchra, J.P. 2003, AJ, 125, 525

Jarrett, T.H., Koribalski, B.S., Kraan-Korteweg, R.C., Woudt, P.A., Whitney, B.A., Meade, M.R., Babler, B., Churchwell, E., Benjamin, R.A., Indebetouw, R. 2007, AJ, 133, No. 3

Jôeveer, M. & Einasto, J. 1978, in "The Large-Scale Structure of the Universe", eds. Longair, M & Einasto, J., IAU Symposium 79, 241

Joint *IRAS* Working Science Group 1988, IRAS Point Source Catalogue, Version 2, Washington: US Govt. Printing Office

Kandori, R., Kusakabe, N., Tamura, M., et al. 2006

Kocevski, D.D. & Ebeling, H. 2006, ApJ, 645, 1043

Kolatt, T., Dekel, A., & Lahav, O. 1995, MNRAS, 275, 797

Kraan-Korteweg, R.C., Cayette, V., Balkowski, C., Fairall, A.P., Henning, P.A. 1994, in "Unveiling Large-Scale Structures Behind the Milky Way", eds. Balkowski, C. & Kraan-Korteweg, R.C., ASP Conf. Ser. 67 (Observatoire de Paris-Meudon)

Kraan-Korteweg, R.C., Woudt, P.A., Cayatte, V., Fairall, A.P., Balkowski, C., Henning, P.A. 1996, Nature 379, 51

Kraan-Korteweg, R.C. 2000, in "Mapping the Hidden Universe: The Universe Behind the Milky Way - The Universe in HI", eds. Kraan-Korteweg, R.C., Henning, P.A., & Andernach, H., ASP Conf. Ser. 218 (San Francisco: ASP)

Kraan-Korteweg, R.C. 2000, LNP 556, 301

Kraan-Korteweg, R.C., & Lahav, O. 2000, A&ARv 10, 211

Kraan-Korteweg, R.C. 2005, RvMA, 18, 48

Kraan-Korteweg, R.C. & Jarrett, T.H. 2005, in "Nearby Large-Scale Structures and the Zone of Avoidance", eds. Fairall, A.P. & Woudt, P.A., ASP Conf. Ser. 329 (Cape Town: ASP)

Kron, R.G. 1980, ApJS, 43, 305

Lucey, J., Radburn-Smith, D., Hudson, M. 2004, in "Nearby Large-Scale Structures and the Zone of Avoidance", eds. Fairall, A.P. & Woudt, P.A., ASP Conf. Ser. 329 (Cape Town: ASP)

Lynden-Bell, D., Faber, S.M., Burstein, D., Davies, R.L., Dressler, A., Terlevich, R.J., Wegner, G. 1988, ApJ, 326, 19

Lynden-Bell, D., Lahav, O., Burstein, D. 1989, MNRAS, 241, 325

Mamon, G.A. 2000, in Cosmic Flows 1999: Towards an Understanding of Large-Scale Structure, eds. Courteau, S., Strauss, M.A. & Willick, J.A., ASP Conf. Ser. 201, 103 (San Francisco: ASP)

Nagayama, T. 2004, Ph.D. thesis, Univ. of Nagoya

Nagayama, T. et al. 2004, MNRAS, 354, 980

Nagayama, T. et al. 2006, MNRAS, 368, 534

Nakajima, Y., Kandori, R., Tamura, M., et al. 2008, in press.

Nakashima, Y., et al., private communication

Proctor, R.: *The Universe of Stars*, (Longmans, Green and Co., London 1878) pp.41

Radburn-Smith, D.J., Lucey, J.R., Woudt, P.A., Kraan-Korteweg, R.C., Watson, F.G. 2006, MNRAS, 369, 1131

Saunders, W., D'Mellow, K., Tully, B., et al. 2000, in "Mapping the Hidden Universe: The Universe Behind the Milky Way - The Universe in HI", eds. Kraan-Korteweg, R.C., Henning, P.A., & Andernach, H., ASP Conf. Ser. 218 (San Francisco: ASP)

Sanchis, T., Mamon, G.A., Salvador-Solé, E., Solanes, J.M. 2004, A&A, 418, 393

Schlegel, D.J., Finkbeiner, D.P., & Davis, M. 1998, ApJ, 500, 525

Schröder, A.C., Kraan-Korteweg, R.C., Mamon, G.A. 2000, in "Mapping the Hidden Universe: The Universe Behind the Milky Way - The Universe in HI", eds. Kraan-Korteweg, R.C., Henning, P.A., & Andernach, H., ASP Conf. Ser. 218 (San Francisco: ASP)

Schröder, A.C., Mamon, G.A., Kraan-Korteweg, R.C., & Woudt, P.A. 2005, in "Nearby Large-Scale Structures & the Zone of Avoidance", eds. Fairall, A.P. & Woudt, P.A., ASP Conf. Ser. 218, 119 (San Francisco: ASP)

Schröder, A.C., Mamon, G.A., Kraan-Korteweg, R.C., Woudt, P.A. 2007. A&A 466, 481

Shane, C.D. & Wirtanen, C.A. 1967, Publ. Lick Obs. XXII, Pt. 1

Shapley, H. 1961, in Galaxies, Cambridge: Harvard University Press, 159

Skelton, R.E. 2007, M.Sc thesis, Univ. of Cape Town

Skrutskie, M.F., Cutri, R.M., Stiening, R., Weinberg, M.D., Schneider, S., Carpenter, J.M., Beichman, C., Capps, R., Chester, T., Elias, J., and 21 coauthors 2006, AJ 131 (Issue 2), 1163

Staveley-Smith, L., Juraszek, S., Henning, P.A., et al. 2000, in "Mapping the Hidden Universe: The Universe Behind the Milky Way - The Universe in HI", eds. Kraan-Korteweg, R.C., Henning, P.A., & Andernach, H., ASP Conf. Ser. 218 (San Francisco: ASP)

Tashiro, M., Kaneda, H., Makishima, K., Iyomoto, N., et al. 1998, ApJ, 499, 713

Tonry, J. & Schneider, D.P. 1988, AJ, 96, 807

Tonry, J.L., Blakeslee, J.P., Ajhar, E.A., Dressler, A. 2000, ApJ, 530, 625

van Driel, W., Schneider, S.E., Kraan-Korteweg, R.C., Monnier Ragaigne, D. 2008, submitted to A&A

Woudt, P.A., Fairall, A.P., Kraan-Korteweg, R.C. 1997, in "Dark and Visible Matter in Galaxies and Cosmological Implications", eds. Persic, M. & Salucci, P., ASP Conf. Ser. 117 (Sesto Pusteria: ASP)

Woudt, P.A. 1998, Ph.D. thesis, Univ. of Cape Town

Woudt, P.A., Kraan-Korteweg, R.C. 2000, in "Mapping the Hidden Universe: The Universe Behind the Milky Way - The Universe in HI", eds. Kraan-Korteweg, R.C., Henning, P.A., & Andernach, H., ASP Conf. Ser. 218 (San Francisco: ASP)

Woudt, P.A., Kraan-Korteweg, R.C., & Fairall, A.P. 2000, in "Mapping the Hidden Universe: The Universe Behind the Milky Way - The Universe in HI", eds. Kraan-Korteweg, R.C., Henning, P.A., & Andernach, H., ASP Conf. Ser. 218 (San Francisco: ASP)

Woudt, P.A. & Kraan-Korteweg, R.C. 2001, A&A, 380, 441-459

Woudt, P.A., Kraan-Korteweg, R.C., Lucey, J., Fairall, A.P., Moore, S.A.W. 2008, MNRAS, 383, 445